Characterization of VUV Pulses from the Short-Pulse Facility at DELTA and Steps towards Pump-Probe Experiments

Dissertation

zur Erlangung des Doktorgrades
der Fakultät Physik
der Technischen Universität Dortmund

Maryam Huck

Fakultät Physik
Dortmund, Jan. 2015

Gutachter der Dissertation:
Prof. Dr. Shaukat Khan
Prof. Dr. Christian Gutt

To my parents

Abstract

The short-pulse facility at the 1.5-GeV synchrotron light source DELTA, operated by the TU Dortmund University, generates coherent VUV radiation by Coherent Harmonic Generation (CHG) as well as coherent THz pulses. The goal is to provide femtosecond coherent VUV-radiation pulses for time-resolved pump-probe experiments. CHG is based on the interaction of ultrashort laser pulses with electrons in an undulator to generate synchrotron radiation pulses of similar length, but at coherent harmonics of the laser wavelength. The goals of this PhD thesis were the characterization of the CHG pulses and the preparation of the first pump-probe experiments with the new light source. The CHG pulses were characterized using different methods which are applied either at a diagnostics beamline in air (for long wavelengths of 200 nm and above) or at an evacuated VUV beamline (for 200 nm and below). The characterization includes studying the transverse and longitudinal coherence properties of the CHG pulses, the intensity of the radiation, its angular and spectral distribution, estimate of the energy modulation, and the dependence of these properties on different parameters. In order to perform pump-probe experiments, an evacuated laser beamline of 53 m length was constructed and commissioned to guide some part of the laser pulses to the experimental station at the VUV beamline. This included optimizing and focusing the laser beam, realizing the temporal and transverse overlap between pump and probe pulses, controlling and monitoring the beam position with motorized in-vacuum mirrors and diagnostics screens, and stabilizing the angle and position of the beam using an optical feedback system.

Kurzdarstellung

Die Kurzpulsquelle an der 1.5-GeV-Synchrotronstrahlungsquelle DELTA, betrieben von der Technischen Universität Dortmund, erzeugt kohärente VUV-Strahlung durch Coherent Harmonic Generation (CHG) sowie kohärente THz-Pulse. Das Ziel ist, ultrakurze (100 fs) kohärente VUV-Strahlungspulse für zeitaufgelöste Anrege-Abfrage-Experimente zu liefern. CHG basiert auf der Wechselwirkung von Elektronenpaketen mit Femtosekunden-Laserpulsen in einem Undulator, um kohärente Synchrotronstrahlungspulse ähnlicher Dauer auf höheren Harmonischen der Laserwellenlänge zu erzeugen. Das Ziel dieser Doktorarbeit besteht einerseits in der Charakterisierung der CHG-Pulse und andererseits in der Vorbereitung eines ersten Anrege-Abfrage-Experiments mit der neuen Strahlungsquelle. Die Charakterisierung der CHG-Pulse erfordert verschiedene Messmethoden, die bei langen Wellenlängen (200 nm und größer) in einer Diagnose-Strahllinie an Luft, und bei kürzeren Wellenlängen (200 nm und darunter) an einer evakuierten VUV-Strahllinie zur Anwendung kommen. Charakterisiert wurden die transversale und longitudinale Kohärenteigenschaften der CHG-Pulse, die Intensität der Strahlung, ihre räumliche Verteilung, ihr Spektrum sowie die Abhängigkeit dieser Eigenschaften von verschiedenen Parametern. Für die Durchführung von Anrege-Abfrage-Experimenten wurde eine evakuierte Strahllinie von 53 m Länge aufgebaut und in Betrieb genommen, mit der ein Teil der Laserpulse zur Experimentierstation an der VUV-Strahllinie transportiert wird. Die Inbetriebnahme beinhaltet die Optimierung und Fokussierung des Strahls, Realisierung der zeitlichen und räumlichen Überlappung zwischen Anrege- und Abfrage-Puls, die Kontrolle und Beobachtung der Strahlposition mit motorisierten Spiegeln und Diagnoseschirmen, sowie die Stabilisierung von Position und Winkel des Strahls mit Hilfe eines optischen Regelsystems.

Contents

1 Introduction

1.1 Pump-probe experiments

Figure 1.1 shows the world's oldest example of capturing motion into a still picture, five sequential images of a Persian ibex jumping towards the food on a tree, painted on an earthen goblet discovered at the site of the 5200-year-old Burnt City in southeastern Iran [1].

In order to capture images in a similar way, to follow the state of a material in ultrafast dynamic processes such as electron transfer, lattice vibrations, phase transitions, or spin dynamics in real time, a technique called pump-probe can be used. Here, a light pulse with femtosecond (fs) duration excites a sample to a higher state, and after a certain time another pulse probes the state of the sample. Variation of the delay yields the state as function of time.

The temporal resolution of this technique depends on the duration of the pulses and the accuracy of delay between them. The delay between pump and probe pulses can be set with a delay stage with µm or nm resolution. A laser system using the chirped pulse amplification technique [2] can provide pulses with femtosecond duration, but with typical wavelengths of about 800 nm. However, for the probe pulse, light with shorter and tunable wavelength would be desirable, which can be obtained from conventional synchrotron light sources.

Figure 1.1: The world's oldest example of capturing the phenomenon of motion into a still picture; five sequential images of a Persian ibex on an earthen goblet discovered at the site of the 5200-year-old *Burnt City* in southeastern Iran [1].

1.2 Synchrotron radiation sources

Observed for the first time in 1947 [3], the exceptional properties of synchrotron radiation such as high brightness, good collimation, short wavelength and tunability were realized in the 1960s and employed in studying a variety of samples. Evolving from the first to second generation in the 80s, dedicated storage rings as synchrotron light sources were constructed, producing high-brilliance radiation with tunable wavelengths from infrared to the VUV and hard X-ray regime. In the 90s, the third generation of synchrotron light sources was designed for very

low emittances and with long dedicated straight sections to take full advantage of undulators yielding nowadays peak brilliances of up to 10^{24} photons/(s·mrad^2·mm^2 · 0.1%bw) [4]. Free electron lasers (FEL) as the fourth generation provide peak brilliances many orders of magnitude higher than this [4–7].

Synchrotron radiation pulses are ideally suited to study the structure of matter on the atomic scale. However, with a typical duration of 30-100 ps (FWHM), given by the electron bunch length in a storage ring, they are not capable of resolving ultrafast dynamic phenomena in the sub-picosecond range. Since there are over 50 of these facilities worldwide [8], it is worthwhile to extend the capabilities of conventional synchrotron light sources to shorter pulse duration. The bunch length can be reduced to a few picoseconds by lowering the momentum compaction factor of the storage ring in the so-called low-α mode (e.g., [9]). However, pulses in the femtosecond range are only obtained by extracting synchrotron light from a small fraction of the electron bunch, rather than the whole bunch. This can be achieved with laser-based methods.

1.3 Coherent harmonic generation at DELTA

One of the methods to combine the advantages of synchrotron light sources and short-pulse laser systems is based on the coherent harmonic generation (CHG) principle [10]. CHG has been demonstrated at ACO and Super-ACO [11–13] in Orsay, France, and more recently at UVSOR-II in Okazaki, Japan [14, 15], and ELETTRA in Trieste, Italy [16–18].
Here, a laser pulse interacts with an electron bunch in a first undulator (called modulator) causing a periodic energy modulation and subsequent micro-bunching in a dispersive magnetic chicane, which yields coherent radiation at harmonics of a seed wavelength in the second undulator called radiator.
Additionally, due to path length differences acquired by the off-energy electrons within the bending magnets downstream of the undulator, a sub-millimeter gap in the longitudinal density profile is created, which causes the emission of coherent THz radiation [19].
CHG is capable of producing temporally highly coherent pulses, compared to the spontaneous emission.

A facility employing the CHG principle is commissioned and operated since 2011 at DELTA, a 1.5-GeV electron storage ring at the TU Dortmund University, with the purpose of providing ultrashort coherent VUV radiation for time-resolved user experiments [20–28]. A Ti:sapphire femtosecond laser system is used for seeding, either with its standard wavelength of 800 nm or with its second harmonic, generated in a BBO crystal. Some part of the laser

pulses is guided via an evacuated laser beamline (pump-pulse beamline) to the experimental station at the VUV beamline to conduct pump-probe experiments.

In this work, various properties of the CHG pulses and their dependencies on machine parameters are investigated experimentally. After an introduction to the basic concepts of synchrotron radiation, ultrashort pulses and coherence in Chapter 1, the DELTA storage ring, the CHG facility and the construction of the pump-pulse beamline is described in Chapter 2. Commissioning of the pump-pulse beamline, detection of the CHG pulses in the user VUV beamline, and first proof-of-principle measurements in this beamline in preparation of pump-probe experiments are explained in Chapter 3. In Chapter 4, a comprehensive characterization of the CHG pulses is presented, including the angular and spectral distribution of the CHG pulses, an estimate of their pulse energy and energy modulation, and an experimental investigation of their transverse and longitudinal coherence properties using a double-slit setup and a Michelson interferometer, revealing the high coherence of the CHG pulses. The thesis concludes with a summary and outlook in Chapter 5.

2 Basic Concepts and Theory

In this Chapter, the theoretical framework is provided that underlies the generation of ultrashort VUV pulses and various experimental methods utilized to characterize these pulses. The description of synchrotron radiation mainly follows [29–31], the concept of the laser and ultrashort pulses follows [32, 33], and the coherence part is based on [34, 35].

2.1 Synchrotron radiation

After accelerating a charged particle, the electric field lines close to the particle point radially toward the particle, while at far distances, the field lines point to the position of the particle before the acceleration, causing a distortion in electric field lines in between. The distortion travels away from the particle with the speed of light and is observed as electromagnetic radiation. The radiation field $\vec{E}$ from a relativistic charge q can be calculated by [36]

$$\vec{E}_{\mathrm{r}}(\vec{r},t) = \frac{q}{4\pi\varepsilon_0}\Big(\underbrace{\frac{\hat{n}+\vec{\beta}}{\gamma^2(1+\hat{n}\cdot\vec{\beta})^3|\vec{r}-\vec{r_{\mathrm{s}}}|^2}}_{\text{near field}} + \underbrace{\frac{\hat{n}\times(\hat{n}+\vec{\beta})\times\dot{\vec{\beta}}}{c(1+\hat{n}.\vec{\beta})^3|\vec{r}-\vec{r_{\mathrm{s}}}|}}_{\text{far field}}\Big)_{t_{\mathrm{r}}}, \tag{2.1}$$

where all quantities are evaluated at the *retarded time* $t_{\mathrm{r}} = t - R(t_{\mathrm{r}})/c$ indicated by the index "r", γ is the Lorentz factor, $\vec{\beta} = \vec{v}/c$ is the velocity of the particle, and $\vec{r} - \vec{r_{\mathrm{s}}} = \vec{R}$ is the vector from the observation point $\vec{r}$ to the charged particle (radiation source) at $\vec{r_{\mathrm{s}}}$. Furthermore, $\hat{n}(t_{\mathrm{r}}) = \vec{R}/|\vec{R}|$ is the direction of observation, c the light speed and ϵ_0 is the vacuum permittivity.
The first term of the radiation field in Eq. 2.1 is the Coulomb field of the charged particle at rest or at uniform motion and is proportional to $1/R^2$ (dominating in the near field). The second term is proportional to the acceleration of the particle $\dot{\vec{\beta}}$ and to $1/R$ (dominating in the far field). The *Poynting vector*

$$\vec{S} = [\frac{1}{\mu_0 c}\vec{E}\times\vec{B}]_{\mathrm{r}} = \varepsilon_0 c[\vec{E}\times(\vec{E}\times\hat{n})]_{\mathrm{r}} = -\varepsilon_0 c\vec{E}^2\,\hat{n}|_{\mathrm{r}}; \quad (\vec{B} = \frac{1}{c}[\vec{E}\times\hat{n}]_{\mathrm{r}}; \quad \vec{E}\perp\hat{n}) \tag{2.2}$$

defines the energy flux density (intensity) of synchrotron radiation per unit cross section at the observation point $\vec{r}$ and time t, and parallel to the direction of propagation $\hat{n}$. The Poynting vector is used to determine the angular and spectral distribution of the radiation.

The synchrotron radiation power per unit solid angle at distance R from the source in a co-moving frame with the charge is [29]

$$\frac{dP}{d\Omega} = -(\hat{n}\cdot\vec{S})R^2|_{\mathrm{r}} = \varepsilon_0 c R^2 \vec{E}^2|_{\mathrm{r}}. \tag{2.3}$$

The energy per unit solid angle is obtained by integrating the radiation power over time

$$\frac{dW(t)}{d\Omega} = -\int_{-\infty}^{\infty}\frac{dP}{d\Omega}dt = \varepsilon_0 c\int_{-\infty}^{\infty} R_{\mathrm{r}}^2\left|\vec{E}_{\mathrm{r}}(t)\right|^2 dt. \tag{2.4}$$

When the charged particles are deflected transversely by a magnetic field, e.g. by a bending magnet in a storage ring, they emit synchrotron radiation. In order to determine the spectrum of the synchrotron radiation, the Fourier transformation is applied on the electric field, yielding

$$\frac{dW(\omega)}{d\Omega} = \frac{\varepsilon_0 c}{\pi}R_{\mathrm{r}}^2\int_0^{\infty}\left|\vec{E}_{\mathrm{r}}(\omega)\right|^2 d\omega \tag{2.5}$$

with $\omega = 2\pi\nu$ and ν being the radiation frequency. By inserting the far-field term from Eq. 2.1 into the frequency domain (Eq. 2.5), assuming an electron as the charged particle, and using the relation $dt/dt_{\mathrm{r}} = r/R(t_{\mathrm{r}}) = (1-\hat{n}\cdot\vec{\beta})$, the energy per unit solid angle and frequency is obtained

$$\frac{d^2W}{d\Omega d\omega} = \varepsilon_0\frac{c}{\pi}R_{\mathrm{r}}^2\left|\vec{E}_{\mathrm{r}}(\omega)\right|^2 = \frac{e^2}{16\pi^3\varepsilon_0 c}\left|\int_{-\infty}^{\infty}\frac{\hat{n}\times\left[\left(\hat{n}+\vec{\beta}\right)\times\dot{\vec{\beta}}\right]}{\left(1+\hat{n}\cdot\vec{\beta}\right)^2}e^{i\omega(t_{\mathrm{r}}+\frac{\vec{R}_{\mathrm{r}}}{c})}dt_{\mathrm{r}}\right|_{\mathrm{r}}^2. \tag{2.6}$$

Equations 2.1 to 2.6 are the basis of synchrotron radiation calculation codes such as *Spectra* [37]. A more detailed discussion of the radiation properties can be found in [29].

Synchrotron radiation from a bending magnet

Considering the trajectory of an electron in a bending magnet as an arc with a constant radius ρ, the average synchrotron radiation power reads

$$P_\gamma = \frac{2}{3}r_c\frac{mc^3\beta^4\gamma^4}{\rho^2} \tag{2.7}$$

with $r_c = e^2/4\pi\epsilon_0 mc^2$ being the classical electron radius and $\gamma = 1/\sqrt{1-\beta^2}$ being the Lorentz factor. The synchrotron radiation from a relativistic particle in the observer's reference frame is collimated in the forward direction within an rms half angle of $\theta_{\mathrm{rms}} \approx 1/\gamma$ and is emitted over a wide range of frequencies. The spectral distribution of the synchrotron radiation from a particle in a bending magnet reads [29]

$$\frac{dP}{d\omega} = \frac{P_\gamma}{\omega_c} S(\omega/\omega_c); \qquad S(\omega/\omega_c) = \frac{9\sqrt{3}}{8\pi}\frac{\omega}{\omega_c}\int_{\omega/\omega_c}^{\infty} K_{5/3}(x)\,\mathrm{d}x. \tag{2.8}$$

Here, $K_{5/3}$ is the modified Bessel function of second kind, $\omega_c = 3c\gamma^3/\rho$ is the so-called critical frequency and $S(\omega/\omega_c)$ is the universal synchrotron radiation function shown in Fig. 2.1.

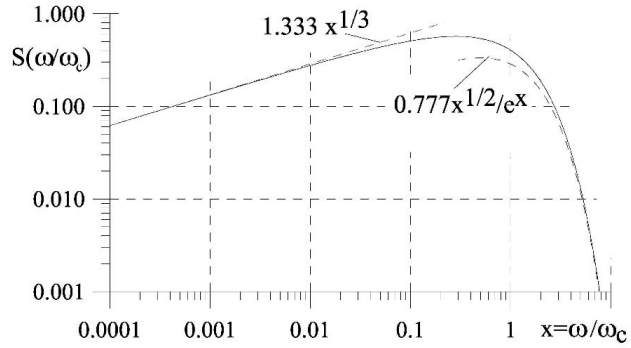

Figure 2.1: Universal synchrotron radiation function $S(\omega/\omega_c)$ for a bending magnet [29].

2.1.1 Insertion devices

Insertion devices such as *undulator* and *wiggler* produce radiation with optimized properties to meet the needs of research with synchrotron radiation. They are inserted along a straight section in a storage ring. An undulator/wiggler is a sequence of alternating magnetic dipoles with a period length of λ_u between like-sign poles. Electrons are periodically deflected transversely by a sinusoidal magnetic field, and they radiate in forward direction. Radiation fields from various parts of the trajectory in an undulator overlap and interfere, resulting in nearly monochromatic light that includes a fundamental wavelength together with its harmonics.

For the electrons, the undulator period appears shortened by the Lorentz factor γ due to the length contraction $\lambda_\mathrm{u}^* = \lambda_\mathrm{u}/\gamma$. The radiation wavelength observed in the laboratory system is shortened by another factor of γ due to the Doppler shift.

The scheme of an undulator, particle trajectory and radiation emission is illustrated in Fig. 2.2. The longitudinal direction is denoted by s, the horizontal direction by x, and the

vertical direction by y. Assuming an infinite horizontal magnet extent, the x component of the magnetic field is zero.

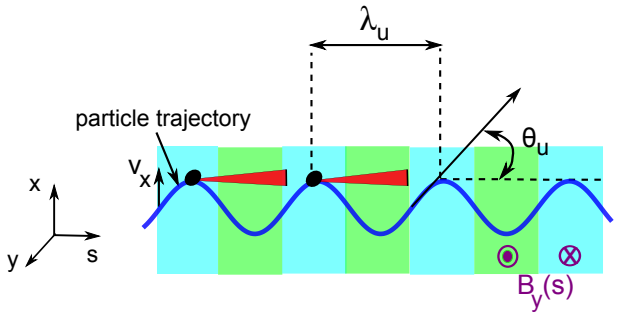

Figure 2.2: Particle trajectory (blue curve in the x-s plane) and emission of radiation in an undulator with undulator period λ_u, the maximum trajectory angle of θ_u and magnetic field $B_y(s)$ in y direction. The bending angle of the particle in this diagram has been exaggerated.

The on-axis ($y = 0$), magnetic field of an undulator $B_\mathrm{y}(s)$ and the definition of the undulator/wiggler deflection parameter K is as follows

$$B_y(s) = \tilde{B}\cos(k_\mathrm{u}s)\ ; \quad k_\mathrm{u} = \frac{2\pi}{\lambda_\mathrm{u}} \tag{2.9}$$

$$K = \frac{\lambda_\mathrm{u} e\tilde{B}}{2\pi m_\mathrm{e} c}, \tag{2.10}$$

where $\tilde{B}$ is the peak magnetic field along the beam axis s and m_e is the electron mass. By solving the equation of motion for an electron with a velocity of $\beta = v/c$ in the x-s plane under the Lorentz force $\vec{F} = e\vec{v} \times \vec{B}$, the particle trajectory and the maximum trajectory angle θ_u in the laboratory frame is given by [30]

$$x(t) = -\frac{K}{k_\mathrm{u}\gamma}\cos(\omega_\mathrm{u}t)\ ; \quad \omega_\mathrm{u} = k_\mathrm{u}\beta c = \frac{2\pi}{\lambda_\mathrm{u}}c \tag{2.11}$$

$$s(t) = \beta^* ct + \frac{K^2}{8k_\mathrm{u}\gamma^2}\sin(2\omega_\mathrm{u}t) \tag{2.12}$$

$$\text{with } \beta^* = \beta\left[1 - \frac{1}{2\gamma^2}(1 + \frac{K^2}{2})\right] \tag{2.13}$$

$$\theta_\mathrm{u} = \frac{K}{\gamma}, \tag{2.14}$$

where $\beta^* = \dot{\bar{s}}/c$ is the average relative velocity of the electron in the laboratory reference

frame.

The position of particles relative to the reference particle (the particle at the nominal position) is described by a (6×1) vector $\vec{X} = (x(s),\, x'(s),\, y(s),\, y'(s),\, \Delta z,\, \Delta p/p)$, with Δz being the longitudinal deviation from the reference, p being the momentum of the nominal particle and Δp the deviation from this value. The prime denotes the derivative with respect to s. For a reference particle, all the elements of this vector are zero. Each element in a storage ring (e.g. free drift space, bending magnet, quadrupole magnet) can be represented by a (6×6) transfer matrix M which acts on the six-dimensional electron vector like $\vec{X_1} = M\vec{X_0}$, where $\vec{X_0}$ ($\vec{X_1}$) is the position at the beginning (end) of the element.

Undulator radiation

The resonance condition for constructive interference and hence the fundamental wavelength of the undulator radiation is given by [30]

$$\lambda_{\mathrm{res}}(\theta) = \frac{\lambda_{\mathrm{u}}}{2\gamma^2}\left(1 + \frac{K^2}{2} + \gamma^2\theta^2\right). \tag{2.15}$$

The resonance frequency depends on the deflection parameter K, the undulator period λ_{u} and the beam energy γ, and also on the observation angle θ. With increasing angle, the radiation wavelength increases (red shifted).

To move along one undulator period, the electron takes the time $\tau_{\mathrm{u}} = \lambda_{\mathrm{u}}/c\beta^*$. Within the same time, the radiation front proceeds a distance of $s_{\mathrm{u}} = \tau_{\mathrm{u}}c$, moving ahead of the particle. For a constructive superposition of the radiation from all undulator periods, the path difference $s_{\mathrm{u}} - \lambda_{\mathrm{u}}\cos(\theta)$ should be the radiation wavelength λ_{res} which yields Eq. 2.15.

By substituting the electron trajectory into Eq. 2.6, the energy of the on-axis radiation per unit frequency and solid angle for one electron from a planer undulator with N_{u} periods reads

$$\frac{d^2I}{d\Omega d\omega} = \frac{e^2}{4\pi\varepsilon_0 c}\left(\frac{KN_{\mathrm{u}}\lambda_{\mathrm{res}}}{\gamma}\right)^2 \sum_{n=1}^{\infty} \frac{A_n^2}{\lambda^2}\left(\frac{\sin(\delta_n)}{\delta_n}\right)^2 \tag{2.16}$$

$$\text{with } A_n \approx J_{\frac{n+1}{2}}\left(\frac{nK^2}{4+2K^2}\right) - J_{\frac{n-1}{2}}\left(\frac{nK^2}{4+2K^2}\right), \text{ and } \delta_n = \pi N_{\mathrm{u}}(n - \frac{\lambda_{\mathrm{res}}}{\lambda}), \tag{2.17}$$

where J_{n} is a Bessel function of the first kind, and n is the harmonic number. The angular distribution includes different radiation lobes that depend on the frequency, emission angle,

and polarization. Two polarization directions have been defined for the radiation field: in σ-mode, the radiation has an electric field in the plane of the particle path, in π-mode, the polarization is orthogonal to the sigma-mode. For the fundamental wavelength in the forward direction ($\theta = 0$), there is a strong radiation lobe in σ-mode, while there is no emission in π-mode.

When the electric field deviates from a sinusoidal shape, higher harmonics appear in the radiation spectrum (examples are shown in [29–31]). For the second harmonic, the π-mode radiation in the forward direction vanishes. There is no forward radiation for even harmonics.

The spectrum of the radiation for the first harmonic ($n = 1$ in Eq. 2.16) can be written as

$$I_{\mathrm{und}}(\lambda) \propto \left(\frac{\sin(\chi)}{\chi}\right)^2 \; ; \quad \chi = \pi N_{\mathrm{u}} \frac{\Delta\lambda}{\lambda} \; ; \quad \Delta\lambda = \lambda - \lambda_{\mathrm{res}}. \tag{2.18}$$

For an undulator with small K value, the radiation spectrum has a peak with a width of about $1/N_{\mathrm{u}}$ at the fundamental wavelength, and at higher harmonics the radiation intensity decreases. As the K value increases, the intensity of the higher harmonics increases until the spectrum is similar to the continuous spectrum of dipole radiation (Fig. 2.1).

Dispersive chicane and optical klystron

Storage ring FELs [38, 39] have a very low gain compared to self-amplified spontaneous emission (SASE) FELs [5] due to their limited undulator length and low peak current. In order to increase the gain to at least a few percent, a configuration called *optical klystron* [38–40] is used which is a modification of an undulator.

An optical klystron (OK) consists of two undulators and one disperive magnetic chicane between them . When passing through a magnetic dispersive section, charged particles undergo different trajectories depending on their energy. Their longitudinal deflection (Δz) depends on the magnetic configuration of the chicane via the r_{56} element of its transfer matrix M as

$$\Delta z = r_{56} \frac{\Delta p}{p}. \tag{2.19}$$

The r_{56} value of a chicane of length L can be determined by integrating over the squared

integral of the magnetic field along the chicane [28]

$$r_{56} = \frac{L}{{\gamma_0}^2} + \left(\frac{e}{cm_0\gamma_0}\right)^2 \int_0^s \left(\int_0^s B(s')ds'\right)^2 ds. \tag{2.20}$$

The radiation from an optical klystron is the interference of the radiation from two undulators tuned to the same wavelength with a delay caused by the chicane which depends on the strength of the chicane r_{56}. By introducing a new parameter $N_\mathrm{d} = r_{56}/(2\lambda)$, the number of undulator-period equivalent of the dispersive section, the spectrum of the radiation can be derived to be [40]

$$I_\mathrm{OK}(\lambda) = 2I_\mathrm{und}\left(1 + f\ \cos\left(2\pi(N_\mathrm{d} + N_\mathrm{u})\frac{\Delta\lambda}{\lambda}\right)\right)\ ; \quad \Delta\lambda = \lambda - \lambda_\mathrm{res} \tag{2.21}$$

The width of the spectrum and that of the fringes in the spectrum is

$$(\Delta\lambda/\lambda)_\mathrm{s} = 1/N_\mathrm{u}\ ; \qquad (\Delta\lambda/\lambda)_\mathrm{f} = 1/(N_\mathrm{d} + N_\mathrm{u}), \tag{2.22}$$

respectively. The spectrum of the radiation from the optical klystron (U250) at the DELTA storage ring (see Section 3.1) is shown in Fig 2.3. In this example, a value of $r_{56} = 27.5$ µm is obtained by fitting the experimental data to Eq. 2.21.

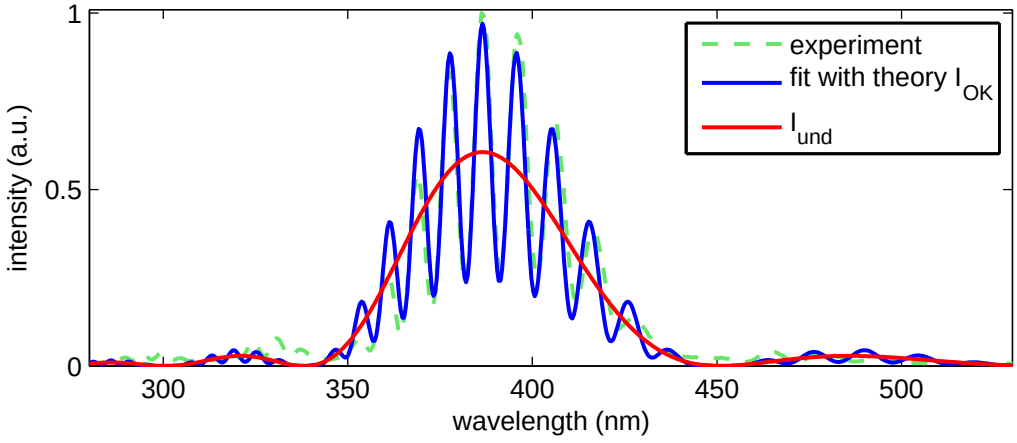

Figure 2.3: Spectrum of the synchrotron radiation from the optical klystron at DELTA with $N_\mathrm{u} = 7$, $\lambda_\mathrm{u} = 25$ cm and $r_{56} = 27.5$ µm.

2.2 Femtosecond laser pulses

Ultrashort high-power femtosecond laser pulses can be generated with mode-locked lasers using the chirped pulse amplification technique [2,33], in which the laser pulse is stretched temporally prior to amplification to lower the peak intensity, and recompressed after amplification. These pulses exhibit special properties and effects in a medium due to their short duration and high peak power.

Generally, the temporal dependence of the electric field and the intensity of an electromagnetic wave in a material of refractive index n can be expressed like [33]

$$E(t) = \tilde{\mathcal{E}}(t)e^{i\omega_0 t}; \quad \tilde{\mathcal{E}}(t) = \mathcal{E}(t)e^{i\varphi(t)}, \qquad I(t) = \epsilon_0 cn\mathcal{E}^2, \tag{2.23}$$

where $\tilde{\mathcal{E}}(t)$ is the complex field envelope, $\mathcal{E}(t) = |\tilde{\mathcal{E}}(t)|$ is the field envelope, ω_0 is the carrier frequency, and $\varphi(t)$ is the time-dependent phase. The spectrum of the field can be derived by Fourier transformation ($\mathcal{F}$)

$$E(\Omega) = \mathcal{F}\{E(t)\} = \int_{-\infty}^{\infty} E(t)e^{-i\Omega t}dt = |E(\Omega)|e^{i\Phi(\Omega)} \tag{2.24}$$

$$I(\Omega) = \epsilon_0 cnE^2(\Omega). \tag{2.25}$$

Here, $|E(\Omega)|$ denotes the spectral amplitude, $I(\Omega)$ denotes the spectral intensity and $\Phi(\Omega)$ denotes the spectral phase. The spectral width (FWHM of the spectral intensity) $\Delta\nu_\mathrm{p} = \Delta\omega_\mathrm{p}/2\pi$ and the pulse duration τ_p (FWHM of the intensity profile) are related to each other, and there is a minimum value for their product ("time-bandwidth product")

$$\Delta\nu_\mathrm{p}\ \tau_\mathrm{p} \geq c_B, \tag{2.26}$$

where c_B is a numerical constant of the order of one, depending on the pulse shape e.g. $c_B = 0.44$ for a Gaussian pulse. A pulse for which the equality holds is called "Fourier limited" or "bandwidth limited". The carrier frequency in general can be time-dependent

$$\omega(t) = \omega_0(t) + \frac{d}{dt}\varphi(t). \tag{2.27}$$

If $d\varphi(t)/dt = f(t)$ is not constant, the pulse is called "frequency modulated" or "chirped". If

$d^2\varphi(t)/dt^2$ is positive (negative), the carrier frequency increases (decreases) along the pulse, and the pulse is called up- (down-) chirped. A positive chirp is shown in Fig. 2.4(a) for a Gaussian pulse. If $d\varphi(t)/dt$ is a constant, only a frequency shift is added to ω_0.

The parameters of laser pulses can be altered by passing through a transparent medium. The *group velocity* v_g, *group velocity dispersion GVD*, *group delay* T_g and *group delay dispersion GDD* are defined by

$$v_\mathrm{g} = \left(\frac{\partial k}{\partial \omega}\right)^{-1} = c\left(n(\omega) - \omega\frac{dn}{d\omega}\right)^{-1} = \frac{c}{n_g(\omega)}; \qquad T_g = \frac{\partial \varphi}{\partial \omega}\,, \tag{2.28}$$

$$\mathrm{GVD} = \frac{\partial}{\partial \omega}\frac{1}{v_g} = \frac{\partial^2 k}{\partial \omega^2}\,; \qquad \mathrm{GDD} = \frac{dT_g}{d\omega} = \frac{\partial^2 \varphi}{\partial \omega^2}, \tag{2.29}$$

where $k = 2\pi/\lambda$ is the wavenumber, $\omega = 2\pi\nu$ is the angular frequency, $\varphi(\omega)$ is the spectral phase, $n(\omega)$ is the index of refraction, and n_g is called the group index. The envelope moves at the group velocity. Since the group velocity of light in a transparent medium depends on the frequency (dispersion), a chirped pulse will be temporally stretched or compressed, depending on the sign of the chirp.

After passing through a transparent medium with known GDD, the duration of a Gaussian pulse with a Fourier-limited duration of τ_p0 is

$$\tau_\mathrm{p} = \sqrt{{\tau^2}_\mathrm{p0} + \left(\frac{4\ln 2\ \mathrm{GDD}}{\tau_\mathrm{p0}}\right)^2}. \tag{2.30}$$

As can be seen, the shorter the pulse length the stronger the effect of the GDD.

Gaussian Optics

The temporal dependence of the electric field *E(t)* and the intensity *I(t)* (see Eq. 2.23) in a Gaussian pulse is [33]

$$\mathcal{E}(t) = \mathcal{E}_0 \exp\left(-\frac{t^2}{\tau_0^2}\right) = \mathcal{E}_0 \exp\left\{-1.385\ \left(\frac{t^2}{\tau_\mathrm{p}^2}\right)\right\} \tag{2.31}$$

$$I(t) = I_0 \exp\left(-\frac{2t^2}{\tau_0^2}\right) = I_0 \exp\left(-\frac{t^2}{2\sigma_t^2}\right), \tag{2.32}$$

where $\tau_\mathrm{p} = 2\sqrt{2\ln 2}\cdot\sigma_\mathrm{t} = 2.355\,\sigma_\mathrm{t}$ is the FWHM of the electric field envelope, $\tau_0 =$

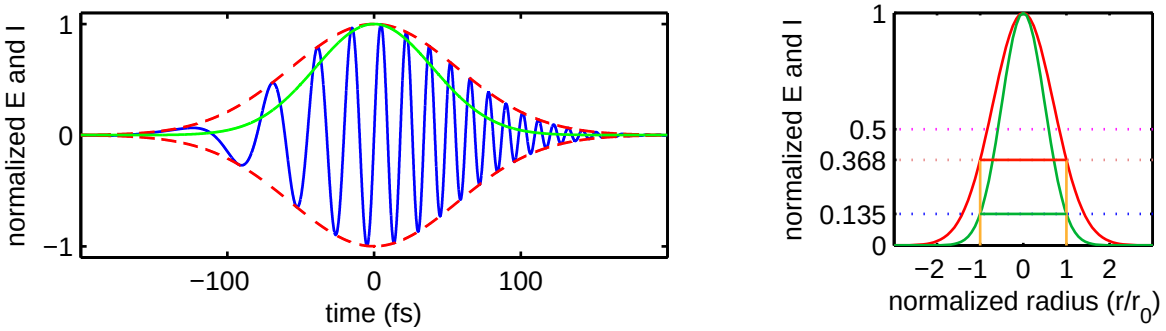

(a) (b)

Figure 2.4: a) Temporal profile of a chirped pulse: the electric field $E(t)$ is represented by a solid blue line. The envelope of the field $|\tilde{\mathcal{E}}(t)| = \mathcal{E}(t)$ is the dashed red line, and the intensity $I(t)$ is the green line. b) Radial profile of the electric field (red curve) and the intensity (narrow green curve) of a Gaussian beam; the $1/e = 0.368$ width of the electric field and $1/e^2 = 0.135$ width of the intensity are shown by red and green lines, respectively.

$\tau_\mathrm{p}/\sqrt{2\,\ln 2} = \tau_\mathrm{p}/\sqrt{1.385} = 2\,\sigma_\mathrm{t}$ is the $1/e \simeq 0.368$ half width of the field envelope (equal to the $1/e^2 \simeq 0.135$ half width of the intensity; see Fig. 2.4(a)), and σ_t is the standard deviation of the temporal profile of a Gaussian beam.

A linearly chirped pulse ($d\varphi/dt = -2at/{\tau_0}^2$) is given by [33]

$$\tilde{\mathcal{E}}(t) = \mathcal{E}_0 \exp\left(-(1+ia)\frac{t^2}{\tau_0^2}\right). \tag{2.33}$$

By applying a Fourier transformation, the spectral intensity can be derived, which has a Gaussian shape. The FWHM width of the spectral intensity and the time-bandwidth product can be found to be [33]

$$\Delta\nu_\mathrm{p} = \frac{1}{\tau_0}\sqrt{8\,\ln 2\,(1+a^2)}; \qquad \Delta\nu_\mathrm{p}\;\tau_\mathrm{p} = \frac{2\,\ln 2}{\pi}\sqrt{1+a^2} \approx 0.44\sqrt{1+a^2}. \tag{2.34}$$

The occurrence of the chirp ($a \neq 0$) increases the time-bandwidth product exceeding the Fourier limit. Figure 2.4(a) shows the electric field for an up-chirped pulse with $\sigma_\mathrm{t} = 80$ fs and a wavelength of $\lambda = 400$ nm. The transverse profile of a Gaussian electric field (shown in Fig.2.4(b)) is given by [33]

$$\mathcal{E}(r) = \mathcal{E}_0 \exp\left(-\frac{r^2}{{r_0}^2}\right) = \mathcal{E}_0 \exp\left\{-1.385\;\left(\frac{r^2}{r_\mathrm{p}^2}\right)\right\} \tag{2.35}$$

$$I(r) = I_0 \exp\left(-\frac{2r^2}{r_0^2}\right) = I_0 \exp\left(-\frac{r^2}{2\sigma_r^2}\right), \tag{2.36}$$

where r is the radial distance from the axis of the beam, the $r_\mathrm{p} = 2\sqrt{2\,\ln 2}\cdot\sigma_\mathrm{r} = 2.355\,\sigma_\mathrm{r}$ is the FWHM width of the electric field, $r_0 = r_\mathrm{p}/\sqrt{2\,\ln 2} = r_\mathrm{p}/\sqrt{1.385} = 2\,\sigma_\mathrm{r}$ is the $1/e \simeq 0.368$ radius of the field (equal to the $1/e^2 \simeq 0.135$ radius of the intensity; see Fig. 2.4(b)), and σ_r is the standard deviation of the transverse profile of a Gaussian beam.

Propagation of a Gaussian beam

The amplitude of the Gaussian beam intensity along the propagation direction z and radial axis of the beam r can be written as [32]

$$I(r,z) = I_0 \left(\frac{w_0}{w(z)}\right)^2 \exp\left(\frac{-2r^2}{w^2(z)}\right), \tag{2.37}$$

where z is the axial distance from the "waist" w_0 (shown in Fig. 2.5). The radius of the laser *w(z)* at distance z is given by [32]

$$w(z) = w_0\sqrt{1+\left(M^2\frac{z}{z_\mathrm{R}}\right)^2} = w_0\sqrt{1+\left(M^2\frac{\lambda z}{\pi {w_0}^2}\right)^2}, \tag{2.38}$$

where $M^2 \geq 1$ is the beam quality factor. For a perfect Gaussian pulse, M^2 is equal to 1. The *Rayleigh length* z_R, the distance along the propagation axis at which the beam size increases by a factor of $\sqrt{2}$ and the area of the beam is doubled, is given by

$$z_\mathrm{R} = \frac{\pi {w_0}^2}{\lambda} \quad , \quad w(\pm z_\mathrm{R}) = \sqrt{2}w_0. \tag{2.39}$$

Twice the Rayleigh length is called the depth of focus of the beam. Far from the waist, the beam is cone-shaped and its opening angle is called the divergence of the beam

$$\theta_\mathrm{div} \approx \frac{w(z)}{z}(z\to\infty)\,; \qquad \theta_\mathrm{div} \simeq M^2\frac{w_0}{z_R} = M^2\frac{\lambda}{\pi w_0}. \tag{2.40}$$

Gaussian beam propagation is illustrated in 2.5.

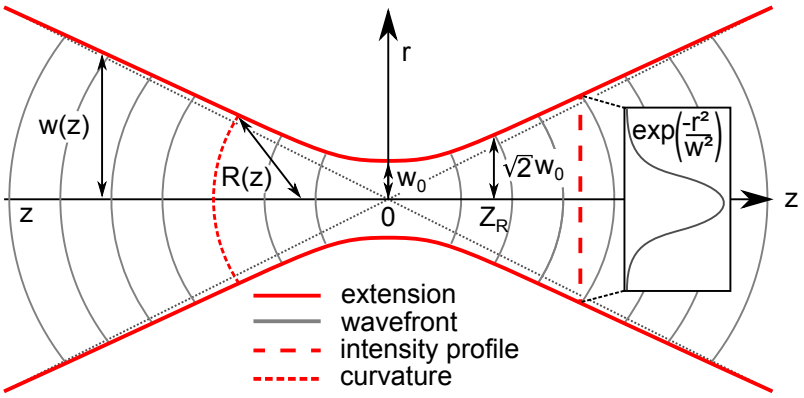

Figure 2.5: Propagation of a Gaussian beam [44].

The radius of curvature of the wavefronts is a function of position [32]

$$R(z) = z\left[1 + \left(\frac{z_\mathrm{R}}{z}\right)^2\right] \ . \tag{2.41}$$

The propagation of a Gaussian beam can be expressed by using ray transfer matrices. For this purpose a complex beam parameter $q(z)$ is defined as [32]

$$q(z) = z + q_0 = z + iz_\mathrm{R} \ ; \qquad q(z=0) = q_0 = iz_\mathrm{R}. \tag{2.42}$$

The reciprocal $1/q(z)$ shows the relationship between $q(z), w(z)$ and $R(z)$

$$\frac{1}{q(z)} = \frac{1}{z + iz_\mathrm{R}} = \frac{z}{z^2 + z_\mathrm{R}^2} - i\frac{z_\mathrm{R}}{z^2 + z_\mathrm{R}^2} = \frac{1}{R(z)} - i\frac{\lambda}{\pi w^2(z)}. \tag{2.43}$$

The effect of any optical element can be calculated using its transfer matrix M. Assuming that the incident beam has a radius of r_in and a divergence of θ_in, the output beam radius r_out and divergence θ_out is derived in geometrical optics by

$$\begin{pmatrix} r \\ \theta \end{pmatrix}_\mathrm{out} = M \times \begin{pmatrix} r \\ \theta \end{pmatrix}_\mathrm{in} \ . \tag{2.44}$$

In Gaussian optics, the properties of the output beam q_out for incident beam q_in are derived

by

$$\begin{pmatrix} q \\ 1 \end{pmatrix}_{\text{out}} = mM \times \begin{pmatrix} q \\ 1 \end{pmatrix}_{\text{in}}, \tag{2.45}$$

where $m = 1/(Cq_{\text{in}} + D)$ is a normalization constant chosen to keep the second component of the ray vector equal to 1. Defining $M = \begin{pmatrix} A & B \\ C & D \end{pmatrix}$, one can derive [32]

$$q_{\text{out}} = \frac{Aq_{\text{in}} + B}{Cq_{\text{in}} + D}. \tag{2.46}$$

2.2.1 Nonlinear effects

Ultrashort laser pulses have high peak power and intensity causing nonlinear effects such as second/third harmonic generation and the Kerr effect. When intense light propagates in a transparent medium such as gas or glass, its properties are modified due to the nonlinear response of the medium to the applied electric field. The polarization of laser light is not anymore a linear function of the electric field and can be written as a series expansion [33]

$$P = \underbrace{\epsilon_0 \chi^{(1)} \mathcal{E}}_{\text{linear}} + \underbrace{\epsilon_0 \chi^{(2)} \mathcal{E}^2}_{\text{SHG}} + \underbrace{\epsilon_0 \chi^{(3)} \mathcal{E}^3}_{\text{Kerr effect}} + \dots, \tag{2.47}$$

where ϵ_0 is the vacuum permeability and $\chi^{(n)}$ is the n-th order frequency-dependent electric susceptibility of the medium.

Measuring the pulse duration of ultrashort pulses is not possible with conventional methods such as power measurement by a photodiode. Even the fastest available detectors with a response time of 10^{-13} to 10^{-12} s can not resolve directly the details of femtosecond pulses, therefore indirect methods including autocorrelators based on various nonlinear effects are used to measure the pulse shape.

Second harmonic generation (SHG) or frequency doubling is a nonlinear process in which two photons are combined and a photon with a doubled frequency is generated. The sum of the wave vectors of the fundamental photons $\vec{k}_{1,2}$ is equal to the wave vector of the resulting photon $\vec{k}_1 + \vec{k}_2 = \vec{k}$ (*phase matching*). Practically, this is carried out by placing a nonlinear medium such as lithium triborate (LBO) or β-barium borate (BBO) in a laser beam. In an intensity autocorrelator (SHG+autocorrelator), the incident pulse is divided into two parts,

and one part is delayed by τ with respect to the other. Both signals pass through a nonlinear crystal with a small angle between then (see Fig. 2.6 left), and the intensity of the generated second harmonic depends on the delay. After passing through a filter or an aperture, the fundamental wavelength is eliminated, the beam is focused on a detector, and the SHG signal is measured. In an *interferometric autocorrelation*, a nonlinear crystal is placed after a Michelson interferometer. A filter is used to eliminate the fundamental wavelength. Simplified setups of an intensity and an interferometric autocorrelator are sketched in Fig. 2.6.

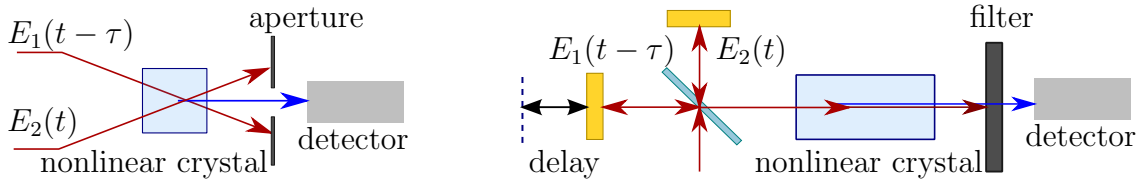

Figure 2.6: A simplified sketch of (left) an intensity autocorrelation and (right) an interferometric autocorrelation setup.

The intensity A_I and the interferometric G_int autocorrelation functions are given by [33]

$$A_\mathrm{I}(\tau) = \int_{-\infty}^{\infty} I(t)I(t-\tau)dt \overset{\mathcal{F}}{\Longrightarrow} \quad A_\mathrm{I}(\Omega) = \tilde{\mathcal{I}}(\Omega)\tilde{\mathcal{I}}^*(\Omega) \tag{2.48}$$

$$G_\mathrm{int}(\tau) = \int_{-\infty}^{\infty} \left\{[E_1(t-\tau) + E_2(t)]^2\right\}^2 dt, \tag{2.49}$$

where $A_\mathrm{I}(\Omega)$ and $\tilde{\mathcal{I}}$ are the Fourier transform of $A_\mathrm{I}(\tau)$ and $I(t)$, respectively. The width of A_I is related to the width of the intensity distribution, e.g. it is $\sqrt{2}$ times the width of the intensity for a Gaussian pulse [33]. The interferometric autocorrelation signal (together with the spectrum) can be used to determine the pulse shape and chirp [33].

Furthermore, in another technique called frequency-resolved optical gating (FROG), the detector is replaced by a spectrometer. This corresponds to a spectrally resolved autocorrelator and yields the intensity, the duration and the phase of a pulse [43]. Another technique is spectral phase interferometry for direct electric-field reconstruction (SPIDER), which uses the spectral interferogram of two identical but spectrally shifted pulses and yields phase information, and combined with independently measured spectra gives also amplitude information [45].

The *optical Kerr effect* is the variation of the refractive index due to the nonlinear response of the medium to ultrashort pulses with high peak intensity I

$$n = n_0 + n_{2E}\langle\mathcal{E}^2\rangle = n_0 + n_{2I}I \tag{2.50}$$

with n_{2I} being the nonlinear index. Transversely, the delay is largest on the beam axis where the intensity is highest. Due to this effect, the wavefronts are deformed, so that the pulse is transversely focused (assuming $n_{2I} > 0$) which is called "self-focusing". In addition, the temporal dependence of the phase shift leads to *self-phase modulation (SPM)*, changing the spectrum of the pulse. As a measure of nonlinear interaction over length L, the so-called B *integral* is defined by [32]

$$B = \frac{2\pi}{\lambda} \int_0^L n_{2\mathrm{I}} I(z)\, \mathrm{d}z. \tag{2.51}$$

Generally, in order to avoid nonlinear distortion effects due to self-phase modulation or self focusing, the B integral must be kept below the value 5 [32].

Two-photon absorption (TPA) is a nonlinear optical phenomenon in which two photons with equal or unequal energies are simultaneously absorbed by an electronic transition in an atom. The first photon takes the atom from the initial state i to a virtual state v, and the second takes it from v to the final state f. The absorption coefficient is proportional to the optical intensity. By using a material in which TPA occurs for a certain wavelength, the pulse duration can be estimated as the two-photon-absorption signal increases when the temporal overlap between two beams decreases. A SiC photodiode can be used to detect a two-photon-induced photocurrent from 800-nm and 400-nm, or from two 400-nm laser beams (Fig. 2.7). The photoelectrons from the photodiode due to TPA can be measured with a simple amperemeter.

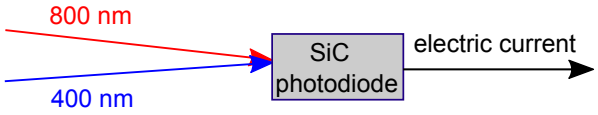

Figure 2.7: Two-photon absorption using a photodiode.

2.3 Coherence and interference

In this Section, the formation of diffraction and interference patterns of an electromagnetic wave and their dependence on the transverse and temporal coherence of the wave are studied. Firstly, the coherence properties for an electromagnetic wave are defined in terms of the cross-correlation of the field, and then the coherence properties of synchrotron radiation are discussed.

Coherence of an electromagnetic wave train is a measure of the correlation between the phases at different points along or transverse to the direction of propagation ($\vec{k}/k$). In Fig. 2.8, wavefronts of a forward-traveling electromagnetic wave pulse are sketched, showing two points marked in longitudinal direction (t_1, t_2) or transverse direction $(\vec{r}_1, \vec{r}_2)$ which could be selected by splitting and delaying the beam or by dividing the wavefront using a double slit.

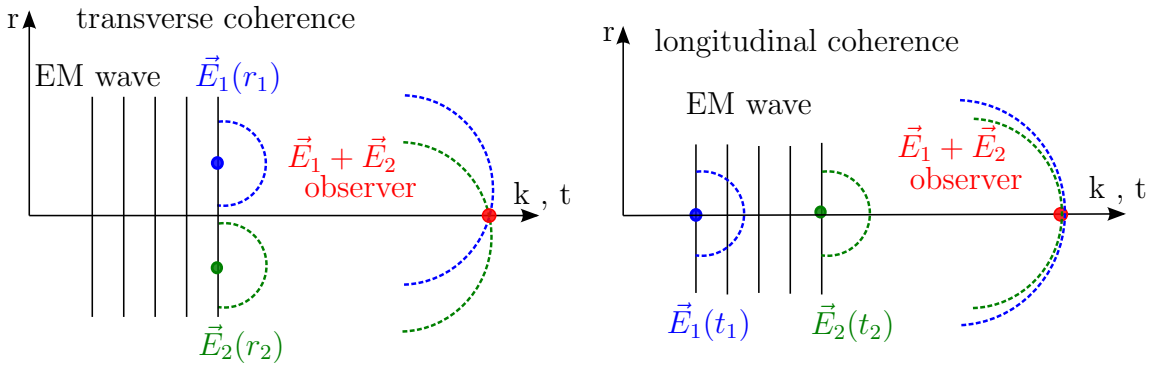

Figure 2.8: The coherence concept for an electromagnetic (EM) wave pulse. Schematic depiction of wavefronts of an electromagnetic wave is shown with two points marked in transverse direction $(\vec{r}_1, \vec{r}_2)$ and longitudinal direction (t_1, t_2), and a red dot denoting the position of the observer. The distance traveled by $E_2(t_2)$ from t_2 to the observer is shorter than that of $E_1(t_1)$ from t_1.

Coherence theory studies the correlation properties of the light whose phase, frequency and wavelength vary randomly with respect to time. In the slowly-varying-amplitude approximation, it is assumed that the amplitude of a forward-traveling wave pulse varies slowly in time and space compared to a period or wavelength. In this case, the propagation of an electromagnetic wave, linearly polarized in x direction is described as

$$\vec{E}(\vec{r}, t) = \mathrm{Re}[\tilde{E} \exp{(i(\omega t - \vec{k} \cdot \vec{r}))}]\vec{u}_\mathrm{x} \tag{2.52}$$

with $\tilde{E}$ the complex amplitude. The total intensity at the position of an observer located at

the origin of the coordinate system reads

$$I_{\mathrm{tot}}(\vec{r}_1,t_1;\vec{r}_2,t_2) \propto \vec{E}_{\mathrm{tot}}^2 = \left[\vec{E}(\vec{r}_1,t_1)+\vec{E}(\vec{r}_2,t_2)\right]^2 \tag{2.53}$$

$$I_{\mathrm{tot}}(\vec{r}_1,t_1;\vec{r}_2,t_2) \propto \underbrace{\left\langle |E(\vec{r}_1,t_1)|^2\right\rangle_{\mathrm{t}}}_{I_1} + \underbrace{\left\langle |E(\vec{r}_2,t_2)|^2\right\rangle_{\mathrm{t}}}_{I_2} + 2\underbrace{\mathrm{Re}\left\langle E^*(\vec{r}_1,t_1)E(\vec{r}_2,t_2)\right\rangle_{\mathrm{t}}}_{\text{correlation term }\Gamma}. \tag{2.54}$$

The total electric field consists of three terms; the independent intensities of the radiation from two points I_1 and I_2, and the correlation Γ between those points. The first-order correlation function [35]

$$\Gamma(\vec{r}_1,t_1;\vec{r}_2,t_2) = \left\langle E^*(\vec{r}_1,t_1)E(\vec{r}_2,t_2)\right\rangle \tag{2.55}$$

depends on the phase differences and results in an intensity pattern with maxima and minima. The normalized correlation function is

$$\gamma(\vec{r}_1,t_1;\vec{r}_2,t_2) = \frac{\left\langle E^*(\vec{r}_1,t_1)E(\vec{r}_2,t_2)\right\rangle}{\left[\left\langle |E(\vec{r}_1,t_1)|^2\right\rangle \left\langle |E(\vec{r}_2,t_2)|^2\right\rangle\right]^{1/2}} = \frac{\Gamma(\vec{r}_1,t_1;\vec{r}_2,t_2)}{\sqrt{I_1 I_2}}. \tag{2.56}$$

The *coherence function* C is defined as the absolute value of the normalized correlation function [35]

$$C(\vec{r}_1,t_1;\vec{r}_2,t_2) = |\gamma(\vec{r}_1,t_1;\vec{r}_2,t_2)|. \tag{2.57}$$

The light is said to be fully coherent for $C=1$, partially coherent for $0<C<1$ and fully incoherent for $C=0$. The coherence length is the distance at which the coherence function drops to a given fraction of its maximum value ($1/e^2$, $1/e$ or $1/2$). By inserting C into Eq. 2.54, the maximum and minimum intensities in the resulting fringe pattern can be derived to be

$$I_{\max} = I_1 + I_2 + 2C\sqrt{I_1 I_2} \tag{2.58}$$

$$I_{\min} = I_1 + I_2 - 2C\sqrt{I_1 I_2}. \tag{2.59}$$

The visibility of the interference fringes is defined as

$$V = \frac{I_{\max} - I_{\min}}{I_{\max} + I_{\min}}. \tag{2.60}$$

Inserting Eq. 2.58 and Eq. 2.59 into Eq. 2.60, it can be shows that when the light intensities from both slits or arms are equal ($I_1 = I_2$), then the visibility is equal to the coherence ($V = C$). When $I_1 \neq I_2$, the contrast observed in the experiment is reduced with respect to a given degree of coherence of the incident radiation

$$V = 2C\frac{\sqrt{I_1 I_2}}{(I_1 + I_2)}. \tag{2.61}$$

The degree of coherence of a wave packet can be defined as the normalized integral over the coherence function weighted by the intensity $I = \langle E^* E \rangle_t$ [48]

$$D = \frac{\int C(\vec{r}) I(\vec{r}) d^3\vec{r}}{\int I(\vec{r}) d^3\vec{r}} \tag{2.62}$$

with $\vec{r} = (x, y, z(t))$. The properties of the longitudinal and transverse coherence are often studied separately.

2.3.1 Longitudinal coherence

Longitudinal coherence is a measure of the correlation of the phase of a light wave at different points along the propagation direction. It shows how monochromatic the source is, i.e. the temporal coherence can be increased simply by using a band-pass filter, but at the expense of loosing intensity. The temporal correlation function G is derived by averaging Γ (Eq. 2.55) at a given position. By assuming one point r_1 at two times $t_1 = t$ and $t_2 = t + \tau$, the temporal autocorrelation function can be written as a function of the delay τ [34]

$$G(\tau) = \langle E^*(t) E(t+\tau) \rangle = \lim_{T \to \infty} \frac{1}{2T} \int_{-T}^{T} E^*(t) E(t+\tau)\, dt\,, \tag{2.63}$$

and the degree of temporal coherence, i.e. the normalized autocorrelation function, reads

$$g(\tau) = \frac{G(\tau)}{G(0)} = \frac{\langle E^*(t)E(t+\tau)\rangle}{\langle E^*(t)E(t)\rangle}. \tag{2.64}$$

When the light is perfectly monochromatic and deterministic, the coherence function equals 1 for all time delays, but in reality it decreases as τ increases. The time (the delayed path) at which the temporal coherence drops to 1/2 of its maximum value is defined as the *coherence time* τ_c (coherence length l_c). In general, the power-equivalent width of the function $g(\tau)$ can also be defined as τ_c, and it is commonly derived by integrating the coherence function over time [34]

$$\tau_{\mathrm{c}} = \int_{-\infty}^{\infty} |g(\tau)|^2 dt\,, \qquad l_{\mathrm{c}} = c\tau_{\mathrm{c}}. \tag{2.65}$$

In this thesis, the definition in Eq. 2.65 is used to determine the coherence length. According to the *Wiener-Khinchin* theorem, the autocorrelation function $G(\tau)$ and the spectral density $S(\nu)$ form a Fourier transform pair, and therefore their widths are inversely proportional to each other. For a Gaussian pulse [34]

$$\tau_{\mathrm{c}} = \sqrt{\frac{2\ln 2}{\pi}} \cdot \frac{1}{\Delta\nu} = \frac{0.664}{\Delta\nu} \tag{2.66}$$

$$l_{\mathrm{c}} = c\tau_{\mathrm{c}} = 0.66c/\Delta\nu = 0.66\lambda^2/\Delta\lambda, \tag{2.67}$$

while for Lorentzian pulse $\tau_{\mathrm{c}} = 1/\pi\Delta\nu$ [34].

Measurement of temporal coherence with a Michelson interferometer

A Michelson interferometer can be used to determine the temporal coherence of radiation. A simplified sketch of the interferometer is shown in Fig. 2.9. The beam is divided by a beamsplitter into two parts with equal amplitude which are reflected from mirrors M_1 and M_2 and finally return to the beamsplitter. The part of the beam coming from M_1 (M_2) passes through (is deflected by) the beamsplitter towards the detector. United again at the beamsplitter, the beams interfere and constitute concentric, circular fringes on a 2D detector or on a screen. If one of the mirrors is tilted and the beams are not parallel after being united, the fringes appear like straight lines instead of circles. The beamsplitter requires a special coating in order to obtain two beams with equal amplitudes.

Assuming the coating of the beamsplitter is on the backside (with respect to the incident beam), the beam "$E(t)$" or OM_1 passes through the beamsplitter three times, while the other beam passes only once. This will cause different dispersive effects in the two arms, which will affect their interference, as the optical path depends on the wavelength. The effect of dispersion is stronger in the case of ultrashort non-monochromatic pulses. For this reason, a compensator should be placed in the OM_2 beam path. The effect caused by the compensator plate or its material, thickness, and orientation must be exactly the same as that of the beamsplitter.

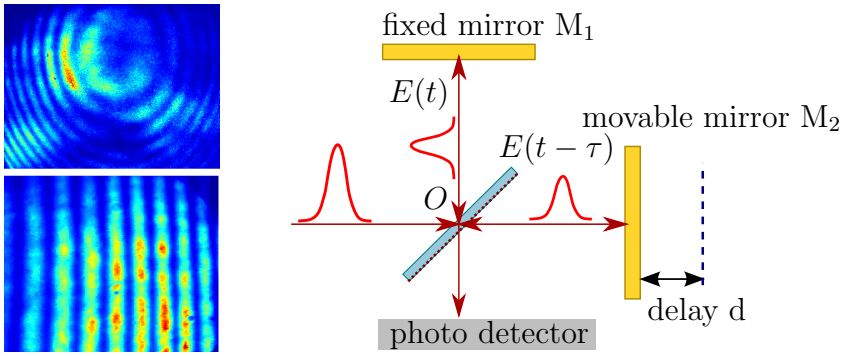

Figure 2.9: Scheme of the Michelson interferometer and the resulting circular (straight) fringes for normal (tilted) mirrors. The interference patterns were obtained by using the CHG light at DELTA (see Section5.6).

The delay d between the beams can be changed by moving the mirror M_2, which is mounted on a linear stage. The intensity of the fringes depends on the phase differences of the two beams, which depend on the difference of their optical paths. If the path difference is an integer (half integer) multiple of the wavelength, constructive (destructive) interference will occur

$$2d\ \cos(\theta_{\mathrm{m}}) = m\lambda\ ;\ \text{constructive interference} \tag{2.68}$$

$$2d\ \cos(\theta_{\mathrm{m}}) = \left(m + \frac{1}{2}\right)\lambda\ ;\ \text{destructive interference,} \tag{2.69}$$

where m is an integer, λ is the wavelength of the light, and θ_{m} is the angular position of the m^{th} fringe from the origin O at the beamsplitter. The transverse position of the m^{th} fringe on the screen at the distance L from the beamsplitter is

$$y_{\mathrm{m}} = L \cdot \tan(\theta_{\mathrm{m}}). \tag{2.70}$$

Assuming the first bright fringe m_0 at $\theta_{m_0} = 0$ and the p^{th} bright fringe at θ_p, then

$$2d = m_0\lambda \tag{2.71}$$

$$2d\ \cos(\theta_p) = (m_0 - p)\lambda. \tag{2.72}$$

By subtracting Eq. 2.71 from Eq. 2.72 and by inserting $\cos(\theta_p) \approx 1 - (\theta_p^2/2)$, the angular position of the p^{th} fringe and the transverse distance Δy between two fringes is

$$\theta_p \approx \left(\frac{p\lambda}{d}\right)^{1/2}, \quad \Delta y = y_{p+1} - y_p \approx L(\theta_{p+1} - \theta_p) = L(\sqrt{p+1} - \sqrt{p})\left(\frac{\lambda}{d}\right)^{1/2}. \tag{2.73}$$

The Michelson interferometer is a field autocorrelator i.e. it does not include second-order nonlinear effects, therefore it does not give any information about the pulse shape or phase, but it provides information about the spectrum, as the coherence length is proportional to the inverse frequency bandwidth (Eq. 2.67). The output intensity of the interferometer is given by the electric field squared using 2.52 and 2.53

$$I(t,\tau) = \frac{1}{2}\epsilon_0 cn\{E_1^2(t) + E_2^2(t+\tau) + E_1(t)E_2^*(t+\tau)e^{i\omega\tau} + E_1(t)E_2^*(t+\tau)e^{-i\omega\tau}\}. \tag{2.74}$$

With slow detectors, the average of the expression above is measured in the ideal case of an infinitely thin beamsplitter and non-dispersive reflectors. If $E_1 = E_2$, the visibility of the fringes is highest. If the light is polychromatic, the visibility is high near the center ($y_0 = 0$) and decreases as y increases.

2.3.2 Transverse coherence

Transverse coherence is a measure of the correlation of the phase of light waves at different points perpendicular to the direction of propagation.
The correlation function between points $\vec{r}_1$ and $\vec{r}_2$ with a time difference $\tau = 0$ for quasi-monochromatic light is defined as [35]

$$J_{12} = \Gamma_{12}(0) = \langle E^*(\vec{r}_1, t)E(\vec{r}_2, t)\rangle\ , \tag{2.75}$$

also called the "mutual transverse coherence function" or the "mutual intensity of the light". The complex coherence function of the light is defined as [35]

$$\mu_{12} = \gamma_{12}(0) = \frac{J_{12}}{[I(\vec{r}_1)I(\vec{r}_2)]^{1/2}}, \quad 0 \leq |\mu_{12}| \leq 1. \tag{2.76}$$

The parameter J_{12} may be regarded as a phasor amplitude of a spatial sinusoidal fringe pattern, whereas μ_{12} is simply a normalized version of J_{12} [35]. The coherence length is the distance at which the transverse coherence drops to half of its maximum value.

Diffraction

Radiation from a light source appears diffracted in the observation plane with an intensity pattern which is characteristic for the source size, angular distribution and the geometry of the involved apertures. According to *Huygens principle*, any point on a wavefront is regarded as a source of a new wavefront called secondary wave, i.e. a spherical wave emerges from each point. The sum of these secondary waves determines the shape of the wave at a subsequent time. The complex amplitude of the primary spherical wave at point Q located at a distance $|\vec{r}_0|$ from the source P_0, is given by $U(r_0) = (U_0/r_0)e^{ikr_0}$. The complex amplitude of the secondary field at a point at distance $|\vec{s}|$ from Q was derived by Fresnel [41]

$$U(P) = -\frac{i}{\lambda}U(r_0)\int_S \frac{e^{iks}}{s}K(\chi)\,dS \quad \text{with} \quad K(\chi) = \frac{1}{2}(1+\cos\chi), \tag{2.77}$$

where S describes the surface of the sphere, and K is the inclination factor, which is a function of χ, the angle between $\vec{r}_0$ and $\vec{s}$, and it is maximum in forward direction (at $\chi = 0$). The rapid oscillations of the phase as a function of the position on the screen gives rise to the diffraction pattern. Two types of diffraction occur depending on the distance from the source: far-field or Fraunhofer diffraction and near-field or Fresnel diffraction, distinguished by the far-field condition [42]

$$L \gg \frac{\pi w^2}{\lambda} \tag{2.78}$$

with w being the width of the aperture. In the far field, the total intensity diffracted by an aperture can be derived by the Fraunhofer integral which is the two-dimensional Fourier transform of the aperture. For a circular aperture, the intensity of the diffracted radiation in

the image plane is given by

$$I(y) = I_0 \frac{4{J_1}^2(kw\ \sin\theta)}{(kw\ \sin\theta)^2}. \tag{2.79}$$

The position on the screen is denoted by y, $k = 2\pi/\lambda$ is the wave number of the radiation, $\theta = \tan^{-1}(y/L)$ is the angle between the light ray and the optical axis, and J_1 is the first-order Bessel function of the first kind. Here, the incident wave is assumed to be a plane wave, that is $E(y) = E_0 = const.$ Due to diffraction, the radiation intensity in the image plane is distributed over a central circle, known as "Airy's disc", and concentric rings with the first minimum at $\sin\theta = 1.22\lambda/w$.
A single slit of width w and infinite length forms a diffraction pattern in a direction y perpendicular to the slit (Fig. 2.10) with an intensity distribution given by

$$I_D(y) = \left(\frac{\sin(\pi wy/\ (\lambda L))}{\pi wy/\ (\lambda L)}\right)^2 \tag{2.80}$$

with the first minimum given by $\sin\theta = \lambda/w$.

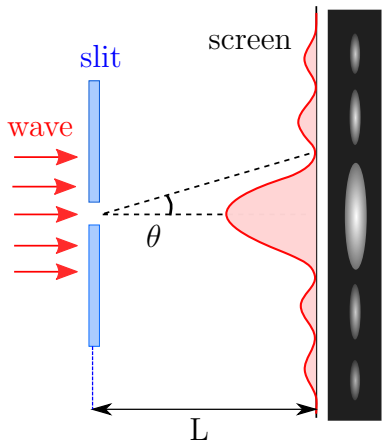

Figure 2.10: Scheme of the Fraunhofer diffraction and the intensity distribution on y axis.

Effect of beam propagation on transverse coherence

The character of the mutual intensity function produced by an incoherent source is fully described by the *Van Cittert–Zernike* theorem, which addresses the propagation of the mutual intensity function of a quasi-monochromatic light. It states that "the mutual intensity in the observation plane $J(x_1, x_2; x_2, y_2)$ can be found by a two-dimensional Fourier transformation of the intensity distribution across the source" [35].

The coherence area A_c on the observation (x,y) plane is defined by [35]

$$A_c = \iint_{-\infty}^{+\infty} |\mu(\Delta x, \Delta y)|^2 d\Delta x d\Delta y, \tag{2.81}$$

where Δx and Δy are the coordinates differences in the observation plane or the pinhole spacing. For a uniformly bright incoherent source with an area of A_s and with any shape, the coherence area at distance z from the source reads [35]

$$A_c = \frac{(\lambda z)^2}{A_s} \approx \frac{\lambda^2}{\Omega_s}, \tag{2.82}$$

where Ω_s is the solid angle subtended by the source from the origin of the observation region. Relation 2.82 implies that the wavefront from an incoherent source will appear coherent at large distances from the source, hence it must be specified at which position the coherence length has been determined. The reason of this effect can be explained qualitatively as follows. Fluctuations of the light at different points in the plane of an incoherent source are uncorrelated, but when the light propagates in the free space, the radiation from each point diverges and overlaps with the radiation from the neighboring points, making a common contribution. The light reaching two points on the observation plane might emanate from such common contributions, therefore a partial correlation between fluctuations at these points on the image plane can be created, resulting in transverse coherence. On the other side, the longitudinal coherence length is not generally influenced by the propagation in vacuum.

Using the Van Cittert–Zernike theorem, the transverse coherence length l_c of a circular incoherent source with radius r_s and angular extension $\theta_s \approx r_s/z$ is given by [35]

$$l_c \propto 1.22\frac{\lambda}{\theta_s} \propto 1.22\frac{\lambda z}{r_s}. \tag{2.83}$$

In principle, the transverse coherence of a of light from an extended source can be increased by decreasing the source size using a pinhole or by increasing the distance, but only at the expense of intensity. In the extreme limit that light originates from a point source, the coherence length is infinite and the field has full transverse coherence.

Transverse coherence and the beam-quality factor

Transverse coherence depends on the number of the TEM modes in the wave. Many lasers

emit beams that approximate a Gaussian profile with the laser operating on the fundamental transverse mode TEM_{00}, but in general beams are not perfectly Gaussian. The general form of the TEM modes are the Hermite–Gaussian (H-G) modes (TEM_{nm}), which are the solutions of the Maxwell's equations in a laser cavity [46].
The quality of the beam is determined by the M^2 factor, also called beam quality factor, and defined as the beam parameter product (BPP) divided by λ/π. BPP is the product of the beam waist and the beam divergence (half opening angle in the far field). The smallest possible beam parameter product is λ/π, achieved with a "diffraction-limited Gaussian beam" with $M^2 = 1$, which corresponds to full transverse coherence. The H-G modes have an M^2 factor of $(2n + 1)$ in x direction and $(2m + 1)$ in y direction [46].
The divergence of a multimode laser beam in the far field ($z \gg (\pi {w_0}^2)/\lambda$) is $\theta_{\mathrm{div}} = M^2\lambda/\pi w_0$, which is M^2 times that of a Gaussian beam of the same spot size. By comparing this divergence with Eq. 2.83, one can establish a relation between the M^2 factor, the laser waist and the radius of the coherence area r_c. The higher the number of TEM modes, the larger the M^2 and the lower the transverse coherence length.

Measurement of transverse coherence with a double-slit setup

Double-slit experiments can be used to determine the transverse coherence degree of a radiation field. The principle of the double-slit experiment is schematically shown in Fig. 2.11. The wavefront of the radiation is divided into two equal parts by using two slits with equal width w and separation d. The beams will interfere on the screen resulting in a pattern of dark or bright fringes depending on the phase difference of the beams, which arises from the path difference $\delta l = d \sin\theta$ with θ being the angular position on the screen. If the optical path difference is an integer (a half-integer) of the wavelength, the interference will be constructive (destructive).

Assuming θ is small and $\sin\theta_m \approx \tan\theta_m$, the constructive condition for the m^{th} fringe, its position y_m on the screen and the distance Δy between two successive bright fringes reads

$$d \sin\theta_m = m\lambda\,, \qquad y_m = L \tan\theta_m \approx L\frac{m\lambda}{d}\,, \qquad \Delta y \approx L\frac{\lambda}{d}. \tag{2.84}$$

In the far field, the two slits form identical diffraction patterns $I_1(y) = I_2(y)$, given by Eq. 2.80. In the near field, the single-slit diffraction patterns of the two slits are displaced by the slit separation. The electric field amplitudes of the two beams coming from the slits, E_1 and E_2, and the intensities in the near field are

$$I_1(y) = {E_1}^2(y) \;\;,\;\; E_1(y) = \frac{\sin(u)}{u} \;\;,\;\; u = \frac{\pi w(y + \frac{d}{2})}{\lambda L},$$

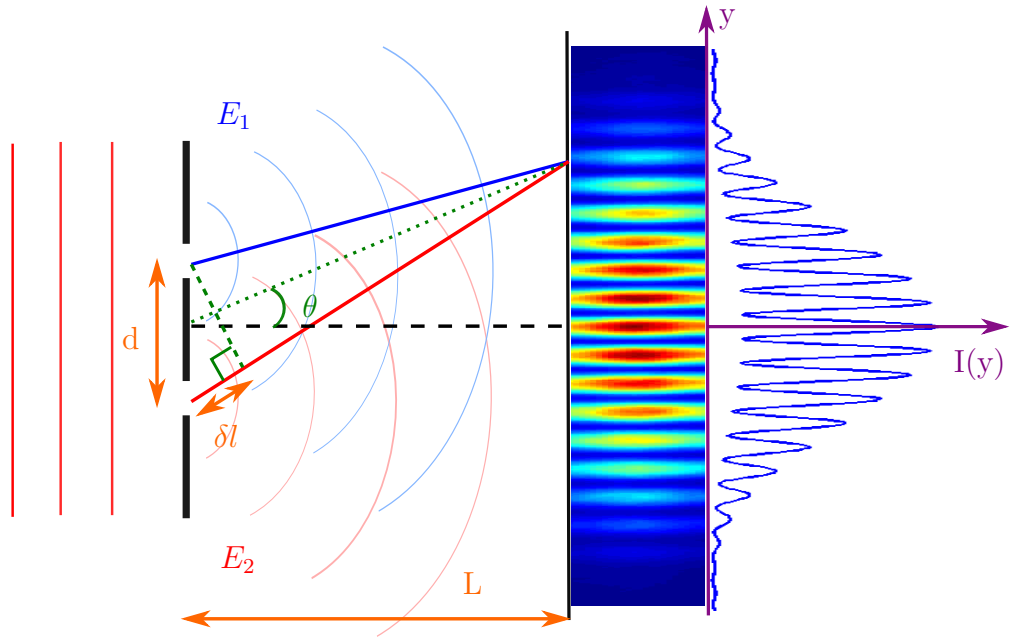

Figure 2.11: Scheme of the double slit experiment (left), resulting fringe pattern and its projection on y axis (right). The interference pattern shown here is obtained by using the CHG light at DELTA (see Section 5.6).

$$I_2(y) = {E_2}^2(y) \quad , \quad E_2(y) = \frac{\sin(v)}{v} \quad , \quad v = \frac{\pi w(y - \frac{d}{2})}{\lambda L}. \tag{2.85}$$

The sum $S(y)$ and the extrema of the intensities are

$$S(y) = I_1(y) + I_2(y), \tag{2.86}$$

$$I_{\max}(y) = (E_1(y) + E_2(y))^2 \quad , \quad I_{\min}(y) = (E_1(y) - E_2(y))^2. \tag{2.87}$$

The visibility $V(y) = C(y)$ (for equal intensity on the slits) was defined in Eq. 2.60. The total intensity on the y axis for the near field and far field can be written as

$$I(y) = S(y)\left[1 + V(y)\cos\left(\frac{2\pi d}{L\lambda}y\right)\right], \qquad \text{in near field,} \tag{2.88}$$

$$I(y) = I_{\mathrm{D}}\left[1 + V(y)\cos\left(\frac{2\pi d}{L\lambda}y\right)\right], \qquad \text{in far field} \tag{2.89}$$

with I_{D} given by Eq. 2.80. For the near-field case, a modulation is applied to $S(y)$, and for the far field this modulation is applied to the Eq. 2.80. By using the relations above for fitting the interference pattern, the visibility and hence the coherence degree can be determined. If

the spacing between the two slits is larger than the transverse coherence length, the resulting pattern on the screen would look like two single slit diffraction patterns.
Interference of an arbitrary aperture can be simulated by using the algorithms based on wavefront propagation in programs such as GLAD (general laser analysis and design), which solves the Maxwell's equations numerically for propagating wavefronts [47, 48].

2.3.3 Coherence of synchrotron radiation

The temporal coherence of synchrotron radiation is determined by the electron bunch length. If electrons are located within a short bunch of the order of the wavelength, the radiation is temporally coherent, whereas transverse coherence occurs when the transverse beam size is small compared to the radiation wavelength [29].

Temporal coherence

In order to discuss the temporal coherence of synchrotron radiation from an electron bunch in a storage ring, we assume that the radiation field from the j^{th} electron in the bunch is $E_j \propto e^{i(\omega t+\varphi_j)}$ with frequency ω and phase φ_j. The phase of the light from each electron depends on the electron position inside the bunch ($\varphi_j = 2\pi z_j/\lambda$, with z_j being the distance of the electron from the center of the bunch) [29]. The total radiation field is the sum of the radiation from all electrons, and the total intensity is proportional to the total electric field squared (see Eqs. 2.2 and 2.23)

$$|\vec{E}_{\text{tot}}| = \sum_{j=1}^{N_{\text{e}}} E_j \propto \sum_{j=1}^{N_{\text{e}}} e^{i(\omega t+\phi_j)} \tag{2.90}$$

$$I_{\text{tot}} = \sum_{j,l=1}^{N_{\text{e}}} E_j E_1^* = I_0 \sum_{j,l=1}^{N_{\text{e}}} e^{i(\omega t+\varphi_j)} e^{-i(\omega t+\varphi_1)} = I_0 \sum_{j,l=1}^{N_{\text{e}}} e^{-i(\varphi_j-\varphi_1)} = N_{\text{e}} I_0 + I_0 \sum_{j,l=1(j\neq l)}^{N_{\text{e}}} e^{-i(\varphi_j-\varphi_1)} \tag{2.91}$$

with I_0 being the single-electron intensity. When the radiation from all electrons has a certain phase relation and is not just statistically distributed ($\Delta\varphi$ =const), the radiation fields are superimposed constructively, the total field (Eq. 2.90) is proportional to the number of electrons N_{e}, and the total intensity is proportional to N_{e}^2. The first term on the right-hand side of the Eq. 2.91 represents the incoherent spontaneous radiation, the second term depends

on the density distribution $\rho_e(s)$. Using Eq. 2.91, the total radiation power can be written as [29]

$$P(\lambda) = P_e(\lambda)N_e[1 + (N_e - 1)g^2(\lambda)] \tag{2.92}$$

with P_e being the single-electron radiation power and $g(\lambda)$ the so-called form factor, which is the Fourier transform of the longitudinal distribution of the normalized electron density

$$g(\lambda, l) = \frac{1}{N_e}\int_{-\infty}^{\infty} \rho_e(s)\, e^{-i\,2\pi s/\lambda} ds \tag{2.93}$$

and determines the amount of the coherent contribution to the intensity. Assuming an rms bunch length of σ_l for a Gaussian bunch, the form factor becomes [29]

$$g^2(\lambda) = \exp\left(-\pi\frac{l^2}{\lambda^2}\right) \quad \text{with} \quad l = \sqrt{2\pi\sigma_l}\,. \tag{2.94}$$

The expression shows that the coherent radiation power (the second term on the r.h.s. of Eq 2.92) falls off rapidly for wavelengths shorter than the effective bunch length l. For longer wavelengths, there are coherent contributions to the radiation, but for typical bunch lengths such long wavelengths are damped and can not propagate along the vacuum chamber of a storage ring, depending on the size of the vacuum pipe compared to the bunch length [29].

When an electron bunch is composed of periodic substructures, the more frequent and sharper these substructures, the larger the Fourier transform components and therefore the higher the coherent contribution in power. In single-pass laser-seeded schemes, the substructures are created by laser-induced energy modulation and subsequent density modulation, which gives rise to higher temporal coherence than that of the spontaneous radiation.

Transverse coherence

Since synchrotron radiation is emitted from a small area equal to the cross section of the electron beam, it may have high transverse coherence, depending on the wavelength and the distance between the source point and the observer. By reducing the electron beam emittance, the emittance of the photon beam can be reduced down to the diffraction limit, which is $\sigma_r\sigma_{r'} = \lambda/(4\pi)$ with $\sigma_r = \sqrt{\lambda L}/(2\pi)$, $\sigma_{r'} = \sqrt{\lambda/L}$ being the diffraction-limited source size, and L the length of the photon source along the particle path [29]. To produce spatially coherent or diffraction-limited radiation, the electron beam emittance must be smaller than

the diffraction-limited photon emittance [29]

$$\epsilon_{\mathrm{x,y}} \leq \frac{\lambda}{4\pi}. \tag{2.95}$$

This condition can be achieved easier for long wavelengths; the longer the wavelength the longer the transverse coherence length (see also Eq.2.83).

As a result of the stochastic nature of spontaneous emission, the spontaneous undulator radiation is composed of many transverse modes with random magnitude and phase, i.e. with poor transverse coherence. In an FEL, however, the central mode TEM_{00} (with Gaussian shape) will develop more strongly in the undulator and dominate due to the best overlap with the electron bunch. Therefore, the transverse coherence increases until saturation. After saturation of the TEM_{00} mode, other modes gain importance and the coherence degree decreases [48]. In a single-pass seeded scheme, the TEM_{00} mode will dominate and develop even quicker due to its dominant contribution in the seed laser beam.

Applications of coherent radiation

Coherent radiation is important for performing experiments like imaging, diffraction, interferometry and holography. Coherent ultrafast pulses are used to study bioparticles and macromolecules which are sensitive to radiation damage, providing insights into disease and drug design [49].

2.4 Coherent Harmonic Generation (CHG)

In many experiments such as time-resolved photoelectron spectroscopy, both femtosecond pulse duration and high photon energy (in VUV or X-ray regime) are required. However, commercial femtosecond lasers can not deliver pulses at high photon energies in the VUV or X-ray regime, whereas generating ultrashort synchrotron pulses (in the femtosecond range) by means of storage rings is limited, since the bunches are too long (in picosecond range).

Several laser seeding schemes have been developed to employ the advantages of the laser- and synchrotron-light sources to generate ultrashort pulses with high photon energies in storage rings. These schemes generally comprise at least two undulators separated by a dispersive section. The basis of any seeding technique is a periodic modulation of the electron energy induced by the electric field of a seed laser pulse that co-propagates with the electron bunch through an undulator called ”modulator”. In the following, several schemes

are described shortly, and the principles of coherent harmonic generation is explained in more details.

In *femtosecond slicing*, proposed by A. Zholents and M. Zolotorev [50], the off-energy electrons caused by the laser-induced energy modulation in a femtosecond slice of the bunch are transversely displaced. Incoherent spontaneous synchrotron radiation is generated by these electrons and is extracted geometrically by spatial or angular discrimination. The intensity of these pulses is only 10^{-4} of normal undulator light and the repetition rate is limited to that of the laser, but the radiator can be set to any desired wavelength and polarization. This scheme was first demonstrated at the ALS (Berkeley, California, USA) [51] with a dipole magnet as radiator, and later at BESSY (Berlin, Germany) [52] and the SLS (Villigen, Switzerland) [53] producing femtosecond undulator radiation.

In *coherent harmonic generation* (CHG), the process is followed by a subsequent density modulation or "microbunching", in a chicane, resulting in density maxima separated by one laser wavelength. Finally, the electrons radiate in a second undulator called "radiator". The radiation does not need to be geometrically separated from the spontaneous emission, since the intensity of the coherent radiation is about 1-3 orders of magnitudes higher than the incoherent radiation. However, since the repetition rate of CHG radiation (limited by the repetition rate of the laser) is about 3 orders of magnitude lower than the electron bunch revolution rate, time-resolved gating is needed to select only the coherent pulse from the sequence of the spontaneous-emission pulses. CHG is limited in wavelength to approximately the 10^{th} harmonic of the seed wavelength. The principle of CHG was first proposed in 1982 by R. Coïsson and F. De Martini with an analytic model describing the CHG process in an optical klystron [10]. The first demonstration of CHG was performed in 1984 at the ACO [11, 12] storage ring (Orsay, France), and then at Super-ACO in the VUV range [13]. More recent experiments have been conducted at UVSOR-II in Okazaki, Japan [14, 15], ELETTRA (Trieste, Italy) [16–18], and DELTA (Dortmund, Germany) [19–28]. The CHG principle and the corresponding phase space distributions are sketched in Fig. 2.12.

High-gain harmonic generation (HGHG) is similar to CHG, with the difference that it is applied to linac-based FELs in which long undulators, the low emittance of the electron beam, and high peak current enables a very high brightness. It was demonstrated at BNL (Upton, New York, USA) [6], and is now routinely employed at FERMI@Elettra (Trieste, Italy) [7].

Echo-enabled harmonic generation (EEHG) is a new FEL seeding method to reach much higher harmonic numbers (around 40). It was proposed in 2009 by G. Stupakov [54]. Three undulators and two chicanes are employed in this scheme. The energy modulation in the first undulator is followed by a strong chicane in order to produce a pattern of discrete

energy bands. After a second energy modulation, this pattern is converted to a density modulation. The previously created discrete energies give rise to a periodic substructure of the density maxima which contains Fourier components at much smaller wavelengths. Proof-of-principle experiments at moderate wavelengths above 100 nm have been carried out at SLAC (California, USA) [55–58] and SINAP (Shanghai/China) [59].

2.4.1 Principle of CHG

The principle of CHG is depicted in Fig. 2.12. After passing through the magnetic chicane, the longitudinal distribution of the energy-modulated electrons is modified. The magnitude of the longitudinal displacement (Δz) of electrons depends on their energy modulation ($\Delta E/E$) and on the strength of the chicane (the r_{56} value) given by Eq. 2.19.

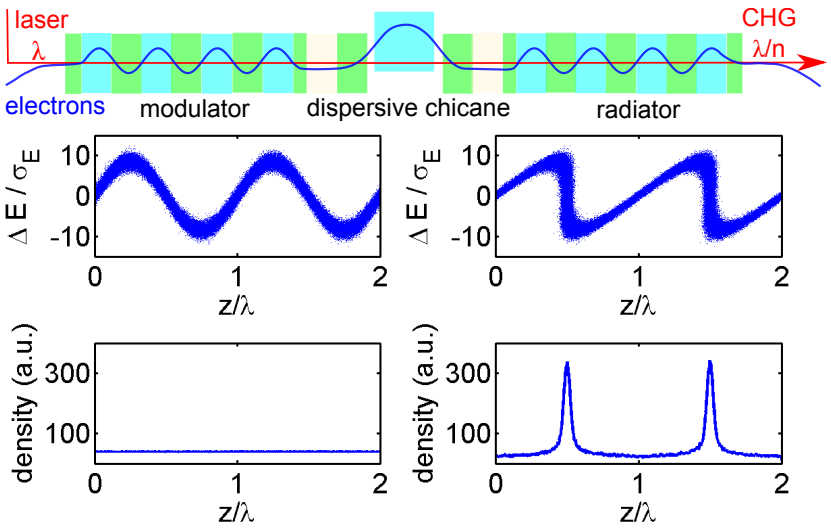

Figure 2.12: Principle of CHG; a femtosecond laser pulse interacts with an electron bunch in an undulator causing a periodic energy modulation and subsequent microbunching which gives rise to coherent radiation at harmonics of the seed wavelength.

The electrons form a fine structure (microbunches) with a spacing of one laser wavelength, which is the reason for the coherent radiation at harmonics of the laser wavelength. Since the phases of radiation from the electrons in the microbunches are correlated, the radiation fields add up constructively and therefore the total radiation intensity is proportional to the squared number of electrons (see Eq. 2.92).

2.4.2 Electron-laser interaction

The interaction between the electrons and the optical radiation field in an undulator can be studied by solving the coupled pendulum-Maxwell equations [60], which relate the evolution

of the longitudinal phase of the electron and the radiation amplitude. This model can also be generalized to account for the evolution of the optical field at harmonics of the fundamental wavelength [61], and is applicable for the numerical simulation of the CHG [15]. In this Section, however, only the analytical models for CHG are discussed.

In the analytical model developed in [10], the relativistic motion of the electrons under the influence of both the magnetic field of the undulator and the electric field of a laser pulse (here considered as a plane wave) obeys the Lorentz force. The energy transfer between the electron with a transverse velocity of $(v_x, v_y = 0, v_z)$ and a laser field with horizontal polarization ($\vec{E} = \vec{E}_x$) can be written as

$$\frac{dE}{dt} = \vec{F}\vec{v} = -eE_x v_x \quad \text{with} \quad \vec{F} = -e(\vec{E} + \vec{v} \times \vec{B}). \tag{2.96}$$

The relative energy modulation is proportional to the peak electric field of the laser pulse E_L and is given by [62]

$$\frac{\Delta E}{E} = \frac{eKE_\mathrm{L}N_\mathrm{u}\lambda_\mathrm{u}}{2E^2 m_\mathrm{e}c^2}[J_0(\xi) - J_1(\xi)] \ \sin\varphi_0$$

$$\text{with} \ \ \xi = \frac{K^2}{4(1 + K^2/2)}, \tag{2.97}$$

where K is the undulator parameter, φ_0 and E are the initial values for the longitudinal phase and the energy of the electron, respectively, and are assumed to be constant in the modulator. Along the dispersive section, the induced energy modulation results in a phase shift of the electrons which depends on the number of the undulator periods N_u and number of the undulator-period equivalent of the dispersive section N_d, and is equal to $\delta\alpha = 4\pi(N_\mathrm{u} + N_\mathrm{d})$. Electrons are longitudinally displaced and form microbucnches.

The quality of the microbunching is determined by a coefficient called "bunching factor" b_n, which is the discrete Fourier transform of the longitudinal distribution of the electron density. The bunching factor is the form factor for certain frequencies at the harmonics of the laser wavelength (see Section 2.3.3 and Eq. 2.93). It depends on the energy modulation amplitude $\Delta E/E$, the harmonic number n, and the relative energy spread of electrons σ_E. It is given by [15]

$$b_\mathrm{n} = f_n J_n[4\pi n(N_\mathrm{u} + N_\mathrm{d})(\Delta E/E)] = f_n J_n(n\,\delta\alpha)$$

$$\text{with } f_n = \exp\left(-8\left[\pi n \sigma_E (N_\mathrm{u} + N_\mathrm{d})\right]^2\right); \quad N_\mathrm{d} = r_{56}/2\lambda, \tag{2.98}$$

where J_n is the first-kind Bessel function of the order n. Examples for an energy modulation $\Delta E/E$ of 0.6% and 0.4% with optimum r_{56} and with a seed wavelength of 400 nm are shown in Fig. 2.13. These values are calculated using the Fourier transform of the electron distribution as shown in Fig. 2.12. The exponential decrease with harmonic number n is dominant, and the second maximum of the Bessel function can also be seen.

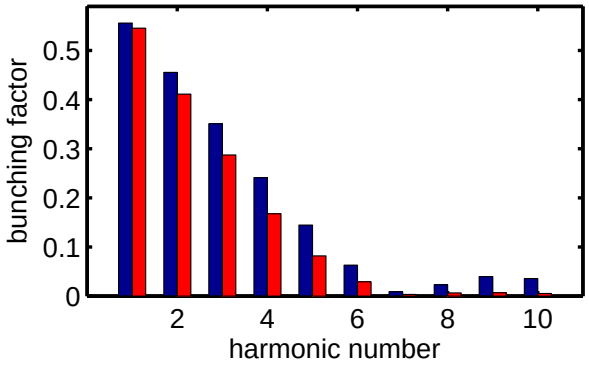

Figure 2.13: The bunching factor for two relative energy modulation values of $\Delta E/E = 0.6\%$ (blue) and 0.4% (red), relative energy spread of the electrons $\sigma_\mathrm{E} = 7 \times 10^{-4}$, and seed wavelength of 400 nm.

Assuming a laser pulse duration τ_L and electron bunch length τ_e, the intensity of the CHG radiation, which is proportional to the squared number of electrons N_e, reads

$$I_\mathrm{CHG} = {b_\mathrm{n}}^2 \left(\frac{\tau_\mathrm{L}}{\tau_\mathrm{e}}\right)^2 {N_\mathrm{e}}^2 I_e. \tag{2.99}$$

To achieve the optimum CHG intensity, the following approximate relation must hold between r_{56} and the energy modulation

$$\Delta z = r_{56}\frac{\Delta E}{E} \approx \frac{\lambda_\mathrm{L}}{4}, \tag{2.100}$$

which implies the creation of the microbunches radiating coherently (see also Section 2.3.3 for temporal coherence of synchrotron radiation); the Δz is the longitudinal displacement of electrons.

The total energy deviation, given by the sum of ΔE and several σ_E (initial energy spread of the electron bunch), must stay below the energy acceptance of the storage ring in order not to loose the beam; therefore the energy modulation is limited by the energy acceptance and

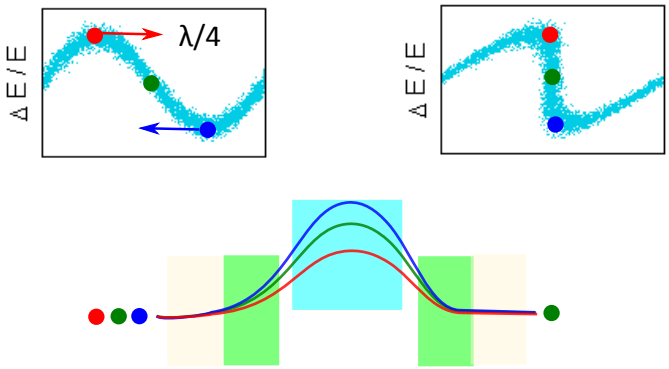

Figure 2.14: Longitudinal displacement (by $\lambda/4$) of the energy-modulated electrons passing through the chicane resulting in formation of microbunches.

alternatively by the laser pulse energy. To obtain the necessary longitudinal displacement (given by Eq. 2.100), r_{56} must be increased and adjusted to the required optimum value.

Coherent THz radiation

When the energy-modulated electrons pass through the following dipole magnets of the storage ring, they are longitudinally displaced and leave a sub-millimeter gap in the longitudinal density profile. Figure 2.15(a) shows a simulation of the energy modulation and resulting displacement, Fig. 2.15(b) shows its Fourier transformation [80].

At high frequencies (the blue curve), the radiation is incoherent, since the wavelengths are shorter than the bunch length (about 100 ps FWHM at the DELTA storage ring). For photon wavelengths longer than the bunch length (orange curve), the radiation is coherent but is greatly damped and do not propagate along the vacuum pipe. In the THz region, there is a coherent contribution due to the laser-induced gap in the longitudinal electron distribution (red curve).

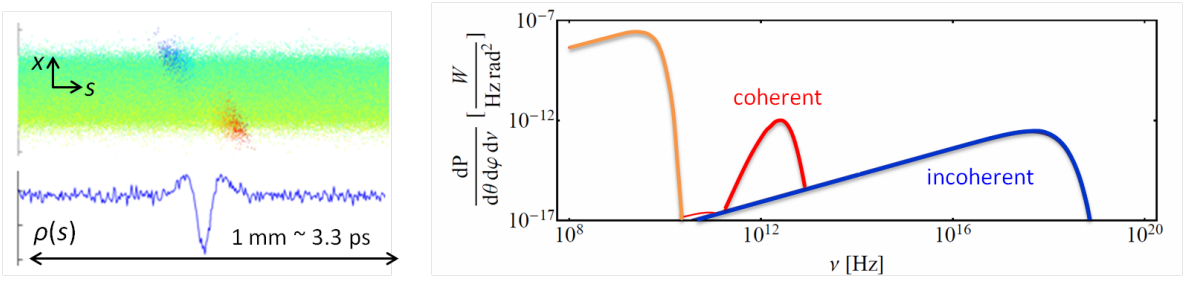

(a) (b)

Figure 2.15: a) Longitudinal density profile of the energy-modulated electrons after passing through a dipole magnet, derived by particle tracking simulation (for CHG at DELTA) with $\Delta E/E = 0.5\%$ [80] (bottom); electrons with negative/positive energy deviation are marked red/blue (top). b) Spectrum derived by Fourier transformation of the density distribution of the whole electron bunch [80].

2.4.3 Experiments with CHG pulses

Since CHG pulses are ultrashort and synchronized with the laser pulses, they can be used in pump-probe experiments for time-resolved studies in the ps and fs domain such as ultrafast photochemical reactions, solvent-solute structural dynamics, structural dynamics in biological systems, order-disorder phenomena in condensed matter, magnetisation dynamics in micro- and nano-magnetism, dynamics of phonons in semiconductors, excitons in metals, and spin dynamics in ferromagnets [65]. Furthermore, CHG pulses are well-suited for experiments requiring a high degree of temporal or transverse coherence. The basics of photoelectron spectroscopy (PES) and the pump-probe technique are shortly described in the following.

Photoelectron spectroscopy

Photoelectron spectroscopy (PES) is a method to study the composition and electronic state of the surface region of a sample by analyzing the kinetic energy distribution of the emitted photoelectrons. It is based on the photoelectric effect (PE) introduced for the first time by Einstein [66]. The fundamental photoelectric equation

$$E_{\mathrm{kin}} = h\nu - E_{\mathrm{bin}} - \phi_0 \tag{2.101}$$

is the basis for the interpretation of PE experiments. Here, E_{kin} is the kinetic energy of the electron, E_{bin} the binding energy, and ϕ_0 a characteristic constant of the sample surface known as the work function, which is the energy needed for taking an electron from the Fermi level to the vacuum level. The fundamental principle of the photoemission process is schematically shown in Fig. 2.16 for the valence band and core levels of a metal. Electrons with binding energy E_{bin} can be excited above the vacuum level E_{vac} by photons with energy $h\nu \geq E_{\mathrm{bin}} + \phi_0$. The photoelectron distribution $I(E_{\mathrm{kin}})$ can be measured by an energy analyzer and is to first order an image of the density of occupied electronic states $N(E)$ in the sample.

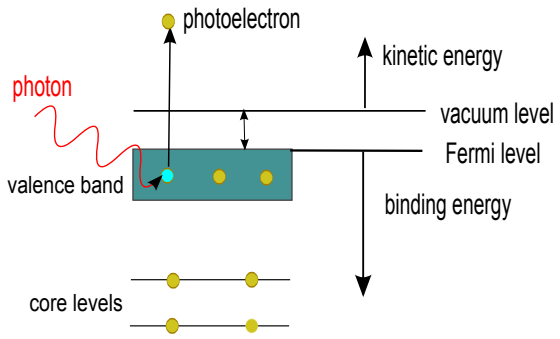

Figure 2.16: Schematic view of the photoemission process.

Ultraviolet photoelectron spectroscopy (UPS) is mainly used for angle-resolved investigation of valence band states (ARUPS), X-ray photoelectron spectroscopy (XPS) is used to investigate core-level states at higher binding energies. The theoretical description of the photoelectron spectrum is based on *Fermi's golden rule* [67]. An example photoelectron spectrum using synchrotron radiation with a fundamental photon energy of $h\nu = 9$ eV and its second harmonic (18 eV) is schematically depicted in Fig. 2.17, showing the valence band near the Fermi level ($E_{\mathrm{bin}} = 0$). The background intensity, increasing with the binding energy, is due to secondary electrons. These secondary electrons are generated when the energetic photoelectrons are inelastically scattered and excite or ionize other atoms. This leads to a smooth background at the low-E_{kin} (high-E_{bin}) side of the principal photoemission peak. The photoelectron distribution from both photon energies overlap with each other and form a more complex spectrum.

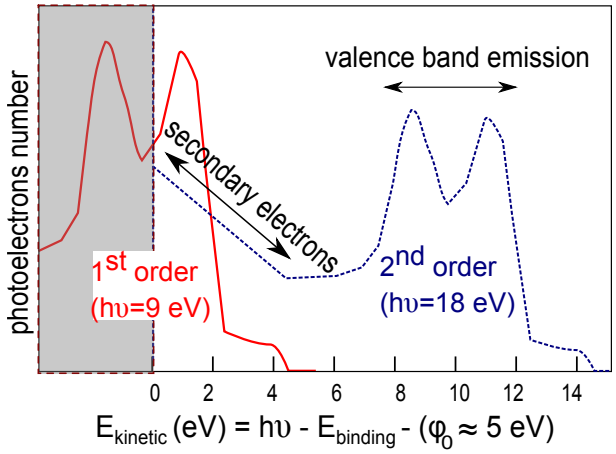

Figure 2.17: A schematic view of a photoelectron spectrum using synchrotron radiation with a fundamental photon energy of $h\nu = 9$ eV (red curve) and its second harmonic at 18 eV (blue curve), showing the valence band near the Fermi level and secondary electrons. The photoelectron distribution from both photon energies overlap with each other.

Synchrotron radiation is widely used for the excitation of photoelectrons because it allows measurements that cannot be performed with other VUV or X-ray sources in the laboratory [67]. The main advantage compared to laboratory sources is that the required photon energy can be selected from a continuous spectrum over a wide energy range. In addition, synchrotron light sources feature high intensity and brightness, variable polarization, and small photon spots.

Pump-probe experiments

The temporal resolution of time-resolved measurements is limited by the speed of the detectors. Among the fastest detectors are streak cameras with a resolution down to 1 ps. For achieving better time resolution, one of the best options by now is a method called "pump-

probe" used to study and visualize structural dynamic processes in materials. In a typical pump-probe experiment, a pulse called "pump" pulse excite an atom to a certain state, and after a defined delay, a second pulse called "probe" pulse captures a snapshot of the subsequent process (e.g by measuring the transmission, reflection or number of photoelectrons).

The time delay between the two pulses is controlled with an optical delay line. By varying the time delay and monitoring the probe signal, successive snapshots or a "movie" of the process can be made. The temporal resolution is not limited by the time constants of the detector, but by the duration of the pump and probe pulse and the accuracy of the delay.

An alternating switching between pump-probe and probe alone (i.e. without excitation) makes the measurement technique more robust against systematic uncertainties introduced e.g. by intensity variations of the probe pulse. For this purpose, an optical chopper can be used. The general setup of a pump-probe experiment using an ultrashort-pulse source in a storage ring based on laser seeding is schematically shown in Fig. 2.18.

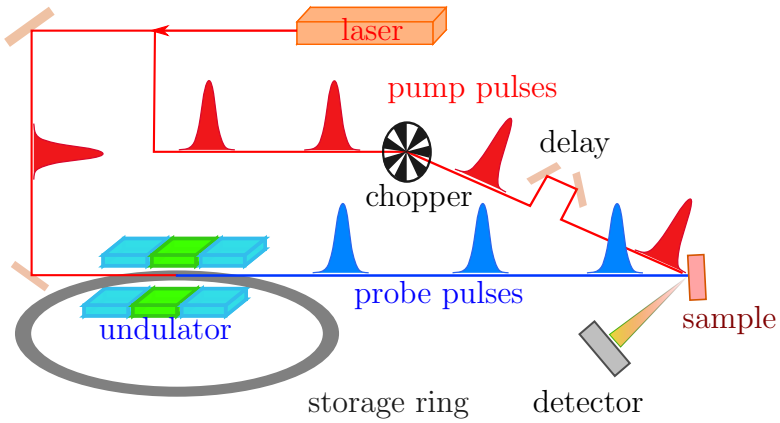

Figure 2.18: The scheme of pump-probe experiments using an ultrashort-pulse source in a storage ring based on laser seeding.

As an example, a laser-pump and X-ray-probe experiment was performed at the femtoslicing source of the BESSY-II electron storage ring [52]. In this experiment [68], the time evolution of the magnetization of the Ni layer in an Au/Ni-layered structure was determined. The 30 nm Au capping layer was excited by the incident laser pump pulse, and subsequently the X-ray magnetic circular dichroism technique was used to probe the femtosecond-scale demagnetization of the adjacent 15 nm Ni layer.

3 Ultrashort Radiation Pulses at DELTA

In this Chapter, at first a short description of the layout and parameters of the DELTA storage ring is presented. As the VUV beamline (BL 5) is used both for diagnostics and pump-probe experiments, this beamline is explained in detail. Then, the CHG facility including the involved beamlines, diagnostics tools and methods is described. At the end, the design and construction of a laser-pulse beamline for future pump-probe experiments is described.

3.1 The synchrotron light source DELTA

DELTA (Dortmund ELecTron Accelerator) is a 1.5-GeV synchrotron radiation source operated by the Center for Synchrotron Radiation at the TU Dortmund University in Germany since 1996 [69]. The layout of the facility is shown in Fig. 3.1.
Electron pulses are emitted from a triode thermionic gun. Electron pulses with a duration of 1 ns for a single bunch or 100 ns for multiple bunches and an energy of 90 keV.

In a linear accelerator (linac), electrons are accelerated to an energy of about 80 MeV by 3-GHz RF pulses driven by a 50 MW pulsed klystron. Next, the electrons are injected into a booster synchrotron (BoDo) with a circumference of 50.4 m. BoDo comprises a FODO lattice, kicker magnets, and a 500-MHz DESY-type resonator which ramps the energy of the

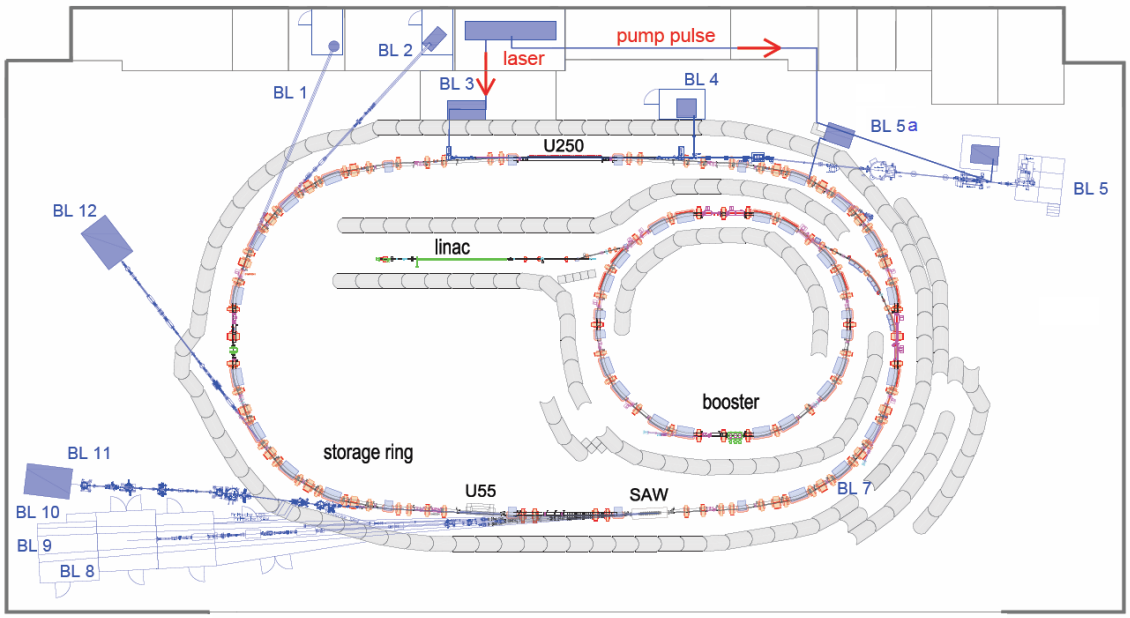

Figure 3.1: Layout of the DELTA storage ring, showing the linear accelerator (linac), the booster (BODO), the storage ring with insertion devices including an electromagnetic undulator (U250), a superconducting asymmetric wiggler (SAW), and a permanent-magnet undulator(U55). Synchrotron radiation beamlines are marked with BL 0 to BL 12.

electrons up to 1.5 GeV within $\sim$ 4 seconds. At this energy, the electrons are injected into the storage ring DELTA by a transfer channel. The multibunch beam is stored for about 10 hours with a maximum beam current of 130 mA decaying to about 50 mA, and the single-bunch beam is stored for 1 hour with a maximum beam current of 10-25 mA decaying to about 5 mA. The electron orbit in DELTA is controlled and corrected by 54 beam position monitors and 56 steering magnets. The energy loss due to the synchrotron radiation is compensated by means of a 500-MHz DORIS-type cavity. Beam instabilities can be damped by using fast bunch-by-bunch transverse and longitudinal feedback systems [71]. The main parameters of the storage ring and the optical parameters at the U250 position are summarized in table 1.

Table 1: Specifications of the storage ring DELTA [70] and optical functions at U250

parameter	symbol	value	unit
general parameters			
electron energy	E	1.49	GeV
circumference	L	115.2	m
revolution time	T_{r}	384	ns
max. beam current (multi-/single-bunch)	I	130 / 20	mA
harmonics number	h	192	-
accelerating RF frequency	f_{RF}	449.819	MHz
Max. RF power	P_{RF}	50	kW
coupling constant	(ϵ_y/ϵ_x)	0.1	-
horizontal emittance	ϵ_x	1.7×10^{-8}	m·rad
vertical emittance	ϵ_y	1.7×10^{-9}	m·rad
relative energy acceptance	$(\Delta E_{\mathrm{max}}/E)$	$0.98{\times}10^{-2}$	-
parameters at U250			
betatron function	β_x / β_y	5 / 13	m
relative energy spread	(σ_{E}/E)	7.5×10^{-4}	-
horiz./vert. electron beam size	σ_x / σ_y	299.3 / 148.7	µm
longitudinal electron beam size (FWHM)	σ_z	3 (100)	cm (ps)
horiz./vert. dispersion	η_x / η_y	-0.09 / 0	m

Synchrotron radiation generated in bending magnets (critical photon energy 2.3 keV), in the hybrid-magnet undulator U55 (photon energies from 55 eV to 1.5 keV), the electromagnetic undulator U250 (photon energies from 5 eV to 400 eV) and in the superconducting wiggler SAW (critical photon energies from 4.2 keV to 7.9 keV) is guided via 8 beamlines to user experiments. X-ray photo-emission spectroscopy (XPS), lithography, spin- and angle- resolved PES, X-ray diffraction/scattering are examples of user experiments performed at DELTA

beamlines [72, 73].

3.1.1 The VUV beamline BL 5

The VUV beamline BL 5 at DELTA is operated by the Forschungszentrum Jülich. It is equipped with a plane-grating monochromator (PGM), a photoelectron spectrometer (SES 2002 analyzer, VG Scienta [77]), a delay-line detector (DLD, Surface Concept GmbH [76]) and a spin-polarized low-energy electron diffraction (SPLEED) detector built by Focus GmbH [78] for spin detection. It is operated in the VUV and soft x-ray regime for angular- and spin-resolved photoelectron spectroscopy [74]. The layout of BL 5 in both side- and top-view is shown in Fig. 3.2.

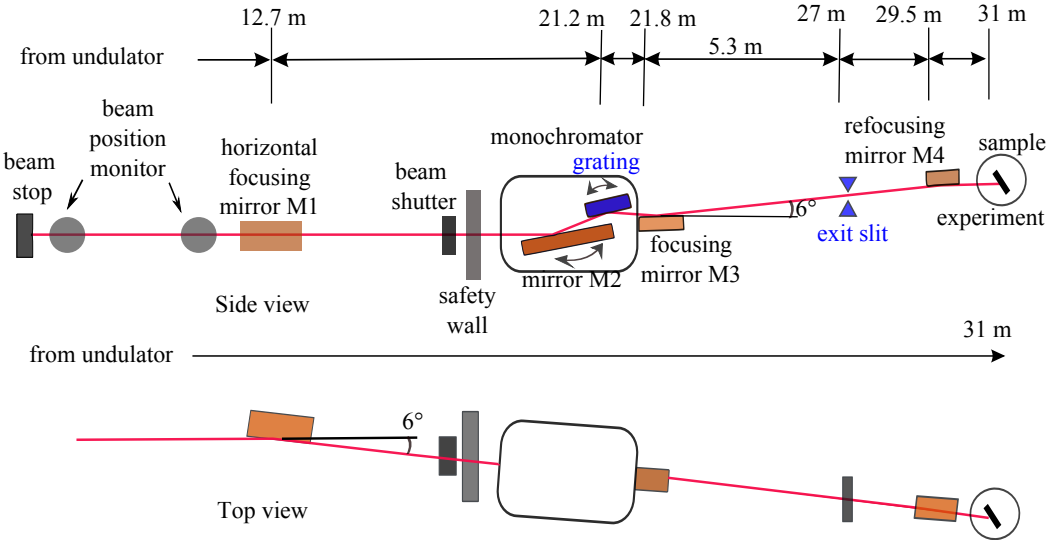

Figure 3.2: The layout of the VUV beamline BL 5 at DELTA with a plane-grating monochromator (PGM), focusing mirrors (M1, M3, M4), an experimental chamber, the distances from undulator U250 are indicated. In the side-view (top) and top-view (bottom) the angles are shown.

Within the radiation safety wall, there is a spherical focusing mirror (M1), which focuses the light on the sample in the horizontal direction. The incident angle of the beam on M1 is 3° and the reflectivity is 65% at a photon energy of 300 eV.

The PGM comprises a plane mirror (M2) and two gratings with 300 (used for low photon energies) and 1200 (used for high photon energies) lines per millimeter. A photon energy is chosen by the monochromator and focused by the focusing mirror M3 onto the exit slit. For selecting a certain photon energy, both mirror and grating in the monochromator are rotated around the horizontal axis. The rotation is carried out such that the fixed-focus constant c_{ff}

value[1] remains constant, i.e. the distance between the virtual source and the monochromator (and hence the beam focus point) remains constant while varying the photon energy. If the c_{ff} value is varied, the position of the exit slit should also be set to the new focus point by using the motorized translation stage of the slit. By applying a higher c_{ff} value, the virtual source lies further away and therefore it appears to be smaller. As a result, the resolution of the monochromator increases while the intensity of the beam decreases. The value of c_{ff} can be varied between 1 and 10.
In this work, values between $c_{\mathrm{ff}} = 1.5$ and 2.5 are used. The refocusing mirror M4 focuses the beam on the sample with a vertical size down to about 70 µm (rms). The energy resolution of the monochromator has been estimated to be $\Delta E/E = 10^{-4}$ at $E = 240$ eV and 10 µm exit slit size [75]. Further details of the beamline can be found in [75].

A scheme of the hemispherical photoelectron analyzer and the DLD is shown in Fig. 3.3. After hitting the sample, the radiation generates photoelectrons that pass through the electron lens and analyzer and reach the DLD. The lens (in angular mode) images the angular distribution of the electrons in the plane of the entrance slit, such that each point of this plane corresponds to a certain emission angle. Only electrons with a certain emission angle can pass through the slit and enter the analyzer. The angular range of the electrons is limited by the slit length; for the standard lens mode it is approximately ±7° with a typical angular resolution of 0.3°.

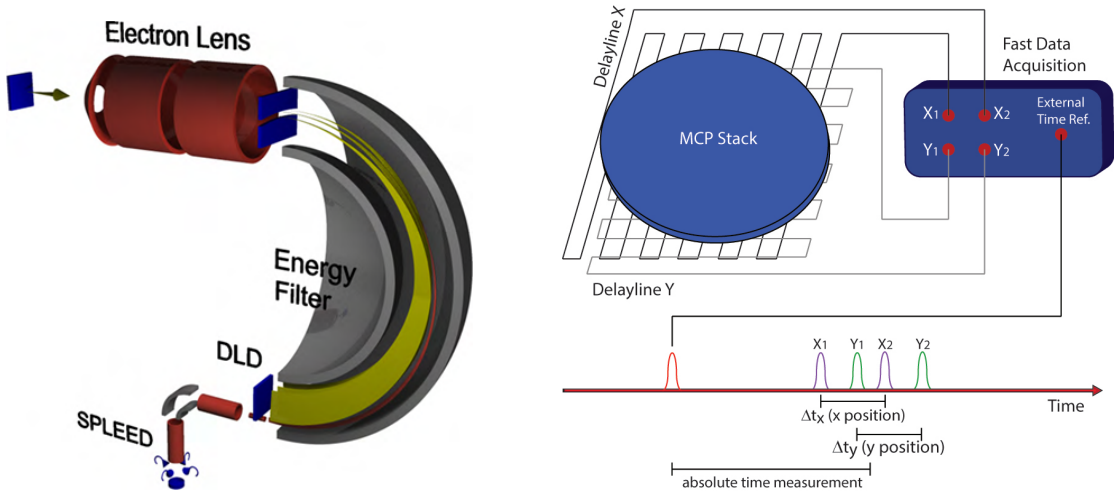

(a) (b)

Figure 3.3: Scheme of the hemispherical photoelectron analyzer (a) [74] and principle of a DLD (b) [76].

The analyzer, consisting of two conducting hemispheres, selects the electrons energy. A constant voltage is applied between the outer and inner sphere, which determines the pass

[1] $c_{\mathrm{ff}} = \sin\alpha / \sin\beta$; α and β are the incident and diffraction angles of the beam with respect to the surface of the grating.

energy i.e. the kinetic energy of the electrons that are able to pass through the analyzer. Electrons with an energy higher or lower than the pass energy will collide with the outer or inner sphere, respectively. The energy resolution δE of the analyzer is determined by the analyzer slit width w_{slit}, the sphere radius R_{sphere} and the pass energy E_{pass} [77]

$$\Delta E \simeq 2\frac{w_{\text{slit}} E_{\text{pass}}}{R_{\text{sphere}}}. \tag{3.1}$$

Thereby, for a 0.1 mm slit and using 1 eV pass energy, the energy resolution is 0.25 meV [77]. The overall energy resolution is a convolution of the energy resolution of the beamline monochromator and analyzer.

The photoelectrons hit a multi-channel plate (MCP) with an active dimension of 27.5 mm (energy direction) × 30 mm (angular). After multiplication, the photoelectrons are detected by the DLD, which generates an electric signal at opposite ends of the delayline in x and y direction. The arrival times of those signals $(t_{x1}, t_{x2}, t_{y1}, t_{y2})$ are measured by the data acquisition system using a time-to-digital converter (TDC). The position of each hit is determined by the time differences ($t_{x1} - t_{x2}$ and $t_{y1} - t_{y2}$), and the time coordinate by the sum of the arrival times ($t_{x1} + t_{x2} + t_{y1} + t_{y2}$) [76]. The reference time for the measurement is defined by an external start signal. With this technique, a two-dimensional picture of the angle versus kinetic energy is mapped directly onto the DLD without moving the sample. For time-resolved measurements, all counts at a certain time are integrated. The temporal resolution of the DLD is about 7 ps. However, the overall resolution is limited by the time-of-flight differences of the electrons inside the hemispherical analyzer and is strongly dependent on the photoelectron energy.

3.2 The CHG facility

A source for ultrashort VUV pulses based on the CHG principle is in operation at DELTA since 2011 [19–28]. The general layout of the CHG facility at DELTA is shown in Fig. 3.4(a). The purpose of the facility is providing radiation for time-resolved pump-probe experiments to study ultrafast processes, for example the demagnetization of ferromagnetic materials. The CHG facility comprises several beamlines, namely a seed, diagnostics, THz, and pump-pulse beamline.

Seed beamline

The laser pulses from a Ti:sapphire femtosecond laser system are sent to the undulator U250, either with its standard wavelength of 796 nm or with the second harmonic thereof

generated with a nonlinear crystal. In future, also the 3rd harmonic will be employed for seeding i.e. modulating the electrons energy with the field of laser pulses. A sketch of the seed beamline BL 3 [79] is shown in Fig. 3.4(b). The laser is focused by a telescope into the undulator. Initially, the telescope was built of three lenses, but for seeding with 398 nm they were replaced by curved mirrors to minimize the effect of group-delay dispersion that lengthens the pulses at short wavelengths. The motorized mirrors M1 and M2 are used to steer the laser beam with a resolution of about 1 µrad. Two diagnostics screens are used to determine the laser path along the beamline.

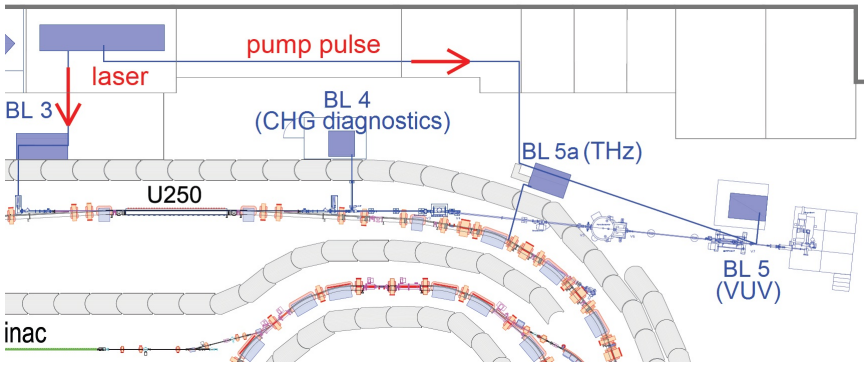

(a)

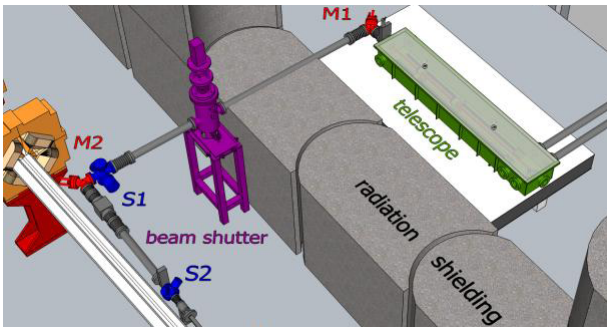

(b)

Figure 3.4: a) Layout of the CHG facility at DELTA, including the seed laser beamline (BL 3), the optical klystron (U250), the diagnostics hutch (BL 4), the THz beamline (BL 5a), the VUV beamline (BL 5), and the pump-pulse beamline. b) Layout of the seed beamline including the mirrors M1, M2, screens S1, S2 and the telescope chamber [79].

The size and position of the laser waist can be measured by guiding the laser leakage from one of the mirrors after the telescope back to a point at the laser laboratory which is located at the same distance from the laser source as the undulator is. The laser spot at this point is called the virtual waist. The waist size and position can be adjusted by moving the telescope and measuring the waist radius using a CCD beam-profiler (WinCamD-UCD12 from DataRay [101]) mounted on an optical rail.

The undulator U250 is an electromagnetic undulator consisting of three segments which

can be powered to form a so-called optical klystron (OK). These three parts (modulator, chicane and radiator, see Section 2.1.1 and 2.4.2) are powered by separate power supplies. The modulator is generally tuned to the wavelength of the seed-laser pulses. The strength of the chicane r_{56} must be optimized depending on the actual energy modulation. The CHG-radiation wavelength is chosen by tuning the radiator to harmonics of the seed wavelength. Finally, the CHG radiation is sent either via BL 4 to a diagnostics hutch for optimization and characterization or to the VUV beamline (BL 5) for detection and application in user experiments. The main parameters of the CHG facility are shown in Table 2.

Table 2: Specifications of the CHG Facility at DELTA

electron bunch:	
bunch length (FWHM)	$\sim$ 100 ps
single-bunch current/charge	up to 20 mA / 7.7 nC
revolution frequency	2.6 MHz
undulator:	
undulator period	250 mm
number of periods (modulator/chicane/radiator)	17 (7/3/7)
K value of modulator/radiator	0 - 10.5
r_{56} of the chicane	0 - 130 µm
max. magnetic field of U250	0.45 T
undulator gap	50 mm
Ti:sapphire laser:	
laser pulse energy @ 796 nm	up to 8 mJ
laser pulse energy @ 398 nm	up to 2.6 mJ
pulse duration (FWHM)	$\sim$ 40 - 70 fs
laser repetition rate	1 kHz
typical laser waist size (2σ @ 796 nm)	$\sim$ 700 µm $\times$ 500 µm

THz beamline

A few meters downstream of the undulator, path length differences of the off-energy electrons cause a sub-millimeter gap in the density profile of the electron bunch which leads to the emission of coherent THz radiation. This radiation is extracted via a dedicated beamline (BL 5a) and can be used as a diagnostics tool for CHG experiments as a sensitive measure for the energy modulation in the undulator, as well as for time-resolved far-infrared spectroscopy [80, 81].

The THz beamline is equipped with an InSb bolometer with a response time of about 1 µs, a $YBa_2Cu_3O_{7-x}$ (YBCO) detector with a response time of less than 17 ps [84, 85], and an FT-IR spectrometer. The THz signal detected by the InSb bolometer is maximized by tuning the vertical and horizontal orientations of mirror M1 and M2 in the seed beamline as well as the laser arrival time. This determines the optimum overlap condition for maximum energy modulation.

A dedicated beamline has been constructed to guide a fraction of the laser pulses to the experimental stations at BL 5 and BL 5a for the purpose of pump-probe experiments; for details see Section 3.3.

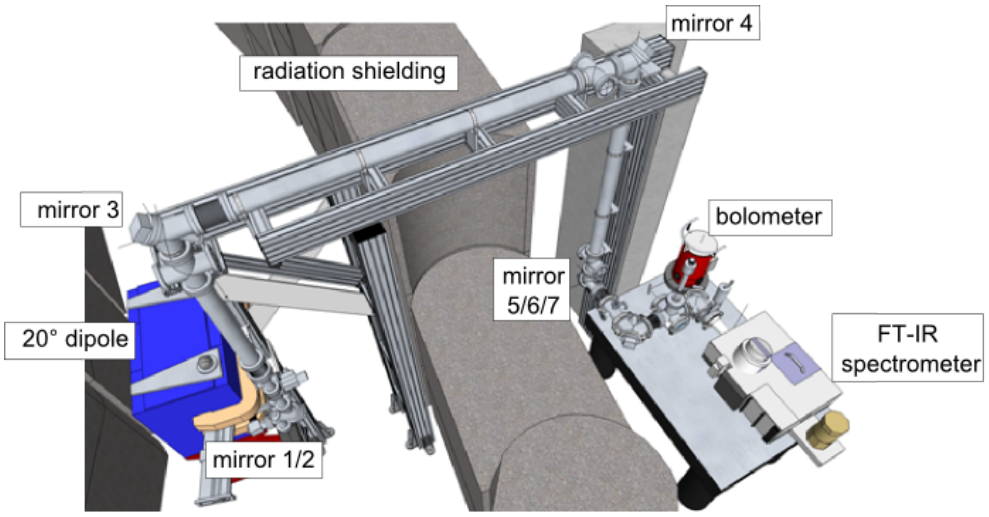

Figure 3.5: The layout of the THz beamline including the mirrors, InSb bolometer and the FT-IR spectrometer [80].

3.2.1 Diagnostics and detection of CHG radiation

Approximately five meters downstream of the undulator (Fig. 3.4(a)), the radiation is sent to the diagnostics hutch (BL 4) by using a water-cooled copper mirror. Various tools in the diagnostics hutch are used to maintain the laser-electron overlap and to detect and optimize the CHG radiation. The setup of the table in the diagnostics hutch is shown in Fig. 3.6.

Transverse overlap between laser pulses and electron bunches

In order to achieve transverse overlap between the laser beam and the electron bunches, the radiation is divided with a beamsplitter into two parts and sent to white screens. Screen 1 is located inside the diagnostics hutch and screen 2 outside the hutch at a distance of approximately 8 meters. The undulator radiation and laser spots on the screens are monitored with CCD cameras during the transverse alignment procedure using the mirrors M1 and M2 in the seed beamline. Previously, the transverse overlap was achieved by monitoring two

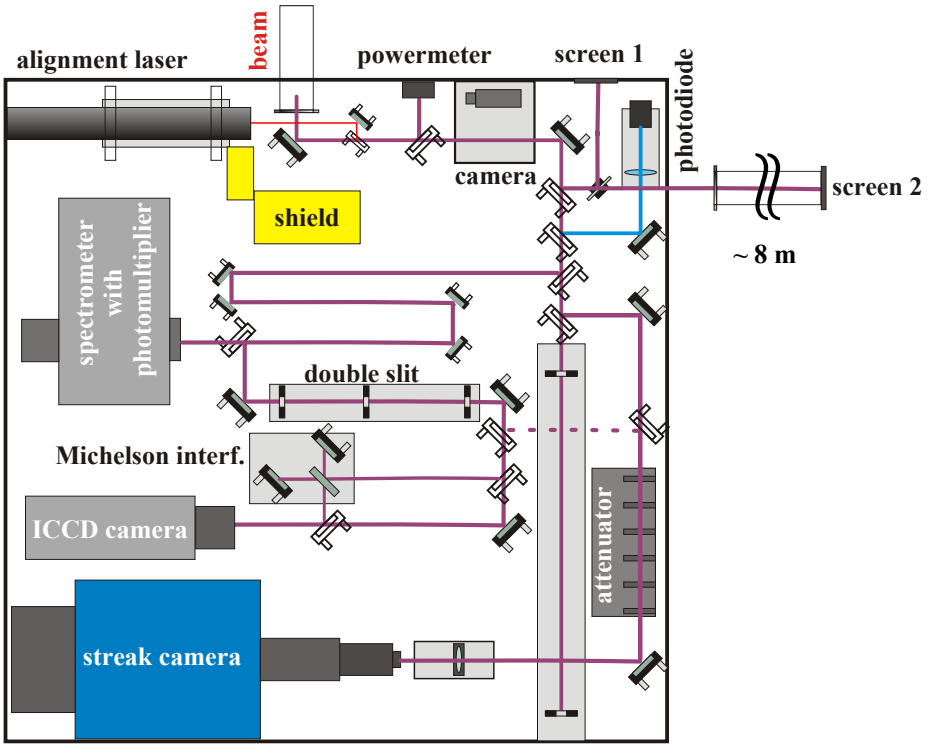

Figure 3.6: The layout of the optical table in the diagnostics hutch, including diagnostics and detection tools for the transverse overlap (screen 1, screen 2 and camera), longitudinal overlap (photodiode and streak camera), CHG detection (photodiode, spectrometer, photomultiplier), and coherence measurements (double slit, Michelson interferometer, ICCD camera).

different points inside the undulator by two CCD cameras together with $70 - 300$ mm zoom lenses. One camera was focused at the beam waist at the center of the modulator, and the other several meters downstream of the modulator. Sample images from one CCD camera are displayed in Fig. 3.7. The images of the new method are more clear and analyzing them is more straightforward.

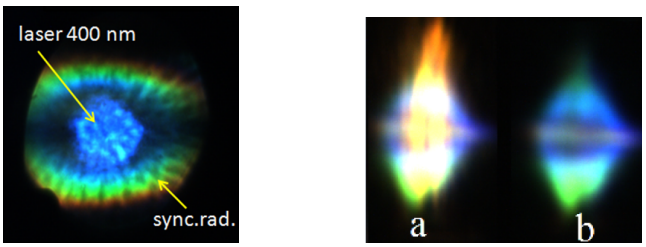

Figure 3.7: Images from CCD cameras recording the diffuse radiation on the screen in the diagnostics hutch (left), and with zoom lenses focused to a distance of 14 m in the undulator (right), with and without laser (a,b).

In addition, the electron orbit can also be adjusted to match the optimized laser beam path. A clear distinction between the laser and undulator radiation can be made by blocking the laser periodically using a 1-Hz chopper. After getting a first THz signal, a finer alignment

can be done by optimizing the THz and CHG signals through small adjustment of the mirrors.

Longitudinal overlap between laser pulses and electron bunches

The laser pulses must be synchronized to the accelerating RF frequency of the storage ring (f = 499.8 MHz). The synchronization scheme is shown in Fig. 3.8. The frequency of the laser oscillator is locked to $f/6 \approx 83.3$ MHz, and the phase shift is continuously measured and controlled with a commercial synchronization system (Synchrolock-AP [83]). In addition, a signal with the revolution frequency ($f/192$) is sent to a delay generator, which creates a 1-kHz signal to trigger the pump laser and the Pockels cells of the Ti:sapphire laser amplifier.

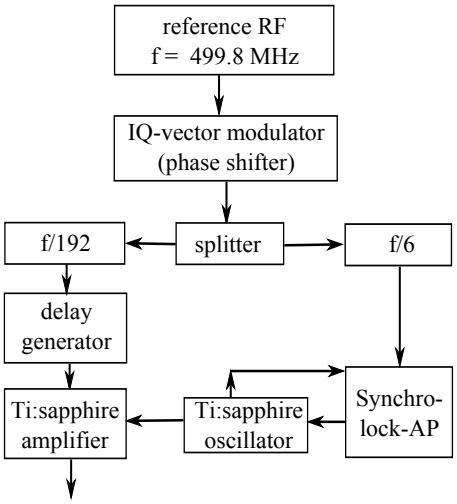

Figure 3.8: Scheme of the synchronization of laser pulses with electron bunches.

The delay between the laser pulse and the electron bunch can be adjusted by a digital phase shifter ("vector modulator") with a minimum step width of 1 ps. The vector modulator is controlled through the control system of DELTA.

For detecting the longitudinal overlap, the laser and the synchrotron radiation pulses are monitored using a fast photodiode detector, and their respective delay is measured using an oscilloscope with 2 GHz bandwidth. Alternatively, the laser and synchrotron light can be monitored by a streak camera with a temporal resolution of $\sim$ 10 ps, limited by space-charge effects near its photocathode from the fs-laser pulses. Figure 3.9(a) shows an image recorded by the streak camera with a delay of $\sim$ 200 ps between the laser signal and the electron bunch, and also one with nearly perfect overlap. Reducing the laser intensity and thus the space charge further is not possible, since the laser spot on the CCD would become nearly invisible due to the low repetition rate of the laser pulses. Figure 3.9(b) shows the signal of the streak camera projected onto the horizontal axis.

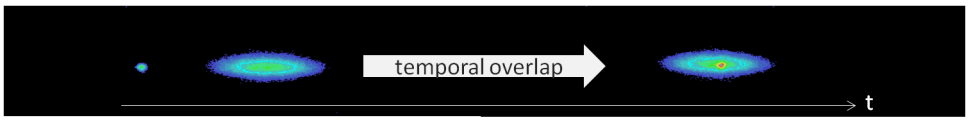

(a)

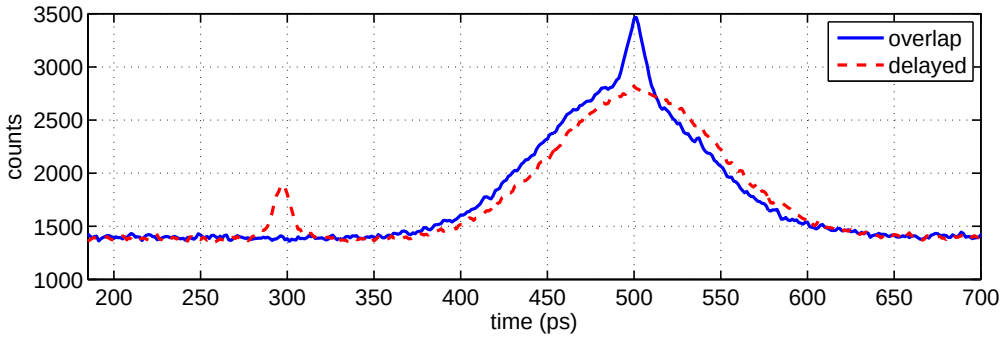

(b)

Figure 3.9: a) An example image from the streak camera showing a laser pulse and an undulator radiation pulse with a remaining mismatch of about 200 ps (left), and synchronized (right). b) Signal of the streak camera projected onto the horizontal axis, showing the electron bunch profile with a FWHM length of 102 ps overlapping with the laser pulse (blue curve) and delayed by 200 ps (red dashed curve).

Detection of CHG radiation

After achieving both temporal and spatial overlap, coherent THz radiation is detected at the THz beamline, and CHG radiation can be detected at either BL 4 or BL 5. At BL 4, an avalanche-photodiode (APD) equipped with a bandpass filter is used to detect the CHG radiation [82], and its spectrum is measured using a Czerny-Turner type spectrometer with a photomultiplier (PMT) or an APD at its exit slit. Although a more easy-to-handle CCD spectrometer is available, the PMT or APD is used in order to resolve the signals from a single revolution (384 ns) that contains the laser pulse (1 kHz repetition rate), while the CCD spectrometer integrates over many turns.

3.3 Design and construction of a pump-pulse beamline

Owing to its short pulse duration, the main applications of CHG radiation are time-resolved experiments. Due to the fact that the CHG radiation is synchronized with a laser, it can be used to perform time-resolved pump-probe experiments with laser pulses used as pump and CHG as probe. For this purpose, some part of the laser pulses (up to 10 %) is sent directly to the sample at BL 5 (Fig. 3.4(a)). Because of the long distance from the laser to the sample, an evacuated beamline has been designed and constructed in the frame of this thesis. In this

Section, the construction and the characteristics of this beamline are described, and the first commissioning results are presented in the next Chapter.

The construction of a beamline involves the design and assembly of both mechanical and optical elements as well as vacuum and electronic components. The mechanical parts include pipes, flanges, mirror chambers, vacuum components, diagnostic screens etc., and the optical part comprises two telescopes, an autocorrelator and a delay stage. In addition, the stability of the laser beam has to be maintained by means of an optical feedback system.

The total distance from the laser source to the sample is about 53 m given by the path length of the laser pulses to the modulator, and the CHG pulses from the modulator to the sample. In order to transfer the laser light over such a long distance, various aspects must be taken into account. The main criteria for designing and constructing the pump-pulse beamline and its components are summarized as follows.

- Mechanical vibrations have to be avoided, i.e. the mounting of the vacuum pipes and especially mirrors should be very stable.
- The beamline should be arranged in such a way that its length is equal to the path length of the probe pulse starting from the laser system.
- The beamline should not block passage ways.
- In order to avoid laser losses and fluctuations due to air movement, the beamline should be evacuated down to a few mbar or less.
- The laser should be focused on the sample with a certain size.
- An arrival time variation from picosecond to nanosecond with respect to the probe pulse is required.
- The total amount of dispersive material in the beamline should be as small as possible to avoid temporal stretching of the pulse and other nonlinear effects of ultrashort laser pulses.
- An extra hutch has to be built close to the sample chamber in which the laser beam, stability and timing are adjusted.
- The angle between the pump and probe beam at the sample should be small to ensure optimum time resolution.
- BL 5 had to be slightly modified to merge it with the pump-pulse beamline.

- All mirrors and screens should be controllable by the control system of DELTA based on EPICS.

According to these requirements, the path and the layout of the beamline has been constructed as described in the next Sections.

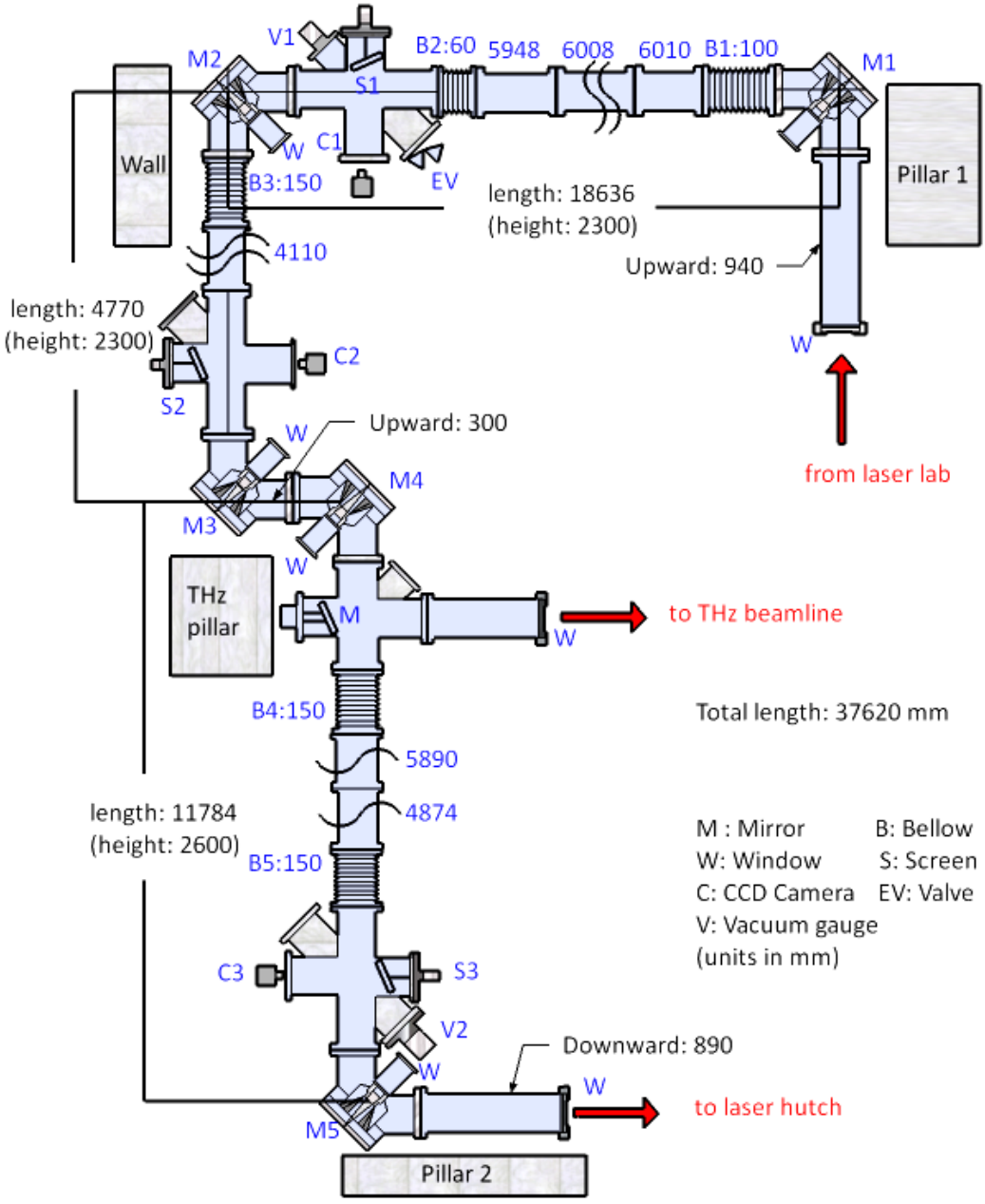

Figure 3.10: A 2-D sketch of the vacuum section of the pump-pulse beamline including mirrors (M), bellows (B), cameras (C), diagnostics screens (S), windows (W), valves (EV), vacuum gauges (V), 4-, 5- and 6-way crosses. The length of each pipe piece, the total length of each section and the height above ground are denoted in mm. All pipes and flanges are CF63 (63 mm inner diameter) except viewports of the mirror chambers (they are CF35).

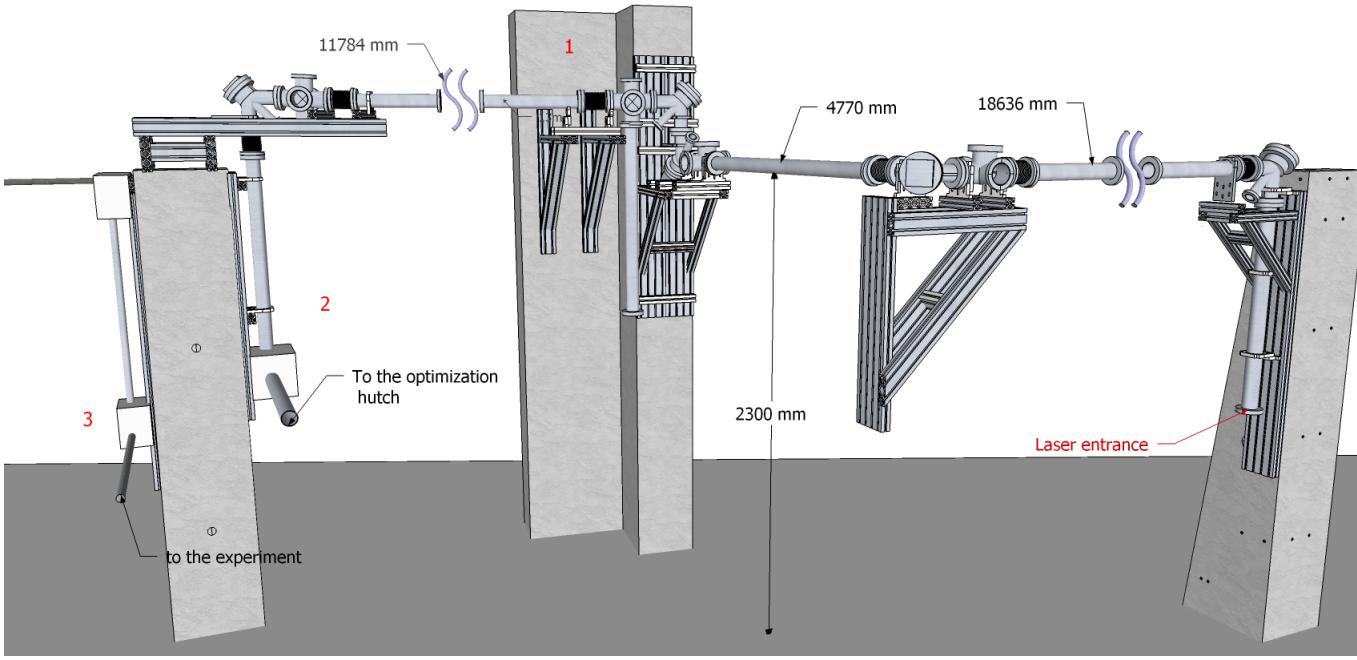

(a)

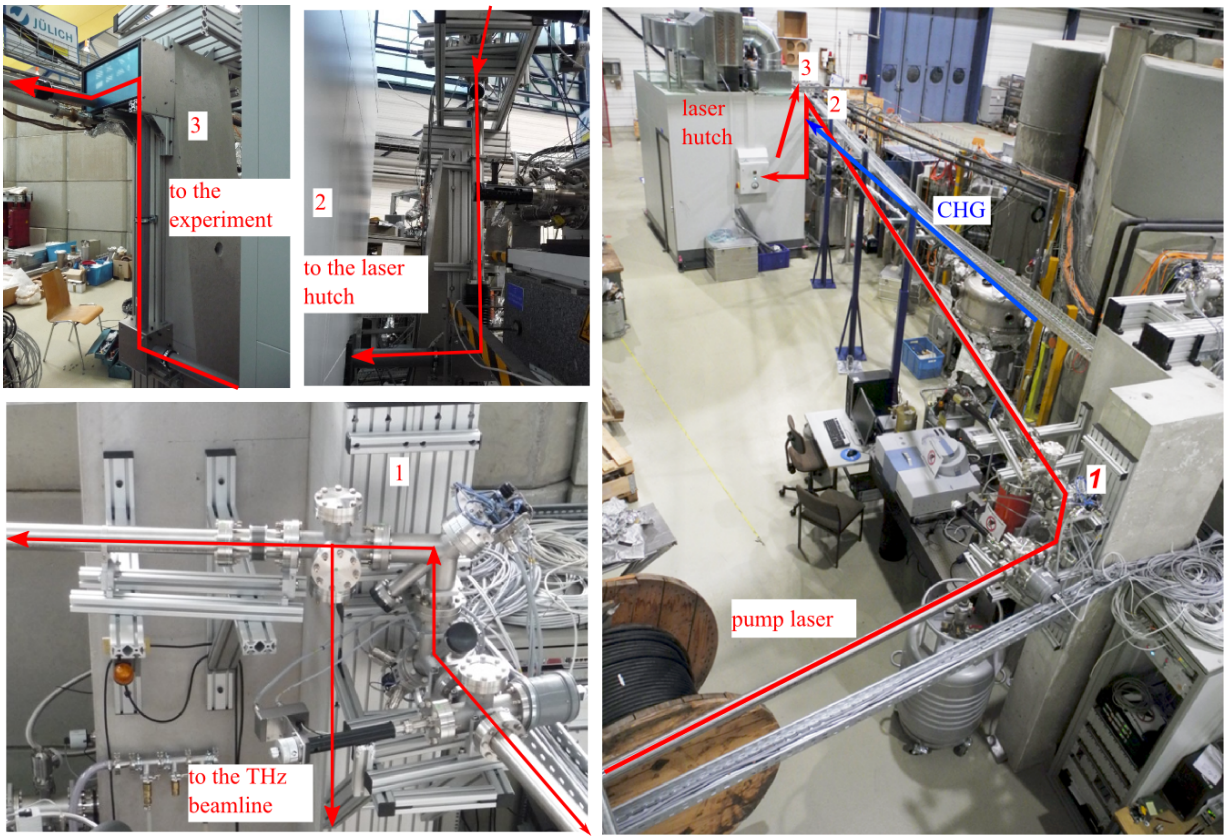

(b)

Figure 3.11: A 3-D sketch of the pump-pulse beamline starting from the laser laboratory towards the optics hutch and the experiment (a). Photographs of the pump-pulse beamline (b). Positions marked by 1,2,3 respectively indicate the location of the THz beamline, the entrance to and the exit from the optics hutch.

3.3.1 General mechanical design, assembly and components

The general layout of the mechanical design and the vacuum components of the pump-pulse beamline is illustrated in Fig. 3.10. In addition, a 3-D view is shown in Fig. 3.11(a).
In the laser laboratory, the beam is sent upward through a short pipe to the first mirror M1 in a height of 2.3 m. Then, the beamline passes through the walls of the neighboring laboratories and reaches the second mirror M2 at a distance of 18.6 m from M1.
Afterwards, the beamline goes towards the THz beamline from which proceeds at a non-normal angle. A periscope with the mirrors M3 and M4 increases the height of the beamline by 0.3 m. The beamline reaches the last mirror chamber M5 at a distance of 11.8 m from M4, and is sent down to the height of 1.08 m above the floor, and finally arrives in the laser optics hutch. A top-view of the beamline path can be seen in Fig. 3.4(a).

All pipes are made of stainless steel with an inner diameter of 63 mm which is necessary to avoid diffraction losses of the laser. The pipes are connected with CF-flanges. Mirror M1 is mounted on a concrete pillar [90] in the laser laboratory. M2 is supported by a concrete wall. M3 and M4 are supported by the pillar at the THz beamline. Because laser-pump/THz-probe experiments are planned for the future, an extra 5-way cross is placed here to insert a mirror that sends the laser pulses to the THz laboratory. The last mirror M5 is connected to another concrete pillar directly before the optics hutch. The material of the pillars is polymer concrete for its ability to damp floor vibrations and for its small temperature-dependent expansion. Photographs of the pump-pulse beamline after completion are shown in Fig. 3.11(b). In the following Sections, components of the beamline are described individually.

Mirror chambers, vacuum system, windows and viewports

All mirrors in the vacuum chambers are motorized and controlled remotely via the control system of DELTA based on EPICS. The mirror chambers are based on a design by BESSY [91]. The mirrors are mounted to a spring cage, which defines the center of rotation on the mirrors surface. A joystick-like rod leads to the back of the flange where it can be moved by two stepper motors. An image of the mirror mount and the design of the chamber are shown in Fig. 3.12.

The mirror chamber has a CF35 viewport made of quartz glass which is used to align the laser beam. The position of the laser spot on the mirror M1 can be determined by using a CCD camera mounted on the viewport of the M1.

The beamline can be pumped down to to a pressure of $\sim 10^{-9}$ mbar using a turbo pump. After removing the pump, the pressure rises to a few 10^{-3} mbar in about two days and remains in this range for a few months.

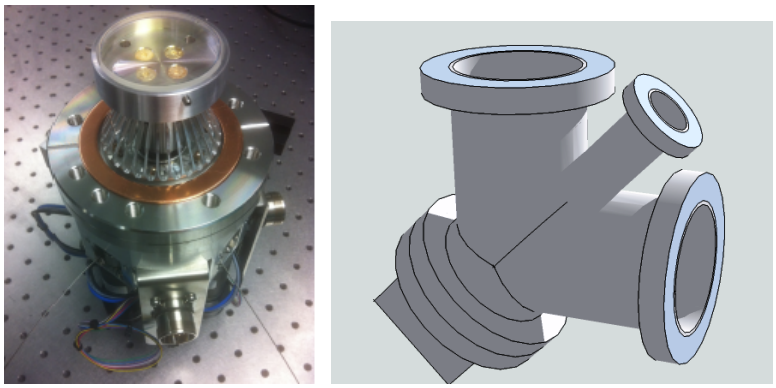

(a) (b)

Figure 3.12: A photo of the mirror mount equipped with a CF flange (a) and a sketch of the mirror chamber into which the mirror mount is inserted.

The entrance and exit windows of the beamline are made of quartz glass with 6.35 mm thickness, 2 inch diameter, and a surface flatness of $\lambda/10$ (Laser Components PW2025UV [98]). Both sides of windows have a broadband anti-reflection coating (BBAR) for the range of 633 - 1064 nm with a reflectivity of less than 0.4% at 800 nm. The reflection curve of the windows is shown in Fig. 3.13. They are mounted on special CF63 flanges and attached to the vacuum pipe.

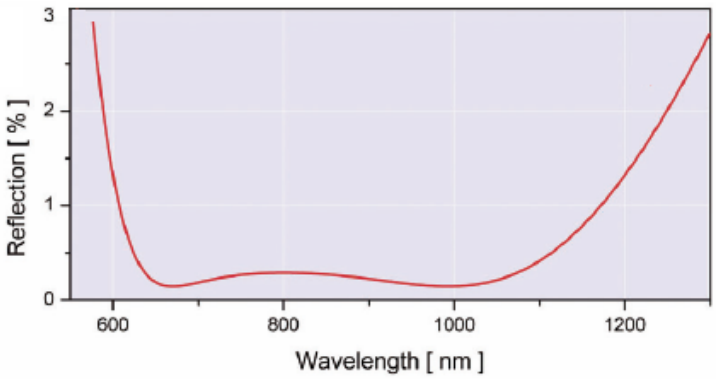

Figure 3.13: The reflection curve of 0° broadband anti-reflection coated windows used in the pump-pulse beamline [98].

Diagnostics screens

In order to monitor and align the transverse position of the laser beam along the beamline, three aluminum screens are installed in the beamline, directly before the mirror chambers M2, M3 and M5. The screens are located on one side of a cross, while a CCD camera is mounted on the opposite side focused on the screen. A sketch and photos of a screen are shown in Fig. 3.14. The surface of the screens has been roughened with abrasive blasting in order to diffuse the incident light. The center of the screen is marked with a cross-hair.

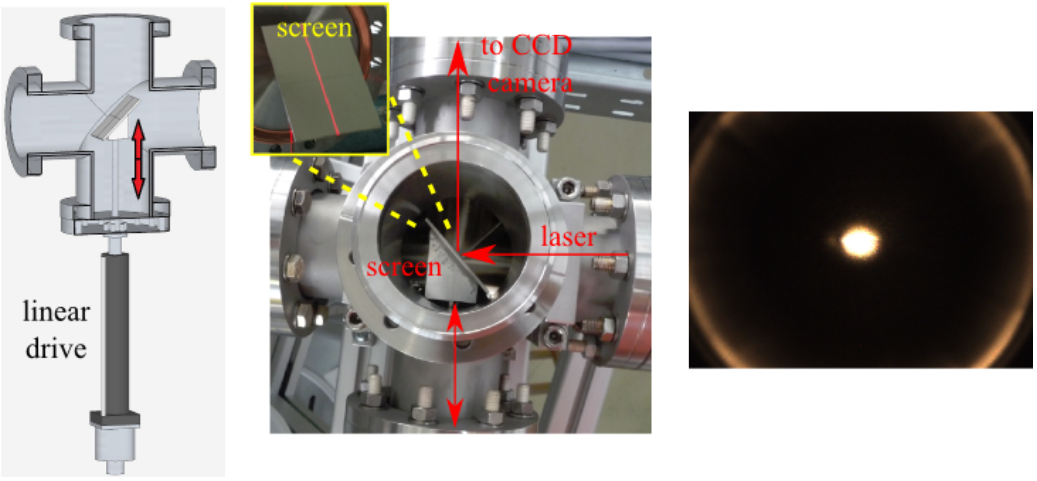

Figure 3.14: Design of the diagnostic screen mounted on a linear stage attached to a cross (left). A photo of the screen mounted inside the beamline (center). Image of the laser spot on the screen at the center of the vacuum pipe, recorded by a CCD camera (right).

The screens are mounted on a linear drive, driven by a stepper motor and controlled via the control system of DELTA.

Merging the pump-pulse beamline with the VUV beamline

A fork-shaped pipe with a CF100 flange at one end and two CF35 flanges at the other end is used for merging the two beamlines with an angle of about 6° between them (Fig. 3.15) [88].

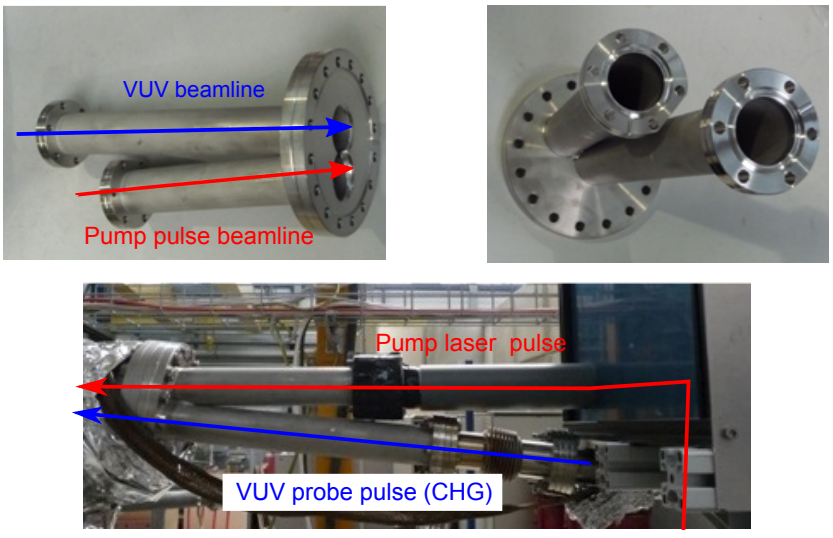

Figure 3.15: Photos of the flange designed for merging the pump-pulse beamline into the VUV beamline.

The limiting apertures in the VUV beamline for the pump pulses are the entrance window of the VUV beamline, the refocusing mirror and its mount and screws, a CF35 flange at the

exit of the mirror chamber, and the following bellow (Fig. 3.16). The laser path passes below the refocusing mirror in the VUV beamline (Fig. 3.16).

The horizontal angle of the CHG beam with respect to the ground before entering and after leaving the mirror chamber is 6 and zero degree, respectively (Fig. 3.2 and 3.16). The pump-pulse beam has an slight horizontal angle such that it passes below the mirror and hits the sample at the same point as the CHG beam.

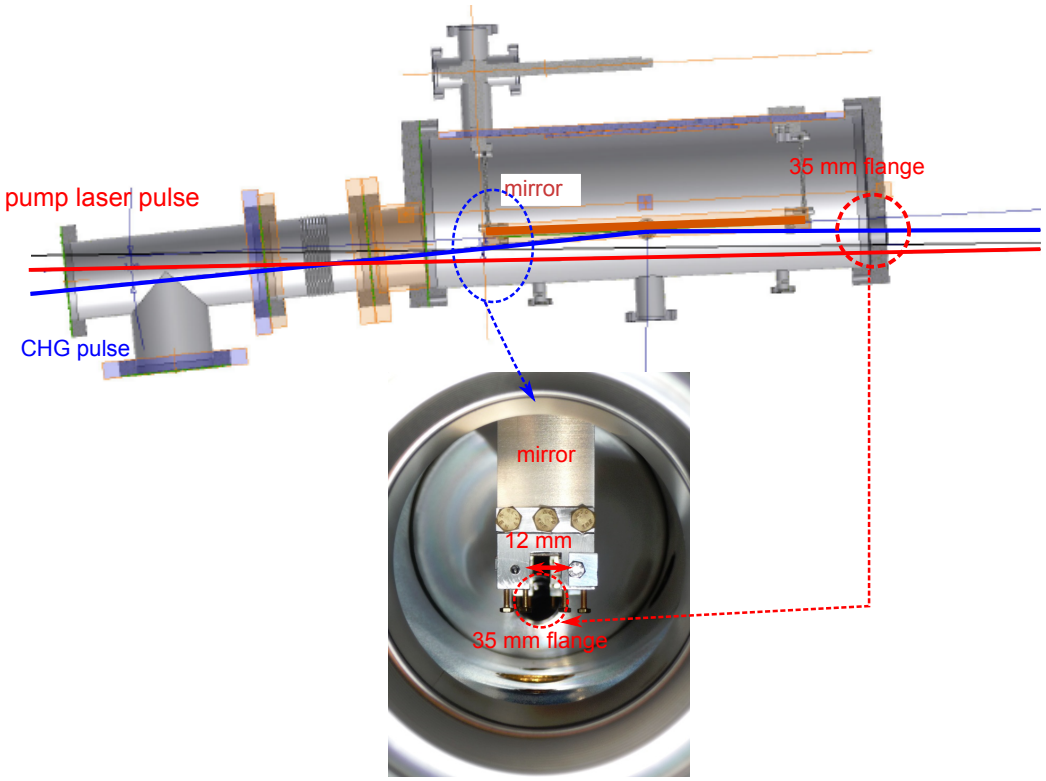

Figure 3.16: Vacuum chamber of the refocusing mirror and limiting apertures inside the chamber; side view (top) and beam view (bottom). The horizontal angle of the mirror is about 3° and can be adjusted by screws at the top of the chamber.

3.3.2 Beamline optical design and components

All mirrors in the vacuum section are plane dielectric mirrors with high reflection (HR) coating for 800 nm (Fig. 3.17) on a fused silica substrate with 50 mm diameter. These mirrors have a reflectivity above 99.9% at 800 nm, adding up in total to $\sim 1\%$ laser power losses throughout the vacuum section of the beamline. The mirror surface has a flatness of about $\lambda/10$ and a GDD value of <20 fs^2. A telescope system has been designed to focus and control the size of the laser beam, as described in the following Section.

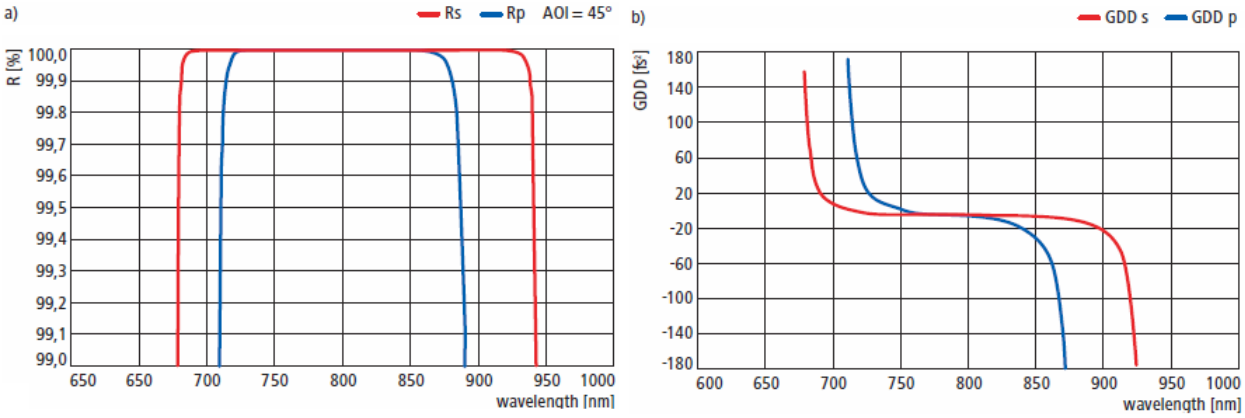

Figure 3.17: Reflectance (a) and GDD (b) spectra for the deflecting plane mirrors with a beam angle-of-incidence (AOI) of 45°. The reflectivity is more than 99.9% in a bandwidth of about 160 nm [99].

Telescope

Assuming a 2D-Gaussian intensity profile with a beam radius of $w = 2\sigma$, the diameter of a circular aperture A should be larger than $4.6\,w$ in order to avoid intensity losses due to diffraction from a sharp-edged aperture. To fulfill this condition, two telescopes and one focusing lens are used to focus and guide the laser beam through the pump-pulse beamline. The $A = \pi w$ criterion gives 99% power transmission but causes diffraction ripples with an intensity variation of $\Delta I/I \approx \pm 17\%$ in the near field and intensity reduction of $\approx 17\%$ in the far field [32].

◇ *First telescope* (refractive telescope)

A refractive telescope focuses and sends the light to the optics hutch. Two lenses are used, a concave one with a focal length of $f_1 = -1$ m and a convex one with a focal length of $f_2 = 1$ m. The lenses are placed ~ 1 m after the amplifier about 5 cm apart from each other. The setup of the optical elements on the laser table in the laser laboratory is shown in Fig. 3.18.

◇ *Second telescope* (reflective telescope)

Using a second telescope in the optics hutch enables more stable and accurate tuning of the laser spot size on the sample. Inside the hutch, the light is focused again using a two-mirror telescope. A concave mirror with a curvature radius of 2 m focuses the beam, then the beam is diverged by a convex mirror with a radius of 1 m. The second curved mirror and an additional plane mirror are mounted on a micrometer stage for fine tuning of the focus (Fig. 3.20). In order to avoid beam steering while moving the stage, the direction of motion of the stage is set parallel to both the incoming and the outgoing beam.

◇ *Final focusing lens*

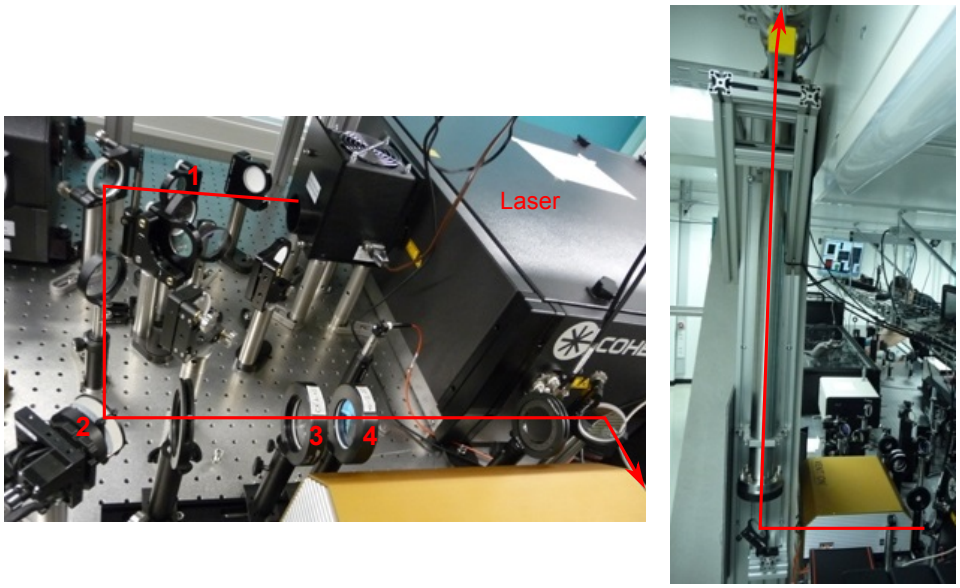

Figure 3.18: Left: Setup in the laser laboratory. Beam splitter (1), first actuator of the optical feedback system (2), plano-concave (PLCC) lens (3), plano-convex (PLCX) lens (4). Right: entrance to the vacuum pipe.

The smallest aperture in the beamline is the vacuum window at the entrance of BL 5 ($\sim$ 20 mm). In order to get a small beam spot at this aperture, a focusing lens is located about 2.8 meters before the sample and $\sim$ 0.5 m before the vacuum window which is the closest possible place.

The telescope calculations were performed by using the ray transfer matrices for Gaussian optics as explained in Sec. 2.2. The required transfer matrices are listed in Table 3, and the actual parameters of the setup can be found in Table 4.

The curved mirrors are coated for high reflectivity at zero degree, and the lenses have anti-reflection coatings for zero degree.

The total optical ray-transfer-matrix of the pump-pulse beamline (M) reads

$$M = (S_6 \times L_3) \times S_5 \times (M_2 \times S_4 \times M_1) \times S_3 \times (L_2 \times S_2 \times L_1) \times S_1 \,. \tag{3.2}$$

component	thin lens	curved mirror	drift space
matrix	$L = \begin{pmatrix} 1 & 0 \\ -1/f & 1 \end{pmatrix}$	$M = \begin{pmatrix} 1 & 0 \\ -2/R & 1 \end{pmatrix}$	$S = \begin{pmatrix} 1 & d \\ 0 & 1 \end{pmatrix}$

Table 3: The transfer matrices for a lens with focal length f, a curved mirror with the radius of curvature R, and a drift space with length d.

Table 4: Parameters of the optical components in the pump-pulse beamline.

element		value [m]	remarks
lenses (L):	f_1	-1	L_1 (PLCC)
	f_2	1	L_2 (PLCX)
	f_3	2	L_3 (PLCX)
mirrors (M):	R_1	2	M_1 (CC)
	R_2	-1	M_2 (CX)
drift spaces (S):	d_1	1.00	source $-L_1$ (in air)
	d_2	0.05	$L_1 - L_2$ (in air)
	d_3	42.25	$L_2 - M_1$ (in vacuum)
	d_4	0.45	$M_1 - M_2$ (in air)
	d_5	6.35	$M_2 - L_3$ (in air)
	d_6	2.90	L_3- target (in vacuum)

A Matlab script was written to trace the beam size and divergence along the beamline. The initial parameters of the Ti:sapphire laser used for this calculations are the $1/e^2$ beam radius $w_1 = 5$ mm, the divergence $\theta_{\text{div}} = 0.03$ mrad, and $M^2 = 1.5$ [79]. The laser beam radius along the beamline calculated using the values given in Table 4 is shown in Fig. 3.19 with a radius of $w = 180$ µm at the sample. The beam size on the sample can be changed by varying the distance between the mirrors in the reflective telescope using a manual micrometer stage. The position of the last lens is fixed.

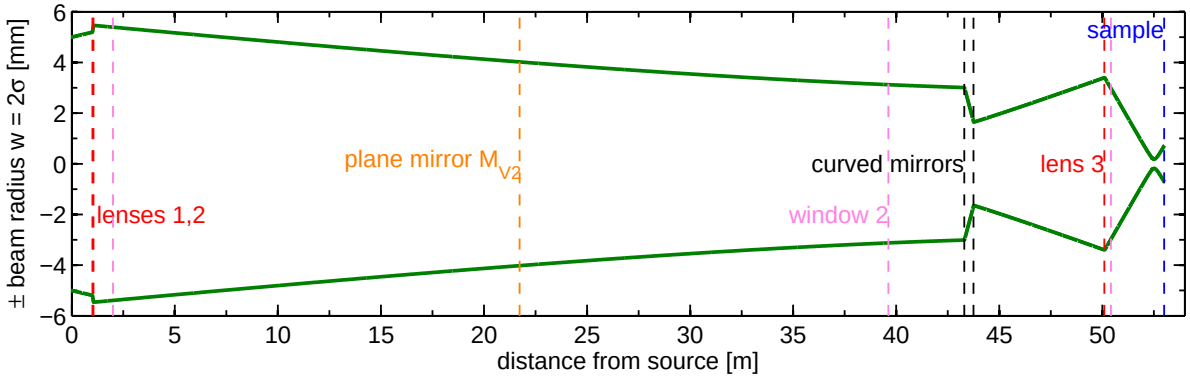

Figure 3.19: The laser profile in the pump-pulse beamline calculated by ray transfer matrices in Gaussian beam optics. The position of the windows, mirrors, curved mirrors, lenses and sample are marked by colored dashed lines.

The pump-pulse beamline comprises in total 5 periscopes: in the laser laboratory, on the THz pillar (with a non-normal angle of about 97°), at the exit of the vacuum pipe before the optics hutch, in the hutch, and at the BL 5 entrance (see also Figs. 3.11 and 3.20). Each of these periscopes changes the beam polarization, because the horizontal angle between the

incident and the outgoing beam in them is either 90° or 97°.

Optics hutch

An air conditioned laser hutch has been constructed close to the sample chamber in which the the laser waist and stability are optimized. It accommodates an optical table, a delay stage, a feedback system, the reflective telescope and a few other diagnostic tools such as a FROG device. The setup of the optical elements on the laser table is shown in Fig. 3.20. The delay stage is used to adjust the delay between the pump and the probe beam in the sub-ps range. The maximum travel range of this stage is 600 mm with a resolution of 1.25 µm. It is controlled by a LabVIEW program on a local PC [89].

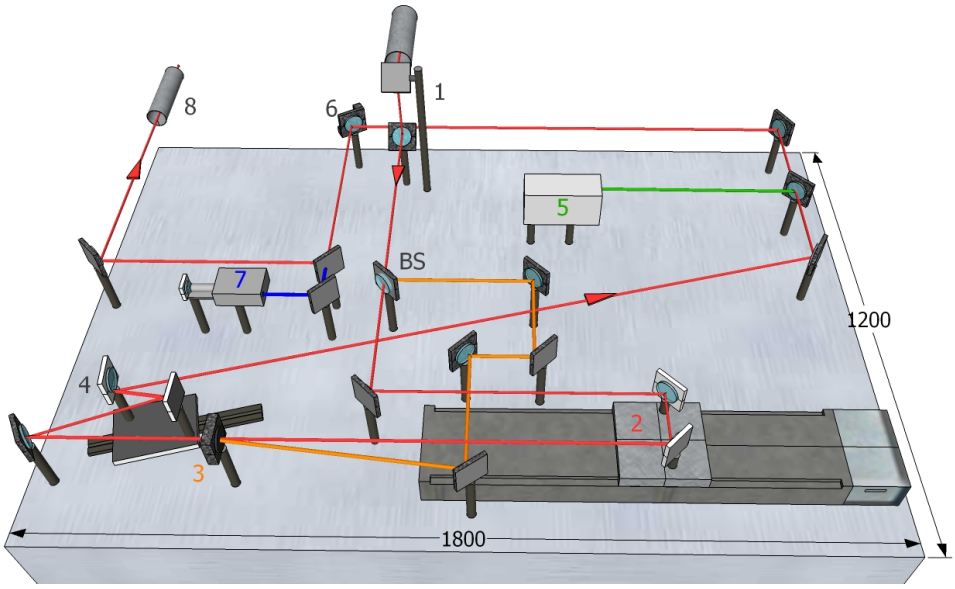

Figure 3.20: Setup of the optical table in the optics hutch. Periscope (1), delay stage (2), SiC photodiode (3), telescope (4), FROG (5), motorized mirror of the optical feedback system (6), detectors of the optical feedback system (7), exit towards BL 5 (8).

Optical feedback system and laser beam stability

A commercial feedback system ("4De Aligna" from TEM electronic [92]) is used to stabilize the laser path in both angle and position with a presumed accuracy of about 1 µrad and 1 µm, respectively. The system consists of two motorized mirrors and two position-sensitive detectors. The mirrors are equipped with stepper motors and also piezo sensors for fine adjustment. A simplified scheme of the system is shown in Fig 3.21.

The first motorized mirror (A1) is located in the laser laboratory as shown in Fig. 3.18, the second one (A2) in the optics hutch as shown in Fig. 3.20. The distance between A1 and A2 is about 45 m. The large distance between these two mirrors enables a better accuracy in the correction of beam drifts along the whole beamline before the detectors. The leakage from the mirror 0.6 m after A2 is split into two parts by a beamsplitter (Fig. 3.21). One part

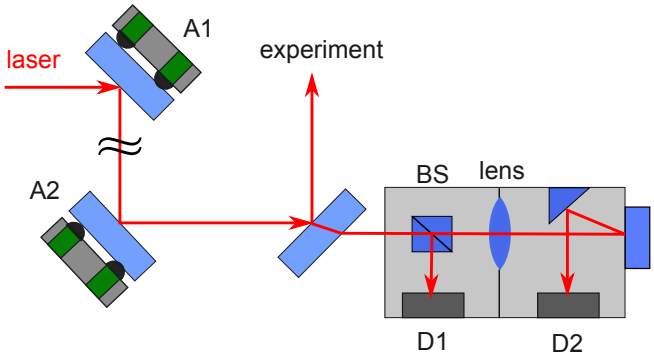

Figure 3.21: Setup of the Aligna feedback system. A1 and A2 are the first and second actuator. D1 and D2 are detectors. A part of the beam is sent to the detectors, and the position and angle of the laser beam are corrected by the actuators.

is sent to the first detector (D1), the other one to the second detector (D2) after passing through a focusing lens with $f = 13$ mm. D2 is located at the focal point of the lens and thus only detects angular fluctuations, while D1 is responsible for detecting position fluctuations. The signals from D1 and D2 are sent to a controller which continuously sends feedback signals to A1 and A2, stabilizing the position and angle of the laser beam on the detector.

Since the feedback system can only correct fluctuations and drifts occurring before the detectors, the beam path between the detectors and sample should be as short as possible. Due to the space limitations, the last detector is located about 6 m away from the sample. The commissioning of the pump-pulse beamline and the feedback system are discussed in the next Chapter.

4 Preparations for Pump-probe Experiments

After construction, the pump-pulse beamline was evacuated and the laser beam was sent through the beamline and aligned. During commissioning of the beamline, the beam size, intensity, stability, spectrum, polarization and pulse duration was measured and the temporal and transverse overlap with the seed laser on the sample was established.
The VUV beamline (BL 5) described in section 3.1.1, was used to detect the CHG radiation below a wavelength of 200 nm. In addition, the CHG radiation was characterized in this beamline for various configurations of the undulator, monochromator and DLD. By varying the c_{ff} value (see section 3.1.1), the aperture widths and the angle of the horizontal-focusing mirror, the beamline was fine-tuned to achieve the best ratio of CHG to spontaneously emitted (SE) radiation. By these means, the first preparatory steps for a laser-pump CHG-probe experiment were taken. In this Chapter, the results of the characterizing measurements at both the pump-pulse and the VUV beamline are presented and discussed.

4.1 Commissioning of the pump-pulse beamline

In order to perform a pump-probe experiment, several conditions should be fulfilled by the pump-pulse beam. Primarily, the pulse duration should remain in the femtosecond range and not be significantly lengthened due to nonlinear effects in the dispersive material of the beamline. Also, the aperture size should always stay well above the diffraction limit of the beam to avoid power losses. The laser power transmitted through the beamline to the sample should be high enough to excite the sample. In addition, the laser pointing (*x,y* positions on the sample) should be stable.

Beam diameter

To verify the telescope calculations (see Section 3.3.2), the beam size was measured at several points along the beamline using the knife-edge technique. Here, the laser beam spot is cut from one direction with a sharp blade, and the power of the clipped beam is measured as a function of the blade position. The size of the beam can be derived by fitting the data to the integral of the Gaussian beam profile, the function $P(x) = (P_0/2)(1 - \mathrm{erf}(\sqrt{2}(x - x_0)/w)$, where "erf" is the error function, x is the knife-edge position, *P(x)* is the measured power, P_0 is the power of the whole beam, x_0 is the x-position of the beam center, and w corresponds to the $1/e^2$ radius of the Gaussian beam [86].
In the measurements presented in this Section, a thin metal sheet (thickness of 100 µm) is used as a blade with translation steps of 500 µm. In the laser laboratory, a powermeter (Gentec Solo 2, equipped with a UP-19K detector) is used to measure the laser power. This

detector has an area big enough to detect the full unfocused laser beam. The power was attenuated by a factor of 1000 and guided to the optics hutch, where another powermeter (S130VC from Thorlab, with Silicon head) was used which is sensitive in the µW power range. Since area of this powermeter is small a fused-silica convex lens was used to focus the beam.

The first measurement point was located in the laser laboratory at about 70 cm after the laser exit and about 40 cm before the first telescope. The $1/e^2$ beam radii of $w_x = 3.8$ mm and $w_y = 4.8$ mm were measured in the horizontal and the vertical directions, respectively (Fig.4.1(a)). While the distance between the lenses of the telescope in the laser laboratory was set to about 5 cm, the second knife edge measurement was performed in the optics hutch 50 cm after the periscope (see Fig. 3.20). The beam radii of $w_x = 5.9$ mm and $w_y = 4.9$ mm were measured (Fig.4.1(b)), close to the values expected from the telescope calculations. At the same point in the optics hutch, the beam radii were measured when the first telescope in the laser laboratory was removed. In this case, the beam radii were $w_x = 8.2$ mm and $w_y = 7.2$ mm. Without using the first telescope, the beam radius is still smaller than the aperture radius between laser laboratory and the optics hutch, but it is close to the limit, and the chance of diffraction-induced power losses is very high in the case of small deviations of the beam path from the center of the apertures.

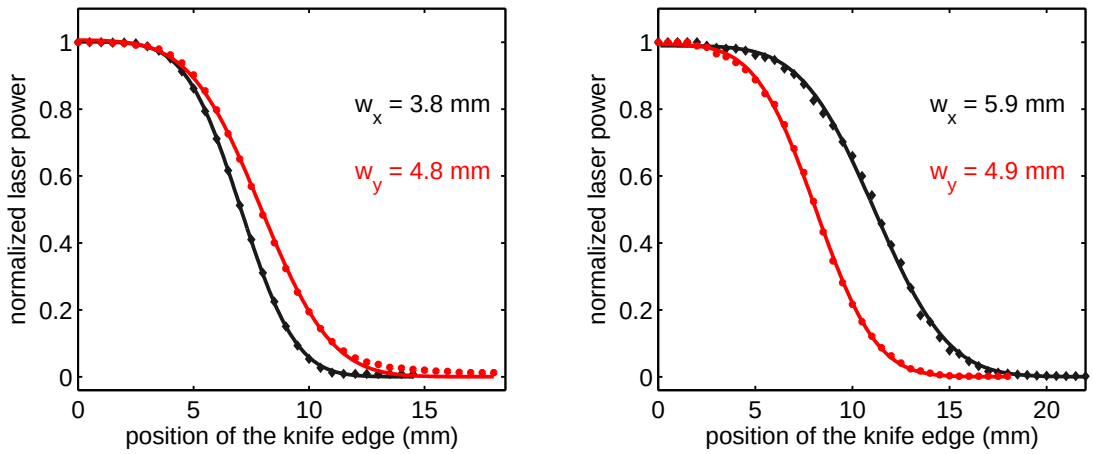

Figure 4.1: The pump-pulse beam radius measured using the knife-edge technique in the laser laboratory at about 70 cm after the laser exit (a) and one meter after entrance of the optics hutch (b) when the lens telescope in the laser laboratory was present.

The CCD camera images of the pump-pulse beam on the screens at several places along the beamline with and without the lens telescope are shown in Fig 4.2. The dimensions of these image are not calibrated, except for the one in the optics hutch, but these images show how the mirrors rotate the beam spot. This effect is particularly visible in the absence of the telescope. Since the beam spot in the hutch has a horizontal angle of about $\theta = 35°$ with

respect to the beam at the laser laboratory (see Fig 4.2), the measured beam radii are the size of the projected beam profile in the x and y directions $(w_\mathrm{x}, w_\mathrm{y})$. In order to calculate the major and minor radii of the elliptical beam $(w_\mathrm{a}, w_\mathrm{b})$, which are needed to estimate the divergence and M^2 value, the following transformation can be used

$$\begin{pmatrix} w_\mathrm{x}^2 \\ w_\mathrm{y}^2 \end{pmatrix} = M \begin{pmatrix} w_\mathrm{a}^2 \\ w_\mathrm{b}^2 \end{pmatrix} \; ; \quad M = \begin{pmatrix} \cos^2(\theta) & \sin^2(\theta) \\ \sin^2(\theta) & \cos^2(\theta) \end{pmatrix}, \tag{4.1}$$

which is derived by applying the rotation matrices for an ellipse to the initial profile [87]. Solving this equation and substituting the measured radii yields $w_\mathrm{a} = 11.7$ mm and $w_\mathrm{b} = 7.4$ mm in the absence of the lens telescope. To derive the divergence of the laser beam, w_a and w_b must be used instead of w_x and w_y.

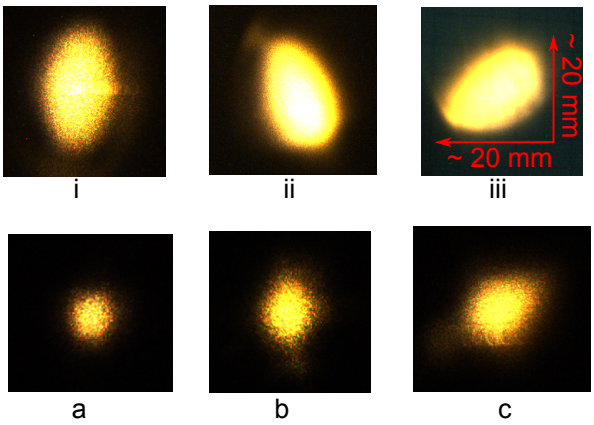

Figure 4.2: CCD camera images of the beam taken from diffuse screens along the pump-pulse beamline from the laser laboratory to the optics hutch with (a,b,c) and without (i,ii,iii) the lens telescope in laser laboratory.

Pump-pulse duration

The duration of the pump pulses was measured in the optics hutch by two methods, using a frequency-resolved optical gating (FROG) device and using an autocorrelator setup. The FROG device is a commercial system from Swamp Optics [100], which can measure and calculate the temporal and spectral intensity and phase profiles. The autocorrelator was built by splitting the laser beam into two parts and sending them through two different paths onto a SiC photodiode (No. 3 in Fig. 3.20). In Fig. 3.20, the beam shown in red can be delayed using a micrometer stage while the path of the beam in orange is fixed. An example of a temporal intensity profile measured using the FROG is shown in Fig. 4.3. The FWHM length of the pulse was about 70 fs.

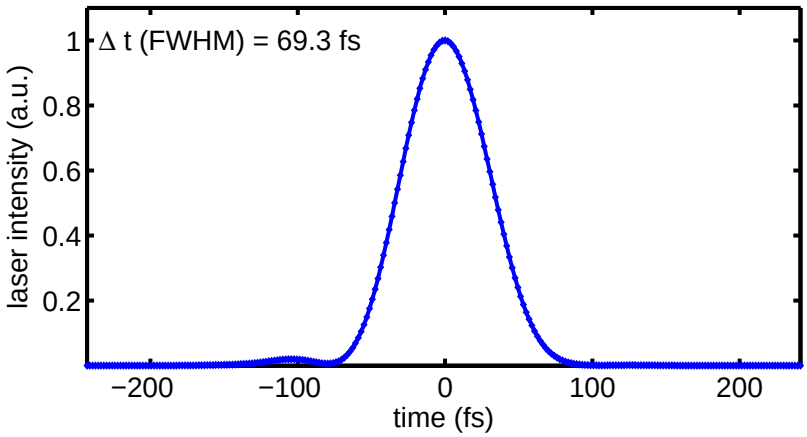

Figure 4.3: Pump-pulse profile in the optics hutch measured using FROG.

Positioning and pointing stability of the laser pulses

The beam-lock system described in Sec. 3.3.2 is used to stabilize the beam position and angle. Fig. 4.4 shows the position of the laser beam spot on the detectors of the feedback system recorded over 80 minutes when the feedback loop was closed (Fig. 4.4(a)) and open (Fig. 4.4(b)). In these figures, the x and y positions of the beam on the first detector are denoted by Bx and By, and on the second detector by Ax and Ay. The laser power measured by the detectors is shown in Fig. 4.5.

When the feedback loop is open, there is a long-term drift and a fast fluctuation in the beam position, angle and power. Generally, they are caused by drifts of the mirrors, air movement, thermal effects of the optical elements, and movement of the optical tables or vacuum chambers. These kind of drifts are effectively corrected by closing the feedback loop, after the beam is aligned perfectly on a sample (Fig. 4.4(a)). Moreover, there is a short-term drift in every 15 minutes which lasts for 5 minutes. The origin of this drift was not clear.

The mean values and standard deviations shown in Table 5 are derived from the measured positions and power on the detectors when the feedback is on. The position of the beam on both detectors and subsequently on a sample directly after the feedback system can be stabilized with an accuracy better than ± 26 µm.

Ax (µm)	Ay (µm)	Bx (µm)	By (µm)	P (mW)
0±24.7	0±25.5	0±23.9	0±23.2	35.2±0.37

Table 5: The mean value and the standard deviation of the positions and power measured by the detectors of the feedback over 80 minutes when the feedback loop was closed.

When the the feedback loop is open, the laser power measured on the feedback detectors decreases over time (Fig. 4.5), since the long-term drifts cause the beam to move away from

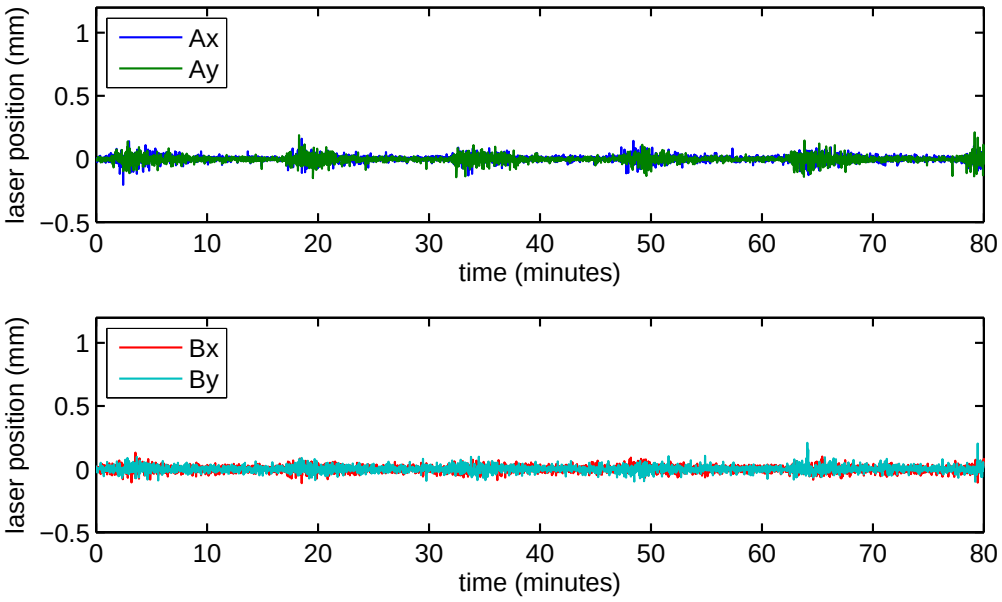

(a)

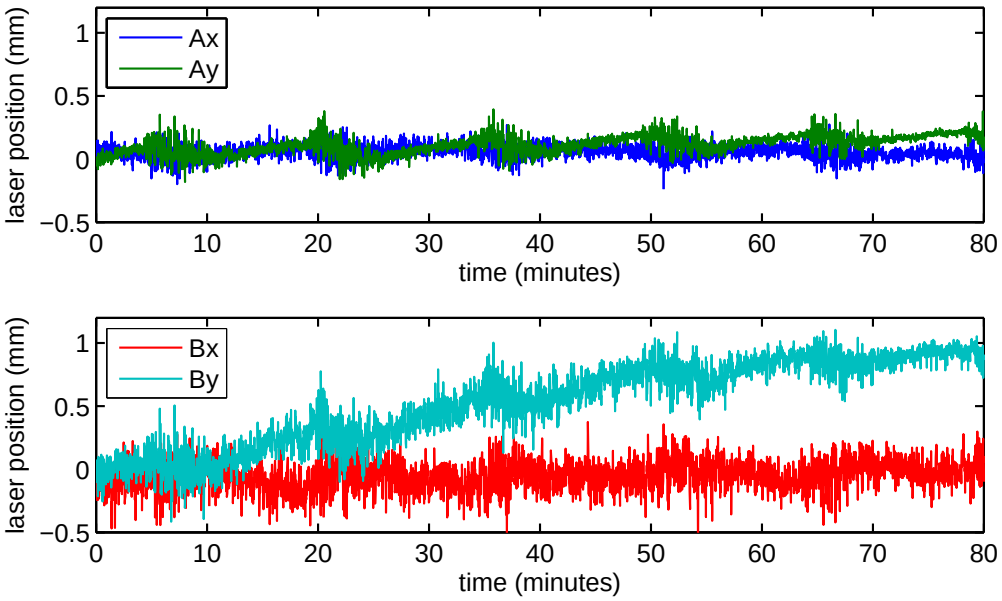

(b)

Figure 4.4: Position of the laser beam recorded for 80 minutes by the detectors of the feedback, when the feedback loop is closed (a) and open (b). When the feedback loop is closed, the beam is stabilized at the center of the detectors with an accuracy better than 26 µm (rms).

the center of the detectors.

When the feedback loop is closed, the power remains stable with an rms fluctuation of 1% (σ_P/P_{mean}), which is significantly less than that of the CHG pulses. The temporal stability of the CHG power has been investigated in [79]. A relative rms fluctuation of 5.4% was recorded for the power of the second harmonic CHG pulses with 400 nm seed wavelength.

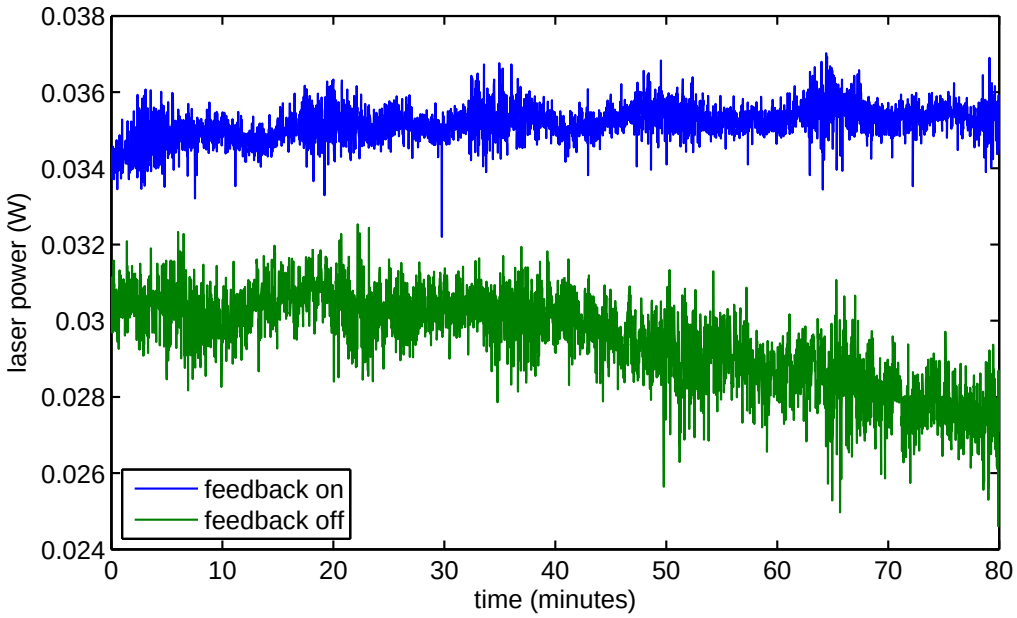

Figure 4.5: The laser power measured using the feedback detectors. When the feedback loop is open, the power decreases gradually as a result of the beam drift from the center of the detector. When the feedback loop is closed, the power remains stable with 1% fluctuation as a result of the continuous beam stabilization.

Laser intensity and beamline transmission

In order to verify the beamline transmission, the power of the laser beam in the optics hutch was measured over 16 minutes using a calibrated powermeter (S130VC from Thorlabs) with a sampling time of 0.1 second, while the feedback system was off (Fig. 4.6). The power decreases as a result of the beam drift from the center of the powermeter, confirming the feedback measurements. The laser power lost on the way from the laser laboratory to the optics hutch was less than 2%.

The intensity of the laser on the sample can be estimated for a given initial laser pulse energy. About 10% of the total Ti:sapphire laser power (about 0.8 W) is sent to the pump-pulse beamline. With the laser repetition rate of 1 kHz, this power is equivalent to an average pulse energy of 0.8 mJ. The main power loss (of about 8%) occurs due to the non-coated vacuum window in the entrance of BL 5. Considering an energy loss of about 10% in the

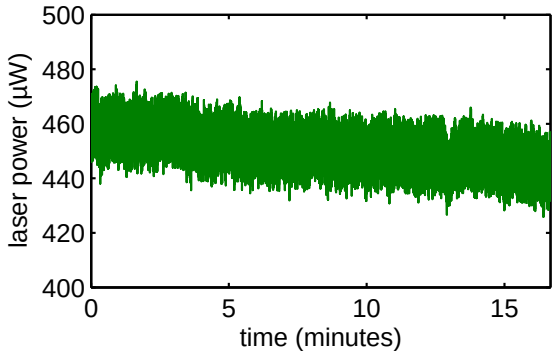

Figure 4.6: The laser power measured over 16 minutes in the optics hutch using a powermeter while the feedback was off.

whole beamline due to the mirrors, windows, air and lenses, the pulse energy delivered to the sample is about 0.72 mJ.

The energy fluence required for demagnetizing a ferromagnetic material was estimated to be about 1 to 10 mJ/cm^2 [93–96]. By focusing the pump-pulses (with pulse energy of 0.72 mJ) to a $1/e^2$ diameter of about 5 mm the energy fluence amounts to 3.7 mJ/cm^2.

Estimate of the *B* integral

As explained in Section 2.2.1, the B integral value along the beamline must be kept below 5 to avoid nonlinear effects. The dispersive elements used in the pump-pulse beamline are listed in Table 6.

Figure 4.7 shows the evolution of B integral calculated by using Eq. 2.51 and assuming two beams with average radii of $w = 5$ and $w = 10$ mm traveling through SiO_2. After passing through 38 mm fused silica, the B integral is less than 4. The B integral over 8 m air is 1.3 for $w = 5$ mm, and 0.3 for $w = 10$ mm. The total B integral remains below 5, small enough to avoid significant nonlinear distortions.

component	number	material	thickness (mm)	n_0	n_{2I} (m^2/W)
lens	3	fused silica (SiO_2)	5	1.453	2.4×10^{-20} [102]
window	3	quartz glass	6	1.453	2.4×10^{-20}
beamsplitter	1	fused silica	~ 5	1.453	2.4×10^{-20}
air	-	-	$\sim 8 \times 10^3$	1.000	4.0×10^{-23} [103]

Table 6: Dispersive material in the pump-pulse beamline. The notations n_0 and n_{2I} indicate, respectively, the linear and nonlinear components of the refractive index for a wavelength of 800 nm.

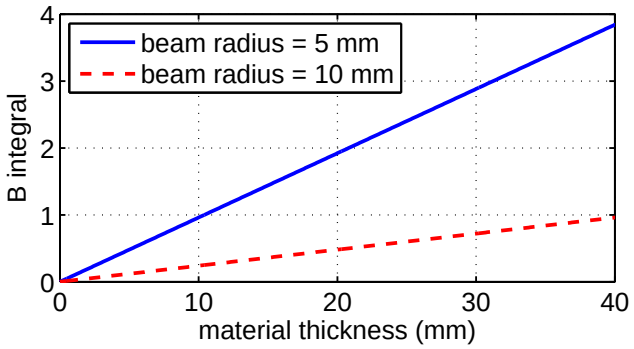

Figure 4.7: The B integral in SiO_2 as a function of the material thickness for two laser beam $1/e^2$ radii with a pulse energy of 0.8 mJ, a FWHM pulse duration of 40 fs, and a peak power of $\sim$ 20 GW.

Estimate of the group-delay dispersion (GDD) and pulse duration

Assuming an initial Gaussian pulse with a duration of 40 fs as measured by a FROG in the laser laboratory, the duration of pump pulses after passing through the whole pump-pulse beamline (with 38 mm fused silica and 8 m air) was calculated.

Using the *VChirp* software [104], a GDD value of 1550 fs^2 was calculated for 796 nm pump pulses. Inserting this value into Eq. 2.30, yields a pulse duration of 115 fs at the sample position.

4.1.1 Overlap of pump and probe pulses

Transverse (spatial) overlap

Both the pump pulses and the undulator radiation are focused on the sample and can be monitored by using a CCD camera and a lens (Fig. 4.8). The CHG radiation on the sample has a wavelength below 200 nm and is not visible for the camera, but it has the same path as the spontaneous emission from the radiator which can be tuned to a wavelength which is visible for camera. Moreover, it is possible to mount a fluorescent screen in place of the sample to observe the transverse overlap.
The diameter of a typical circular sample used in BL 5 is about 1 cm, and the rms size of the undulator radiation on the sample is about 1 to 2 mm in horizontal direction and about 100 µm in the vertical direction. Using a 5 mm pump-pulse beam diameter facilitates the overlap between the pump pulses and the CHG beam.

The pump-pulse size on the sample should be larger than the probe size in order to get uniform demagnetization, and it should be smaller than the sample size in order to get remagnetization induced by the remaining magnetic domains and also to get enough fluence.

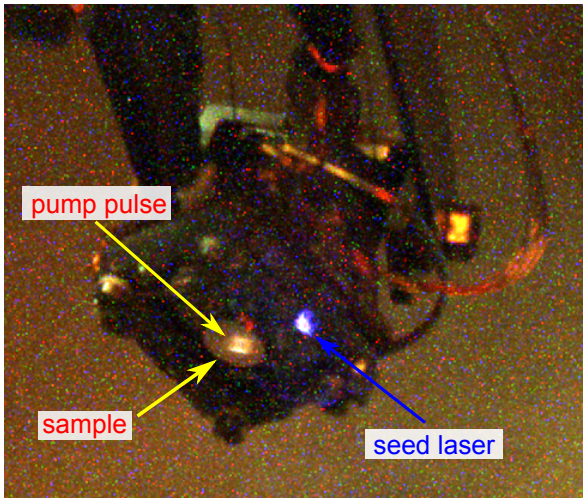

Figure 4.8: Image of the pump- and seed-laser beams on the sample. The seed laser is steered onto the sample holder for better visibility.

Longitudinal (temporal) overlap

As a first step to achieve temporal overlap of the pump and probe pulses, the seed laser has been used instead of the CHG pulses. The path length difference between the CHG and seed laser can be estimated. Photodiodes installed in BL 5 about one meter before the sample [89] have been used to measure the delay between pump- and seed- pulses. The arrangement of the photodiodes is shown in Fig. 4.9. Three photodiodes, one gold mesh and a fluorescent screen are mounted on a steel frame. They can be used for different purposes such

as detecting the CHG or spontaneous emission, measuring the radiation power, or adjusting the pump-probe temporal and spatial overlap. By moving the frame using a manual linear drive outside of the vacuum chamber, each of them can be placed in front of the beam.

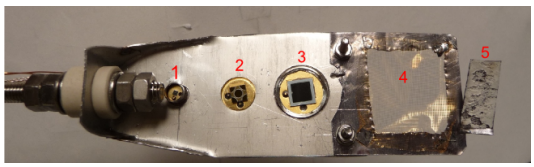

Figure 4.9: Photodiodes and gold-mesh unit installed in the VUV beamline. The frame comprises a SiC visible-blind photodiode (1), a silicon avalanche photodiode (2), a GaAsP photodiode (Hamamatsu G1127) (3), a gold-mesh (4), and a fluorescent screen (5).

To roughly determine the delay between the pump- and seed- pulses, the avalanche photodiode (A1900, with a 2×2 mm^2 silicon sensor and 2 ns rise time) was used. Both beams were focused on the photodiode and good spatial overlap was achieved by monitoring the beams first on the fluorescent screen and then on the photodiode surface with a CCD camera mounted on the viewport of the photodiode unit. The photodiode signal was amplified with a low-noise broadband amplifier (Kuhne LNA BB 0515 B-N) and a 2 GHz high-speed amplifier (Femto HSA-X-2-20) and observed using an oscilloscope (Fig. 4.10). An initial time difference of 6.9 ns corresponding to a path difference of 2.07 m was measured and corrected by rearranging and adding mirrors, thus increasing the path length of the pump pulses.

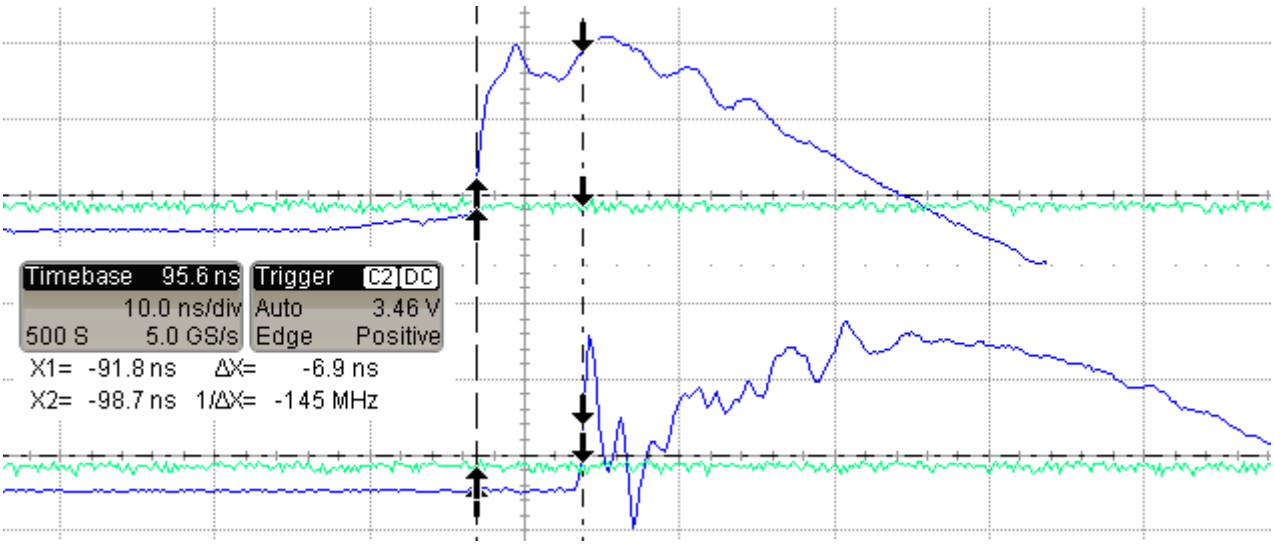

Figure 4.10: Oscilloscope traces: photodiode signal from the seed laser while the pump pulses are blocked (bottom). Signal from both pump and seed laser (top). In this example, there is a timing mismatch of 6.9 ns between the two pulses.

For further temporal alignment, a Silicon Carbide (SiC) visible-blind photodiode (SG01L-18 from sglux [105]) with an active area of 1 mm^2 was used. In order to find the "zero delay" between pump and seed pulses, the arrival time of the pump pulses was varied by using the delay stage and the 2-photon-induced photocurrent in the SiC photodiode was measured. As

long as there is no temporal overlap between the two pulses, the signal is constant due to multi-photon absorption from either the seed or the pump beam, but when the pulses have temporal overlap, the signal increases (Fig. 4.11).

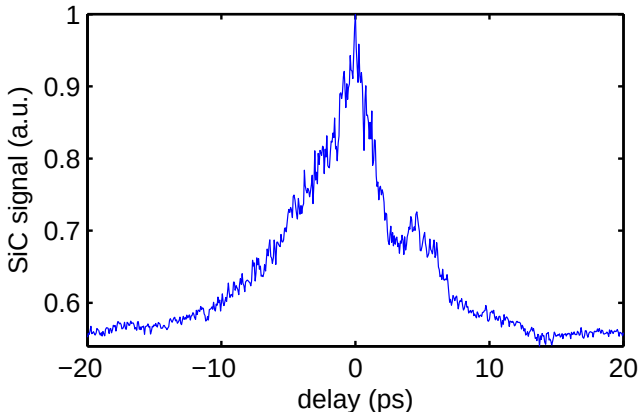

Figure 4.11: Two-photon-induced photocurrent in the SiC-photodiode due to cross-correlation between pump and seed pulses.

The FWHM width of the cross-correlation signal is about 7 ps, indicating a pulse duration of about $\Delta t = 7\ \text{ps}/\sqrt{2} = 4.9$ ps. The main reason for such a long duration is the grating of the monochromator in BL 5. The seed-laser pulses are temporally lengthened due to the dispersion in the monochromator by

$$\Delta t = n\lambda/c \tag{4.2}$$

with n being the total number of the grating lines hit by the beam. In order to achieve a sub-ps temporal resolution, a grating with a lower line density would be preferable. However, by decreasing the line density, the incident angle of the beam on the grating must also be decreased, which in turn diminishes the effect. The grating presently used in the monochromator of the BL 5 has 300 lines per millimeter.
Another way to decrease the number of the grating lines hit by the beam n is to decrease the beam size either by focusing it or by closing the apertures; the latter is at the expense of beam intensity. In this way, the probe pulse duration can be reduced to a few 100 fs.
Furthermore, the temporal broadening of the CHG pulses at lower wavelengths will be smaller.

With a beam diameter of about 5 mm on the grating and $\lambda = 400$ nm, the expected pulse lengthening is about $\Delta t = 4.9$ ps in agreement with the measurement. The origin of the side peak is probably a reflection of the beam from the walls of the vacuum pipe.

The effect of non-normal incident angle of the pump-pulse beam is shown in Fig. 4.12. Assuming a probe beam size of 1 mm, the time difference due to an angle of 1° between the two

beams results in a time difference of approximately $\Delta t = (1\ \text{mm} \times \sin(1^o))/(3 \times 10^8 \text{m/s}) = 58$ fs, which is comparable to the pulse length.

The incident angle of the undulator radiation on the sample in BL 5 is about $\theta = (45°,0°)$ in (x,y) direction. The incident angle of the pump beam in horizontal x direction is the same. In BL 5, the sample is at a height of about 210 cm above the floor, and the last mirror of the pump-pulse beamline is at a height of 204 cm at the distance of 280 cm from the sample. This results in a small incident angle of θ in y direction corresponding to a time difference of $\Delta t_1 = 7.1$ fs (for a vertical probe size of $\Delta y = 100$ µm), which is smaller than the pulse length and will not affect the temporal resolution of the pump-probe experiment significantly.

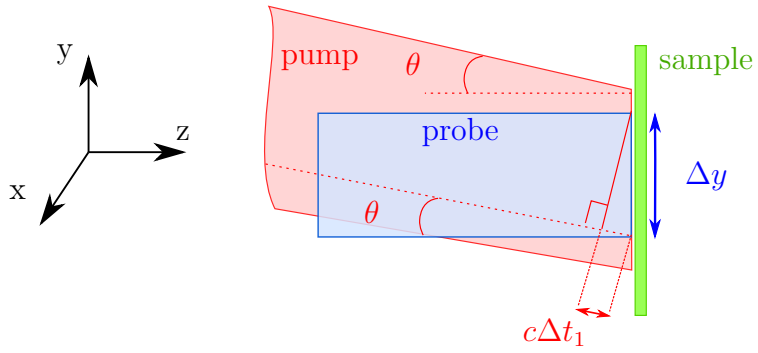

Figure 4.12: Sketch of the pump and probe beams on the sample with different incident angles causing time differences.

4.2 Detection of CHG-induced photoelectrons

As an important step towards user applications, CHG radiation was detected in BL 5. This beamline is presently the only way to detect the CHG pulses below 200 nm, since an evacuated beamline is required.

Only small modifications were necessary to switch from the standard spin- and angular-resolved photoelectron spectroscopy (PES) experiments to time-resolved PES. For this purpose, the timing capability of the delay-line detector (DLD) was enabled (Section 3.1.1). The software and the hardware of the delay-line detector was modified by the manufacturer *Surface Concept GmbH* [107]. A new time-to-digital-converter (TDC) unit with large buffer was installed to be compatible with the 1 kHz trigger, while the previous TDC unit could operate only with triggers faster than 10 kHz.

Examples of time histograms of CHG-induced photoelctrons from a gold target detected by the DLD at $\lambda = 199$ nm and $\lambda = 133$ nm are shown in Fig. 4.13. For these measurements, the c_{ff} value was set to 2.5, the MCP voltage was 1800 V, and the pass energy of the analyzer was 20 eV. For higher photon energies, the c_{ff} is usually set to 1.5. The exposure time was one second and the number of the accumulated exposures was 44 and 66, respectively, for the graphs shown in Figs. 4.13(a) and 4.13(b). At low photon energies (below 10.8 eV), a 9-V battery was applied to the sample for further acceleration of the photoelectrons.

In these measurements, due to the limitation of the previous TDC unit, the trigger rate of the detector was 10 kHz synchronized with the laser pulse. Therefore, the spontaneous emission is accumulated 10 times more often than the CHG radiation. The time resolution is not limited by the DLD, but by the temporal broadening due to different photoelectron trajectories inside the spectrometer (the hemispherical analyzer), which results in an accumulated pulse width of about 40 ns (FWHM) for CHG and about 50 ns for SE. This is sufficient to resolve the CHG signal in successive single-bunch turns (Fig. 4.15) and also to perform CHG experiments with a hybrid filling pattern with a single bunch in a 100-ns gap. The wavelengths of the CHG radiation achieved at DELTA and the corresponding photon energies and K values are summarized in Table 7.

The K value of the undulator was tuned to the maximum CHG signal (K_{exp}) which is slightly different from the theoretical K value (K_{th}) calculated using the undulator equation (Eq. 2.15) (with an electron energy of 1.485 GeV) due to missing calibration at these wavelengths and possible hysteresis. The empirical relation between the undulator current and K value is $I \sim 38.6$ A $\cdot K$.

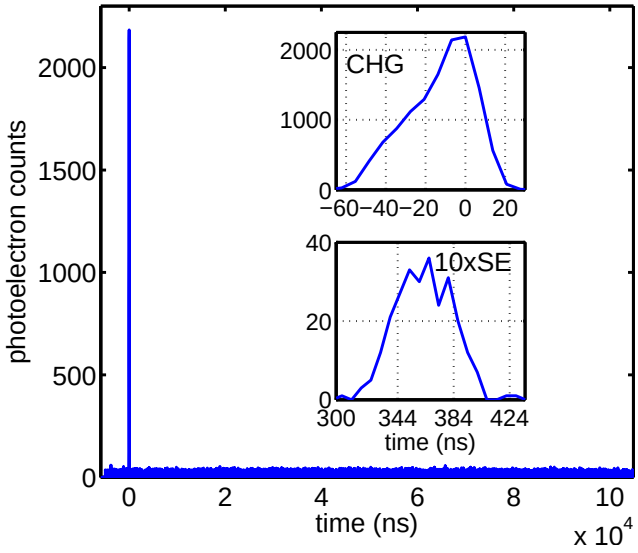

(a)

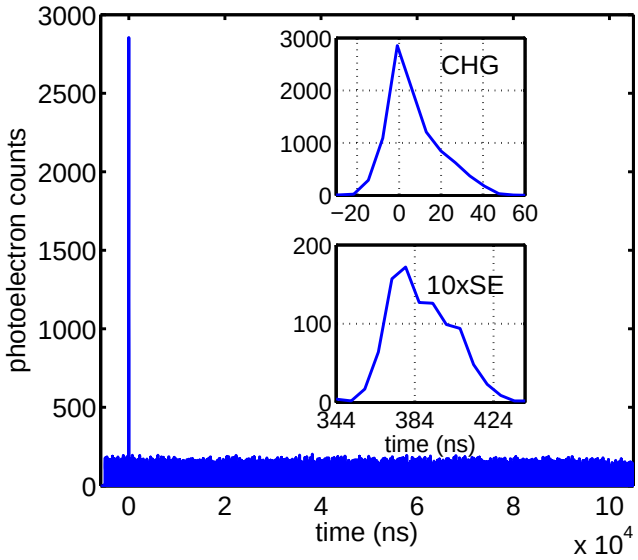

(b)

Figure 4.13: Histogram of the photoelectron (PE) signal from a gold target detected using the DLD at λ =199 nm (a) and λ =133 nm (b). The insets show the PE signal from CHG pulses (at $t = 0$) and from the adjacent spontaneous emission (at $t = 384$ ns).

The energy of the monochromator was tuned to the highest possible CHG signal (E_{exp}), slightly different from the calculated photon energy for the expected wavelength ($E_{\mathrm{th}} = hc/\lambda$). This discrepancy is due to missing calibration of the monochromator at low photon energies of the monochromator.

Figure 4.14 shows typical 2D images from the DLD, here shown for the 5$^{\mathrm{th}}$ harmonic of 800 nm at a monochromator energy of 7.9 eV and a CHG-to-SE ratio of about 3 (see

Table 7: Wavelengths of CHG radiation achieved at DELTA, corresponding photon energies at different harmonic numbers n, undulator K values, and the c_{ff} values used in operating the monochromator. The discrepancies between the theoretical and experimental values are due to missing calibration at these photon energies.

λ_{seed}	n	λ (nm)	E_{th} (eV)	E_{exp}	K_{th}	K_{exp}	c_{ff}
796 nm	2	398.0	3.12	3.10	7.20	7.16	-
	3	265.3	4.68	-	5.82	5.78	-
	4	199.0	6.24	6.25	4.99	4.86	2.5
	5	159.2	7.80	7.90	4.42	4.48	2.5
	6	132.7	9.36	9.35	3.99	3.86	2.5
	7	113.7	10.92	11.05	3.66	3.62	1.5
398 nm	4	99.5	12.49	12.6	3.38	3.36	1.5
	5	79.6	15.60	15.8	2.95	2.94	1.5

Fig 4.17(a)). The y axis represents the momentum of the photoelectrons and the x axis the energy. The accumulated counts in any temporal interval can be saved in a separate file.

The three pictures in Fig 4.14 show the accumulated counts from 124 SE pulses, one CHG, and one SE pulse.

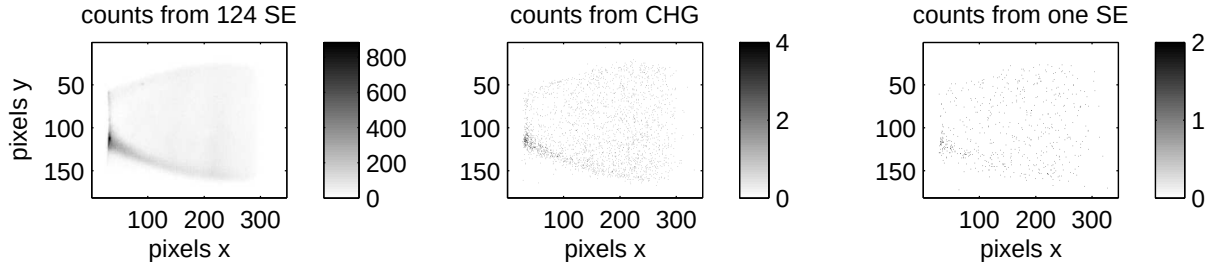

Figure 4.14: 2D images from the DLD showing the photoelectron hits at different points of the MCP for 5^{th} harmonic of the 800 nm seed laser. The gray-scales show the accumulated counts of the photoelectrons from 124 SE pulses, one CHG, and one SE pulse.

While seeding with 400 nm laser wavelength, the harmonics from 2 to 5 were detected. Figure 4.15 shows the photoelectron counts from a gold target for the 2^{nd} to 5^{th} harmonics. Since the U250 is tuned to relatively high undulator parameters ($2.8 < \mathrm{K} < 7.2$), the incoherent radiation not only includes the fundamental wavelength, but also strong harmonics, which can pass the plane grating monochromator (PGM) due to high-order diffraction.

To exclude the higher harmonics, a Lithium Fluoride (LiF) filter was used. Depending on its thickness, the transmission range of LiF is typically from 105 nm (11.8 eV) to 9 µm [106] depending on its thickness. The ratio between the total counts from a CHG signal to the spontaneous signal (CHG-to-SE ratio) is 370 for the second harmonic and 90 for the third harmonic.

To detect the 4th and 5th harmonic of the 400 nm seed laser, the LiF filter had to be removed. Therefore, estimating the true CHG-to-SE ratio at these wavelengths is not straightforward due to the huge background of photoelectrons generated by the high harmonics of the undulators, especially the modulator. The observed CHG to SE ratios for the 4th and 5th harmonics including higher-harmonic background, shown in Fig. 4.15(b) are about 0.3 and 0.2, respectively.

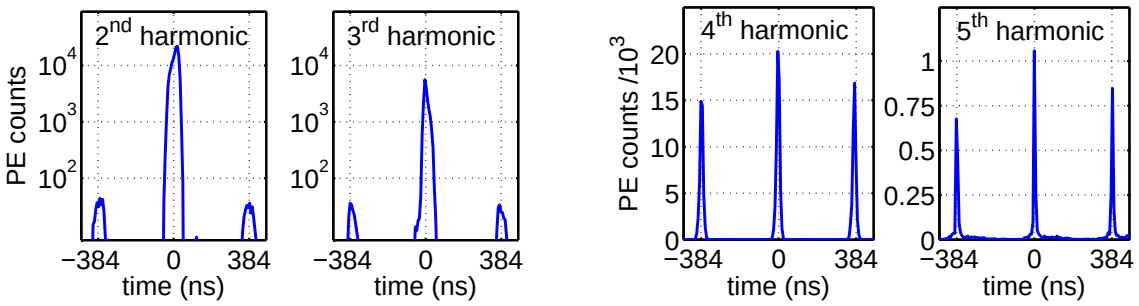

Figure 4.15: a) CHG (at $t = 0$) and spontaneous emission (at t = ±384 ns) signal from photoelectrons detected by the DLD at $\lambda = 199$ nm (left) and $\lambda = 133$ nm (right). Note that the scale of the counts is logarithmic. b) Photoelectron counts form CHG and SE pulses at $\lambda = 100$ nm (left) and $\lambda = 80$ nm (right), here the scale is linear.

4.2.1 Spectrum of CHG measured at BL 5

The spectrum of CHG radiation can be measured in BL 5 by tuning the monochromator to different photon energies. While seeding with 400 nm laser pulses, the CHG spectra were detected at the second (Fig. 4.16(a) and Fig. 4.16(b)) and third (Fig. 4.16(c)) harmonic. The results at 200 nm are consistent with those from other measurements using a Czerny-Turner spectrometer equipped with an avalanche photodiode (APD) and a CCD-array spectrometer, which both give a Gaussian-shaped spectrum with a FWHM width of about 3.3 nm ($\Delta\lambda/\lambda = 1.6\%$). The spectrum in Fig. 4.16(b) is measured at 200 nm with a slightly smaller PGM exit slit (600 µm), yielding a smaller width of 0.072 eV or 3.0 nm ($\Delta\lambda/\lambda = 1.5\%$).

Assuming a pulse duration of 50 fs, the time-bandwidth product $\Delta t \cdot \Delta\nu = 1.1$ is about a factor of two larger than the Fourier limit. At 133 nm, the FWHM width of the spectrum is about 0.123 eV ($\Delta\lambda = 1.63$ nm, $\Delta\lambda/\lambda = 1.2\%$) and $\Delta t \cdot \Delta\nu = 1.3$, with $\Delta t = 50$ fs. The two last spectra in Fig. 4.16 are measured at different conditions at which the ratios were reduced mainly due to a reduction in laser power, degraded efficiency of the SHG unit converting the 800 nm laser pulses to 400 nm, and degraded laser transmission from the laser system to the undulator.

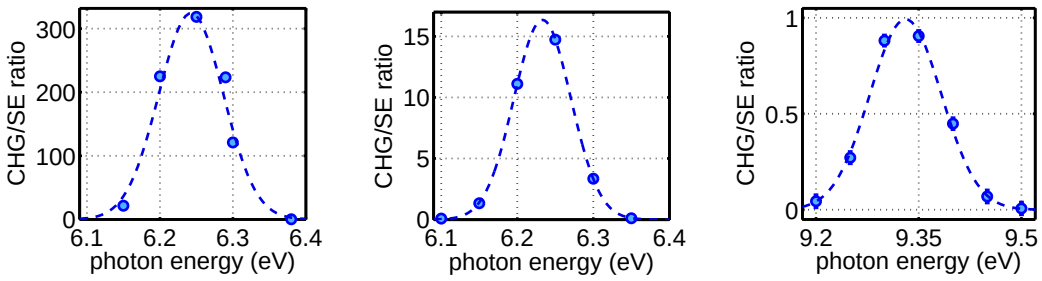

(a) $\lambda_{\mathrm{CHG}} = 200$ nm (b) $\lambda_{\mathrm{CHG}} = 200$ nm (c) $\lambda_{\mathrm{CHG}} = 133$ nm

Figure 4.16: CHG spectra at the second harmonic with FWHM of 0.104 eV (3.31 nm) (a), and third harmonic with FWHM of 0.123 eV (1.63 nm)(c), obtained using photoelectrons under variation of the PGM wavelength. The curve in plot (b) is measured at 200 nm with a smaller PGM exit slit (600 µm), yielding a smaller width of 0.088 eV (3.0 nm). The dashed lines are Gaussian fits.

While seeding with 800 nm, the 5^{th} to 7^{th} CHG harmonics were detected at BL 5. Example spectra are shown in Fig. 4.17, measured behind the LiF filter. The transmission of LiF at $\lambda = 112$ nm ($E_{\mathrm{ph}} = 11.05$ eV) is about 45% [106], reducing the absolute intensity at the 7^{th} harmonic. The unexpected decrease in the spectrum around 9.4 eV might be related to a temporary misalignment of the laser-electron overlap. The error bars of the spectral data in this Section represent the statistical errors, assuming that the photoelectron counts follow the Poisson distribution. However, in some of these plots the error bars are too small to be seen.

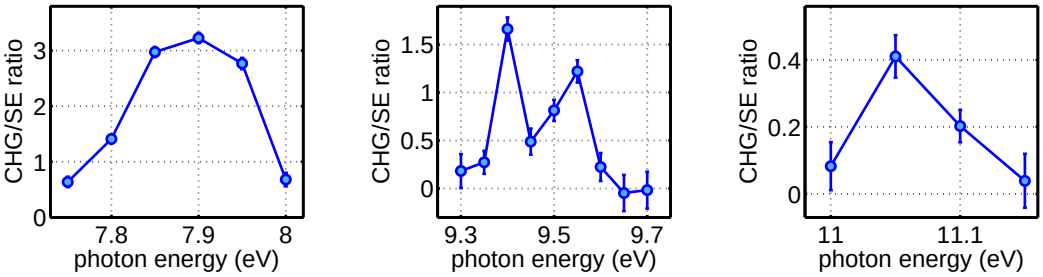

(a) $\lambda_{\mathrm{CHG}} = 160$ nm (b) $\lambda_{\mathrm{CHG}} = 133$ nm (c) $\lambda_{\mathrm{CHG}} = 114$ nm

Figure 4.17: CHG spectra at the $5^{\mathrm{th}}, 6^{\mathrm{th}}$, and 7^{th} harmonic of 800 nm (a,b,c) measured at BL5.

4.2.2 CHG signal versus chicane strength

The CHG-to-SE ratio was measured at BL 5 under variation of the chicane strength r_{56}. The results are shown in Fig. 4.18. As expected, the CHG-to-SE ratio increases until reaching the optimum chicane strength and then decreases due to the over-bunching of the electrons.

Fitting the data in Fig. 4.18 by using the Eq. 2.99 yields the energy modulation $\Delta E/E$, assuming a fixed relative energy spread of $\sigma_E/E = 9.8 \times 10^{-4}$. The measured data are in good

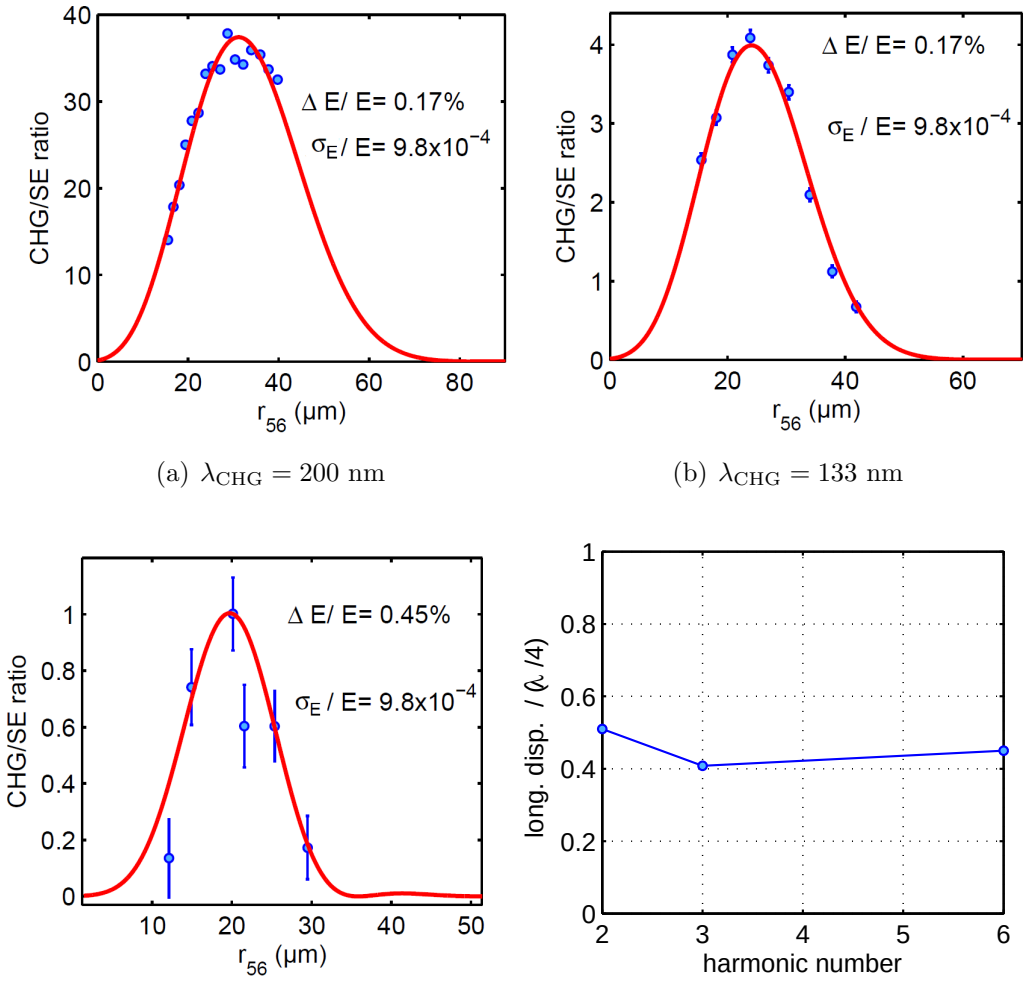

(a) $\lambda_{\mathrm{CHG}} = 200$ nm (b) $\lambda_{\mathrm{CHG}} = 133$ nm

(c) $\lambda_{\mathrm{CHG}} = 133$ nm (d)

Figure 4.18: CHG versus chicane current at the 2nd (a) and 3rd (b) harmonic of the 400 nm seed laser, and the 6th (c) harmonic of 800 nm obtained using photoelectrons. The longitudinal displacement of the electrons ($r_{56} \times (\Delta E/E)$ divided by one quarter of the seed-laser wavelength ($\lambda_L/4$) calculated for these three harmonics is shown in (d). The red curves show the fits to the respective Bessel functions.

agreement with the theory. While seeding with 800 nm wavelength, the energy modulation is 0.45%, which is about 2.65 times higher than the energy modulation while seeding with 400 nm (0.17%). The reasons are the higher laser pulse energy at 800 nm, the chirp introduced after the SHG unit, and the not yet optimized telescope for the 400 nm laser beam. The maximum CHG-to-SE ratio was observed at an r_{56} value of about 30 µm at the 2nd harmonic, which is in agreement with the typical values derived by measurements using the APD in the diagnostic at hutch BL 4 (see Chapter 5). At the 3rd and 6th harmonics (133 nm), the maximum CHG ratio was observed at r_{56} values of about 24 µm and 20 µm, respectively.

Figure 4.18(d) shows the plot of the longitudinal displacement of the electrons divided by one quarter of the seed-laser wavelength $r_{56} \times (\Delta E/E)/(\lambda_L/4)$, calculated for three harmonics,

which should be approximately equal to one. The large discrepancies are due to relatively high energy spread which was verified by simulations.

4.2.3 Photoelectron spectroscopy using CHG

The first proof-of-principle PES experiment using CHG radiation at DELTA was realized by detecting the surface state (the electronic state at the surface of material) of a Cu(111) sample shown in Fig. 4.19 [108]. Using 9.35-eV CHG radiation, a parabolic surface state was recorded with a kinetic energy of the photoelectrons between 4.5 eV and 4.7 eV.

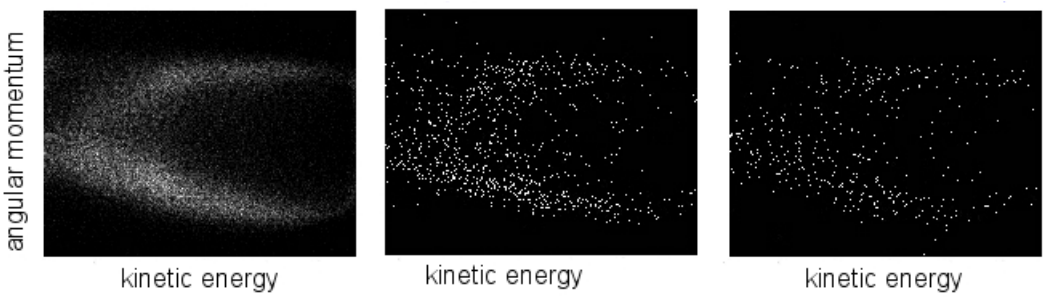

Figure 4.19: Images from the DLD showing the surface state of Cu(111): photoelectrons from 124 spontaneous synchrotron radiation pulses (left), from one CHG pulse (center) and from one spontaneous synchrotron radiation pulse (right).

After detecting CHG radiation at BL 5, bringing the pump pulses on the sample and achieving the zero-delay between the pump and seed pulses, the preparations for pump-probe photoemission experiments are nearly completed. The first experiment will be performed on the magnetic system Co/Cu [97]. The goal is to use the magnetic linear dichroism (MLD) effect in order to study the demagnetization dynamics in this thin-film system. A similar measurement has been reported in [68] using x-ray magnetic circular dichroism (XMCD) with 850-eV pulses from the BESSY femtoslicing source.

One of the challenges to reach this goal is to increase the photon energy and the intensity of the CHG pulses. A high photon energy will increase in turn the kinetic energies of the photoelectrons and the temporal resolution of the hemispherical analyzer (see Eq. 3.1). Both, the higher intensity and photon energy, will also increase the count rate and hence the resolution of the pump-probe experiment.

Furthermore, since the BL 5 and its experimental end station were not designed to be operated at the energy range of CHG pulses (6-20 eV), further modifications as well as calibrations, primarily of the monochromator, are recommended.

5 Characterization of CHG Radiation at DELTA

In this Chapter, a comprehensive time-, space- and frequency-domain characterization of the CHG radiation is presented. The theoretical models presented in Chapter 2 are used to fit the data, leading to further insight into the CHG process and optimizing it for user experiments. The characterized parameters encompass the angular-spectral distribution of the CHG and spontaneous emission, the dependence of the central wavelength of CHG on different parameters, estimate of the energy modulation, estimate of the CHG pulse energy, and the coherence properties of CHG and SE (spontaneous emission, i.e. incoherent synchrotron radiation). Additional characterization and information about the DELTA short-pulse facility, including the THz radiation and the EEHG scheme, can be found in [19–28, 79].

At the end of the year 2012, the chicane within the undulator U250 was modified by rewiring its poles (Section 5.3). The measurements presented until Section 5.3 were conducted before the chicane modification, and the rest with the modified chicane, the higher r_{56} values of which have lead to a better microbunching, coherence and intensity.

The types and the key parameters of the detectors used to conduct the measurements reported in this thesis are listed in the following:

- A CCD spectrometer (Maya2000 Pro from Ocean Optics) was used to measure the spectrum of the laser and SE. This spectrometer has an integration time of 7.2 ms to 5 s, which is not suitable to resolve the CHG pulses with 1 kHz repetition rate among the 2.6-MHz SE pulses. Nevertheless, the 400-nm CHG radiation spectrum could also be measured using this spectrometer, when the peak intensity of a single CHG pulse was comparable to the peak intensity of 2600 pulses of SE.

- In order to record the spectrum of CHG pulses without SE background from more than one pulse, a wavelength-scanning Czerny-Turner spectrometer (Acton Research SP-275) was used with a photomultiplier (PMT) or an avalanche photodiode (APD; S9073 from Hamamatsu) and a 2-GHz sampling oscilloscope.

- A powermeter equipped with a silicon photodiode (S130VC from Thorlabs) was used to measure the power of the laser and SE pulses within a power range of 500 pW to 500 mW and a wavelength range of 200 nm to 1100 nm.

- A powermeter (Gentec Solo 2) equipped with a thermal detector (UP-19K) was used to measure the laser power above $\sim$ 30 mW.

- A fast-gated intensified CCD camera (ICCD) was used to record the interference patterns of CHG, described extensively in Section 5.6.

5.1 Angular distribution

The angular distribution of CHG radiation was measured using the Czerny-Turner spectrometer with a PMT, and the angular distribution of the spontaneous emission was measured using the CCD spectrometer in both horizontal and vertical directions at a distance of about 10 meters away from the radiator.
The radiation spectra were recorded by sending the unfocosed beam to the spectrometer while varying the angle of the mirror before the spectrometer. The angle was measured using a He-Ne laser beam being reflected from the same mirror onto a screen.
The spectra shown in figures 5.1 and 5.3 are interpolated linearly between the 7-20 measured angles.

The SE was measured while only the radiator section of the U250 was on and tuned to a wavelength of 200 nm. When observing the spectra from a point away from the radiation axis, the central wavelength of the SE is shifted towards longer wavelengths (Eq. 2.15), while the central wavelength of the CHG radiation is not affected. The central CHG wavelength is determined by laser wavelength (see Section 5.2) and its spectrum is the Fourier transform of the electron density distribution, yielding a narrow-band spectrum due to sharp peaks at microbunches. The microbunching acts like a narrow-band amplifier on the spectrum of the undulator spontaneous emission.

The measured width of the 200-nm CHG radiation profile was about 6.5 mm (FWHM) in the horizontal direction and 8.5 mm (FWHM) in the vertical direction (Fig. 5.2), consistent with the measurements using the ICCD camera (Section 5.6).

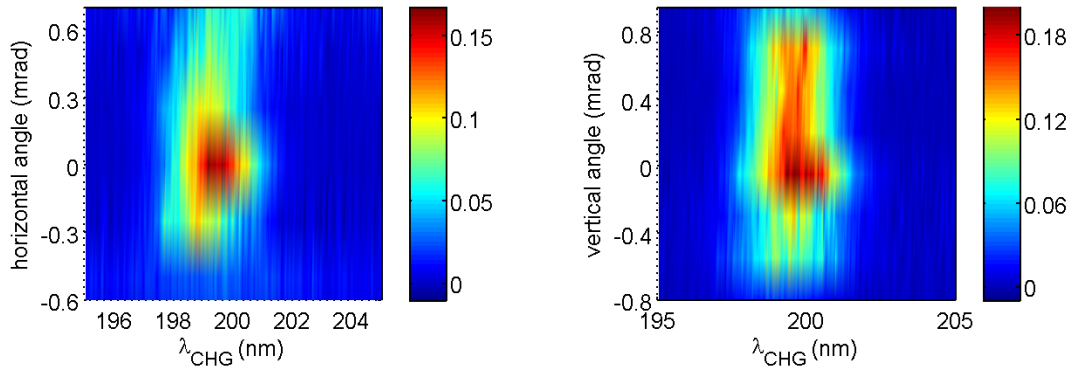

(a) (b)

Figure 5.1: CHG spectra under variation of horizontal (a) and vertical (b) position; measured at a distance of about 10 meters away from the radiator.

The parabola-shaped red-shifts can be seen clearly in the SE spectra distribution. By shifting the angular position from the beam axis to $\theta = \pm 0.6$ mrad, the central wavelength is

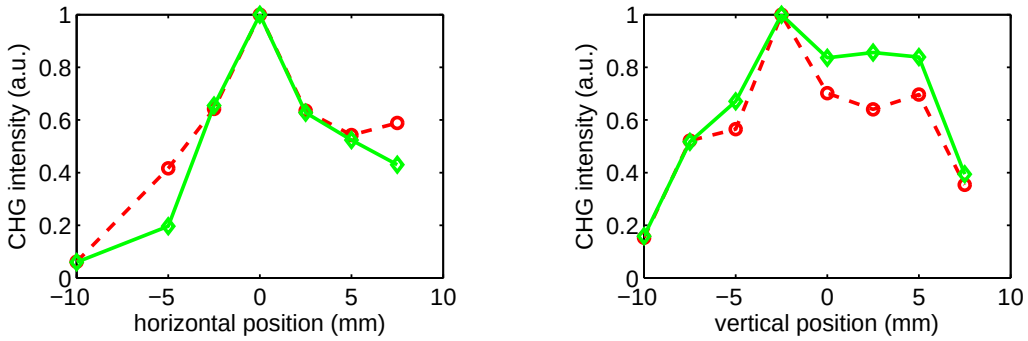

(a) (b)

Figure 5.2: CHG intensity under variation of horizontal (a) and vertical (b) position; the red curve shows the intensity averaged over the wavelength range of 195 nm to 205 nm, and the green curve shows the intensity at the central wavelength.

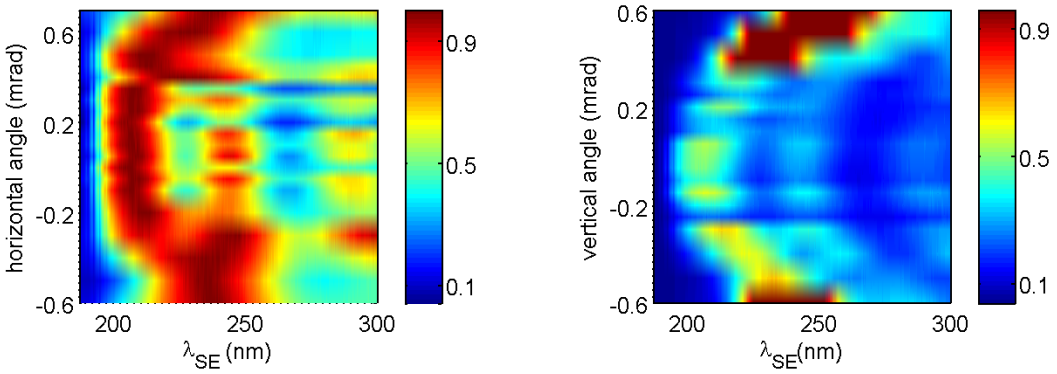

(a) (b)

Figure 5.3: SE spectra under variation of horizontal (a) and vertical (b) position; measured at a distance of about 10 meters away from the radiator.

shifted from 200 nm to about 245 nm. This value fits very well to the theoretical off-axis resonance wavelength. With $\lambda_u = 250$ mm, Eq. 2.15 yields $\Delta\lambda_0(\theta) = \lambda_u\theta^2/2 = 45$ nm.

5.2 Spectral distribution

The central wavelength of CHG radiation was studied while detuning the optical klystron and the laser wavelength. For this purpose, the spectrum of CHG radiation was measured under variation of several parameters, namely the K value of the radiator and modulator, the r_{56} value of the chicane and the spectrum of the laser pulses. The error in measuring the CHG wavelength is about $\pm$ 0.25 nm.

The K value of the modulator was varied from 6.9 to 7.5, i.e. its resonance wavelength was varied from 366 nm to 435 nm (Fig. 5.4). The wavelength of the seed laser was 400 nm, and the radiator was tuned to its second harmonic. While varying the undulator wavelength by 69 nm, the central CHG wavelength varied by only (1.3 ± 0.25) nm .
This small change is due to large bandwidth of the undulator radiation (about $\lambda_{\mathrm{res}}/N_{\mathrm{u}}$) and finite bandwidth of the laser light (about 4.2 nm). The bandwidth of the modulator line is

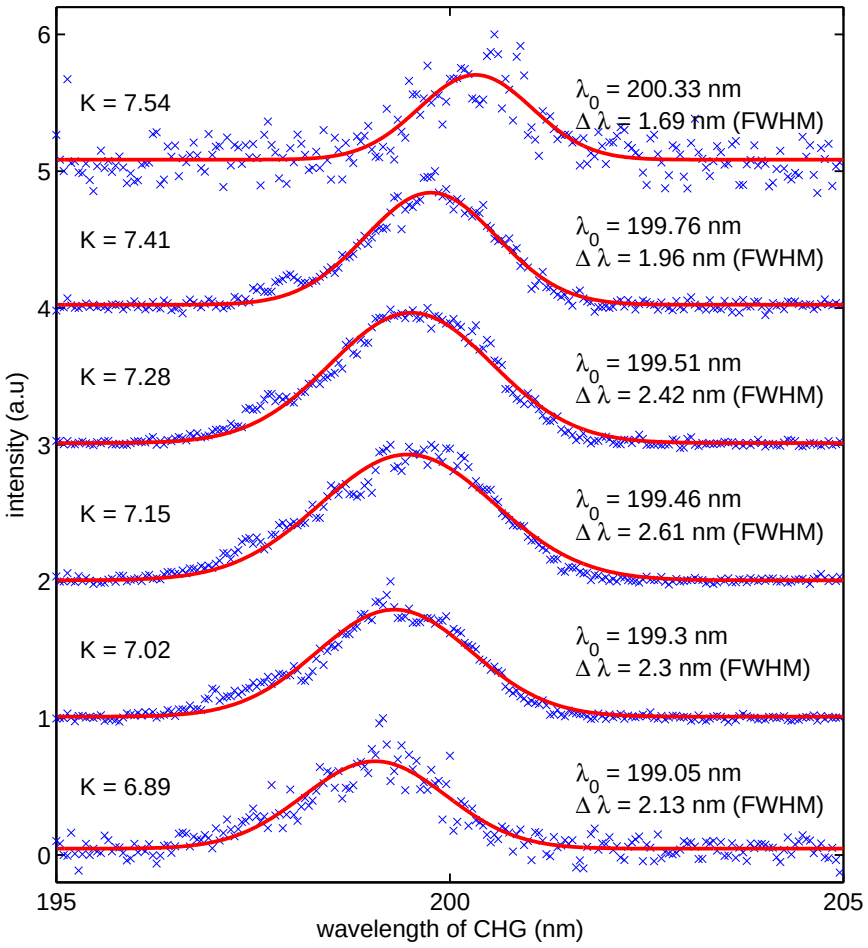

Figure 5.4: CHG spectra under variation of the K value of the modulator.

large enough to cover the laser line over the scanned range, enabling resonant interaction with the laser. The relative CHG intensity increases when approaching the optimum K value, as excepted.

Furthermore, the K value of the radiator was varied from 4.7 to 5.3 (resonance wavelengths of 179 nm to 226 nm) while the modulator was tuned to 400 nm (Fig. 5.5). The change in the central wavelength of the CHG remains within the measurement error.

The optimum chicane strength depends on the energy modulation and laser wavelength given by the relation 2.100. The spectrum is given by the Fourier transform of the longitudinal distribution of the electrons, which is determined by the chicane strength as well as the laser wavelength and pulse energy. While fixing the wavelength of the radiator and modulator to 200 nm and 400 nm, respectively, the chicane strength was varied (Fig. 5.6). The CHG wavelength and bandwidth stays almost unchanged. By increasing the r_{56} value of the chicane,

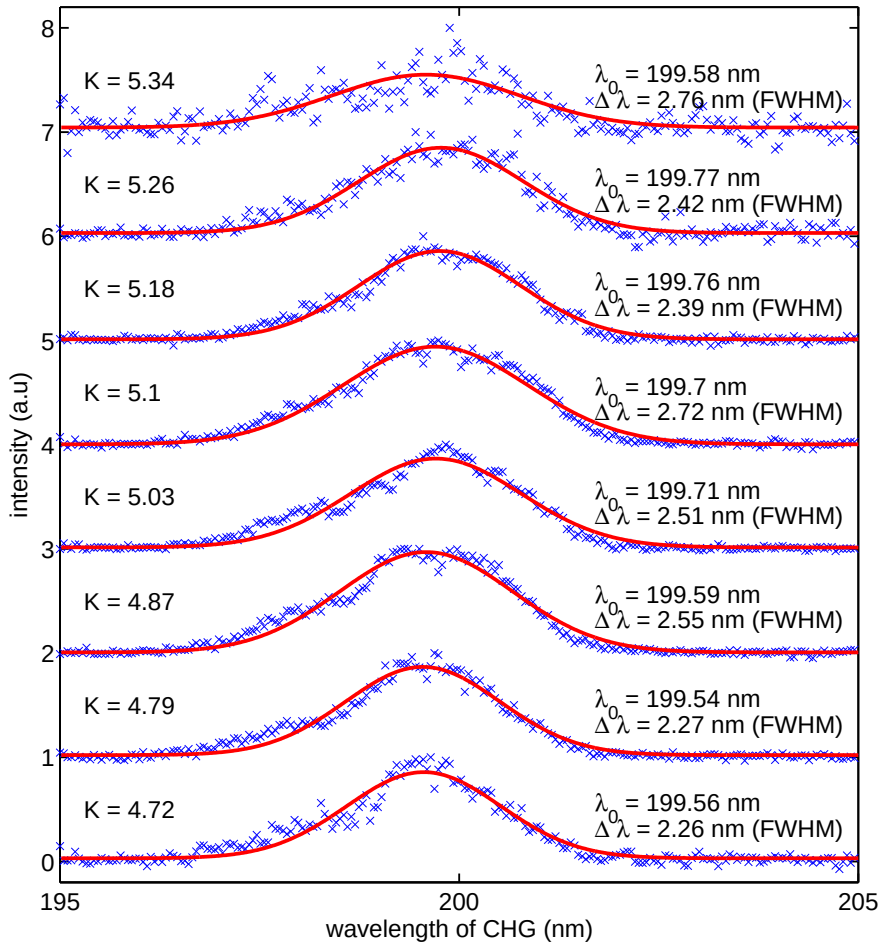

Figure 5.5: CHG spectra under variation of the K value of the radiator.

the CHG intensity increases due to improved microbunching. At the maximum available chicane current of 800 A, equivalent to an r_{56} value of about 11 µm, the CHG intensity is highest. The peak of the Bessel function (Eq. 2.99) could not be reached, because neither the laser energy nor the chicane strength was high enough to get the optimum microbunching. These measurements were done before rewiring the chicane.

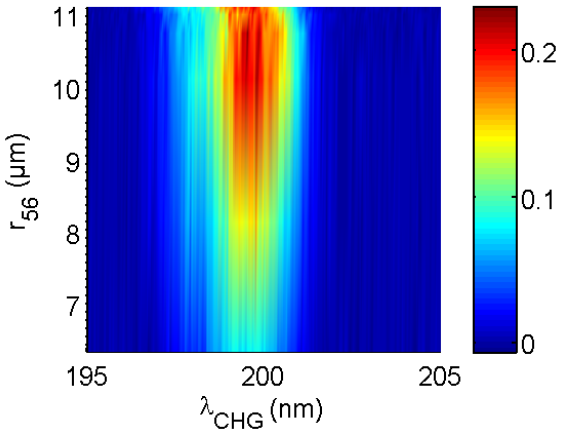

Figure 5.6: CHG spectra under variation of the R_{56} value of the chicane.

CHG spectra were measured while fixing the K value of the radiator and modulator but changing the wavelength of the laser. The spectrum of the 400-nm seed laser was shifted slightly (by 2 nm) by turning the BBO crystal in the second harmonic generation (SHG) unit. Spectra of 400-nm laser pulses and resulting CHG radiation are shown in Fig. 5.7. The CHG wavelength varies by about (1.59 ± 0.25) nm (Fig. 5.7). It is determined directly by the wavelength of the laser, since the laser bandwidth is much smaller than the undulator bandwidth.

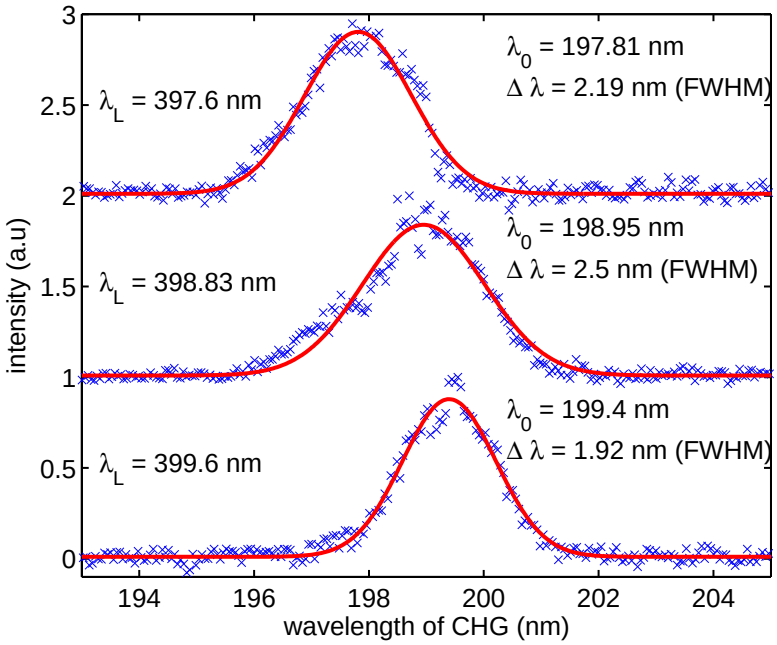

(a)

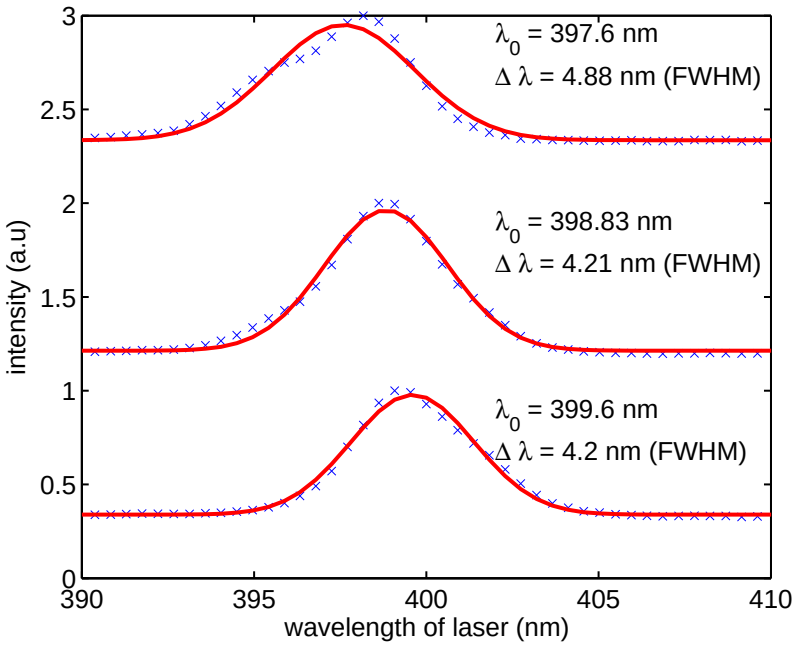

(b)

Figure 5.7: The CHG spectra (a) are measured under the variation of the seed-laser spectra (b).

5.3 Modification and characterization of the magnetic chicane

The CHG facility at DELTA has been significantly improved by modifying the magnetic chicane. Initially, the magnetic chicane was formed by three undulator periods with an increased magnetic field. By rewiring the poles of the chicane, thus changing the shape of the magnetic field along the z-axis, a much larger transverse excursion was created (Fig 5.8) leading to higher r_{56} values. Before rewiring, the maximum r_{56} value was limited to 11 µm. It was increased up to 130 µm by modifying the chicane, causing a dramatic rise in the intensity of the CHG radiation. Further details about the modification can be found in [28]. Besides improvement of the CHG radiation power, a set of new characterization experiments became possible.

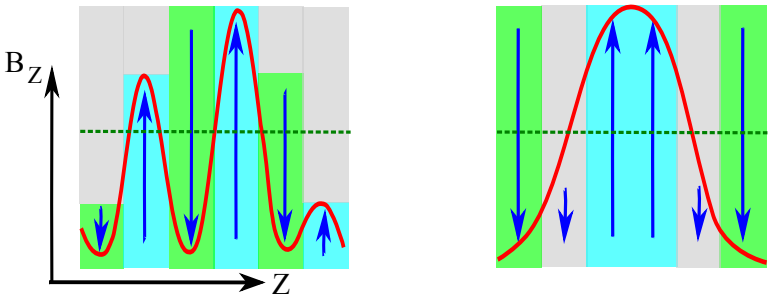

Figure 5.8: The scheme of the magnetic poles of the chicane before (left) and after (right) rewiring. After rewiring, the vertical magnetic field B_z (red line) along the z-axis is symmetric and u-shaped yielding higher r_{56} values up to 130 µm.

The spectrum of the "symmetric" optical klystron (OK), i.e. both modulator and radiator tuned to the same resonance wavelength (here 400 nm), was measured for different chicane currents. Fig. 5.9(a) shows three example spectra of the OK using the rewired chicane for small, optimum (for CHG), and high chicane currents.

By fitting the measured spectra to Eq. 2.21, the r_{56} values as function of the chicane current could be derived (Fig. 5.9(b)). The approximation of this function by the quadratic form $r_{56} = aI^2 + bI + c$ with $a = 0.26 \times 10^{-3}$ µm/A^2, $b = 17 \times 10^{-3}$ µm/A, $c = 2.0$ µm is used for further analysis in this Chapter.

CHG spectra at higher chicane values

When deviating from optimized laser and chicane parameters, the spectral shape changes drastically. For example, increasing the chicane strength leads to an optimum bunching factor (given by constant $r_{56} \cdot \Delta E$) for electrons with lower energy modulation ΔE on the slopes of the slopes of the distribution of the modulation while overbunching the central part. This results in a coherent double pulse, the spectrum of which contains interference fringes. The time between the two pulses should increase with r_{56} while the spectral separation of the fringes

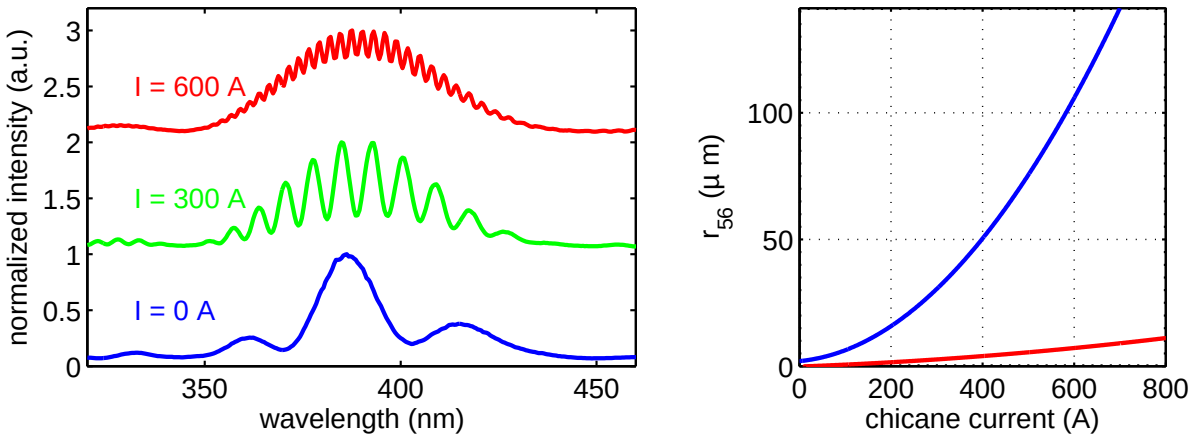

(a) (b)

Figure 5.9: a) Example spectra of a symmetric OK measured while using the rewired chicane at three different chicane currents I. b) Dependence of r_{56} on the chicane current before rewiring (red) and after rewiring (blue).

should decrease. This tendency is clearly observed in the examples in Fig. 5.10, the second harmonic of 800 nm (corresponding to a frequency around 750 THz) with r_{56} values of 20, 53, and 102 µm, but the spectra contain additional unexpected features such as the suppression of the central peak. Further measurements have shown that a slight misalignment of the Ti:sapphire laser compressor, leading to chirped pulses, can produce such features. Additional measurements and simulations are required to arrive at a quantitative understanding of the rich spectral structure observed in CHG radiation under various conditions.

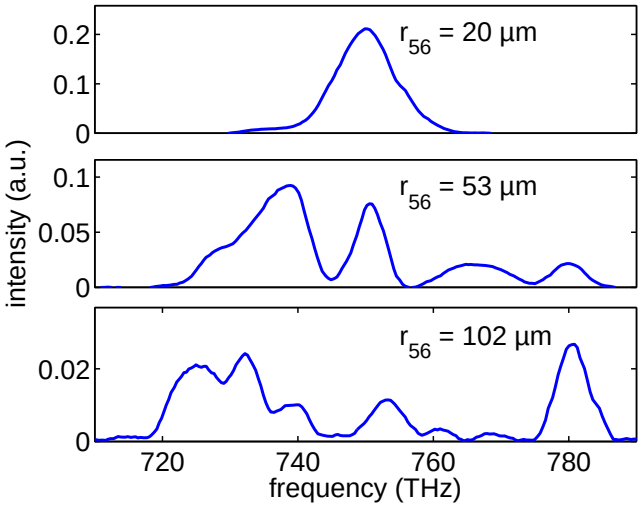

Figure 5.10: CHG spectra around 400 nm (750 THz), the second harmonic of the seed wavelength, under variation of the chicane strength.

5.4 Relative intensity and pulse energy

The observed CHG-to-SE ratios vary from zero to a few thousand depending on the bunching factor, which is determined by the harmonic number, energy modulation (given by the laser power) and chicane strength (Eq. 2.99). Most of the time, the power of the seed laser pulses was set to about 3.5 W while seeding with the fundamental 800-nm wavelength. While seeding with 400 nm, the available laser power was between 1.6 W and 2.6 W, depending on the efficiency of the SHG unit, the length of the 800-nm laser pulses, and the day-to-day performance of the laser amplifier. In Section 4.2, the CHG-to-SE intensity ratios detected in BL 5 were presented for wavelengths below 200 nm; in the following, the ratios of 200- and 400-nm CHG radiation and estimates of their pulse energy are discussed.

In BL 5, contrary to BL 4, almost the whole CHG and SE beams are focused on the sample (by three focusing mirrors in the beamline). This affects the ratio detrimentally, as spontaneous emission has a larger angular distribution (see Section 5.1). In addition, only a part of the photoelectrons passes through the energy analyzer and reaches the delay line detector (DLD) due to the limiting slit size at the entrance of analyzer. In BL 4, only a small part of the beam is focused on the avalanche photodiode (APD), and the beam is steered in such a way that the maximum CHG-to-SE ratio is detected. The highest recorded CHG to SE ratio measured at BL 4 was of the order of 1000, measured for 400-nm CHG radiation as second harmonic of the 800-nm laser. The power of the seed-laser pulses was about 3.5 mJ. While seeding with 400-nm seed-laser pulses, the maximum detected ratio in BL 4 was of the order of a few 100 at 200 nm.

In single-bunch operation, the repetition rate of the SE pulses is 2600 times the repetition rate of the CHG pulses. Typical powermeters average the signals over hundreds of milliseconds, therefore the SE radiation power dominates and the CHG power cannot be measured directly. Nevertheless, the absolute energy of the CHG pulses can be estimated by measuring the power of the spontaneous synchrotron radiation and using the known relationship between them (Eq. 5.2).
In the following calculations, the intensity ratios of $I_{\mathrm{CHG}}/I_{\mathrm{SE}} = 400$ and 2000 are used to estimate the 200-nm (second harmonic of 400 nm) and 400-nm (second harmonic of 800 nm) CHG pulse energies, respectively.
These ratios were measured using a pinhole spectrometer (monochromator+APD), i.e. with a small spectral and spatial width, while the SE power was measured by focusing the whole beam with a fused silica lens on the silicon-head powermeter. Furthermore, the radiation was not monochromatic but was deflected by coated mirrors within a certain bandwidth. Therefore, the beam spot size and bandwidth should be taken into account.

While measuring the power, 50-mm and 25-mm diameter mirrors were used at the beam path in the diagnostics hutch at 400 nm and 200 nm wavelengths, respectively, by which the diameter of the SE beam was limited.
The diameter of the CHG spot was typically about $4\sigma = 20$ mm ($\sim$ 12 mm FWHM) at 400 nm, and $4\sigma = 12$ mm ($\sim$ 7 mm FWHM) at 200 nm (see Figs. 5.17 and 5.19).
The bandwidth of CHG at both wavelengths is about 1.5%, and the bandwidths of the 400- and 200-nm SE are about 10% and 5% (FWHM of 40 nm and 10 nm), respectively, given by the bandwidths of the deflecting coated mirrors. The total CHG pulse energy W_{CHG} and photon flux N_{ph} [photons/pulse] can be estimated by

$$W_{\mathrm{CHG}}(\lambda) = W_{\mathrm{SE}}(\lambda) \left(\frac{I_{\mathrm{CHG}}}{I_{\mathrm{SE}}}\right) \left(\frac{A_{\mathrm{CHG}}}{A_{\mathrm{SE}}}\right) \left(\frac{\Delta\lambda_{\mathrm{CHG}}}{\Delta\lambda_{\mathrm{SE}}}\right), \tag{5.1}$$

$$N_{\mathrm{ph}}\,[\mathrm{photons/pulse}] = W_{\mathrm{CHG}} \frac{\lambda}{hc}\,; \qquad W_{\mathrm{SE}}(\lambda) = P_{\mathrm{SE}}/f_{\mathrm{SE}} \tag{5.2}$$

with $\Delta\lambda_{\mathrm{CHG}}/\Delta\lambda_{\mathrm{SE}}$ being the bandwidth ratio, W_{SE} the pulse energy of SE, and $f_{\mathrm{SE}} = 2.6$ MHz the repetition rate of the SE pulses. The ratio between the SE and CHG beam area is denoted by $A_{\mathrm{CHG}}/A_{\mathrm{SE}}$. The measured SE power P_{SE} and the estimated CHG pulse energy and photon flux are summarized in Table 8. The measurements were done with a single bunch of about 10 mA current.

λ	P_{SE}	W_{CHG}	CHG photon flux
400 nm	250 µW @ 10% BW	5 nJ @ 1.5% BW	1×10^{10} photons/pulse
200 nm	20 µW @ 5% BW	0.2 nJ @ 1.5% BW	2×10^{8} photons/pulse

Table 8: Measured SE power P_{SE} and estimate of the pulse energy W_{CHG} and photon flux of the 200-nm (second harmonic of 400 nm) and 400-nm (second harmonic of 800 nm) CHG pulses for 10 mA single-bunch current.

In addition, the intensity of the spontaneous emission from the undulator (P_{SE}) was simulated using the program *spectra* [37] (Fig. 5.11). In this simulation, an undulator with 7 periods and with undulator and beam parameter at DELTA (see Table 1 in Section 3.1) was assumed. Due to the bandpass filters used in the beam path, the main part of the SE radiation is from the radiator (with 7 periods) tuned to the CHG wavelength. The single-bunch current in this simulation was 20 mA. The calculated P_{SE} is 46 nW and 182 nW for 1% bandwidth of a 1-mm^2 400-nm and 200-nm SE beam, respectively. After multiplying to the aforementioned spectral bandwidths and beam sizes, the order of the values obtained by this simulation conforms the values obtained by the measurements (Table. 8). Although, contrary to the simulation, the measured SE power at 400 nm is higher than at 200 nm, because the 400-nm

SE beam was bigger due to 50 mm mirrors, and also the 200-nm SE is partially absorbed in air.

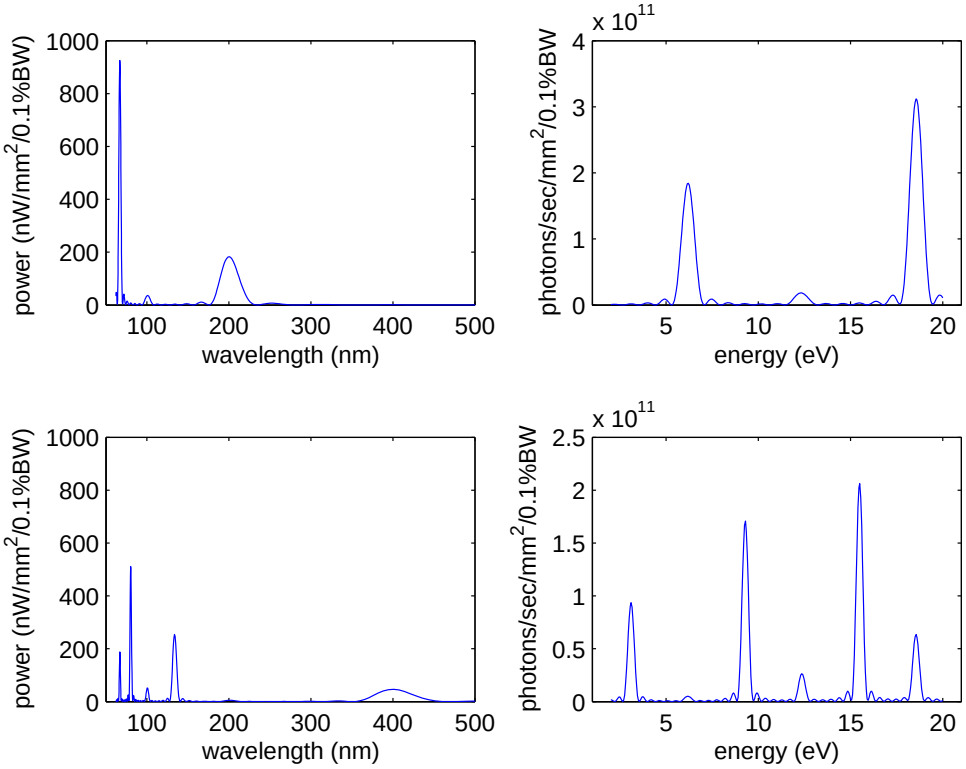

Figure 5.11: Photon flux of SE vs. photon energy, simulated using the program *spectra* [37] (right), and calculated radiation power from the photon flux (left) for the radiation from undulator tuned to 200 nm (6.2 eV; top) and 400 nm (3.1 eV; bottom).

5.5 Estimate of energy modulation

A possible way to estimate the energy modulation is to observe the CHG intensity while varying the chicane strength. The energy modulation can be determined by fitting Eq. 2.99 to these data. In the previous Chapter, such measurements at BL 5 were presented for wavelengths below 200 nm. Here, examples are shown for 200 nm, the second harmonic of 400 nm, measured at BL 4 for two different laser energies (Fig. 5.12). The laser energy in horizontal polarization was varied using a half-wave plate.

The green points in Fig. 5.12 (a) represent the data obtained before rewiring the chicane showing the limitations of that configuration. As the chicane strength increases, the CHG intensity also increases and reaches a maximum around $r_{56} = 23$ µm and 43 µm, respectively, for $E_L = 2.6$ mJ and 1.3 mJ. Further increasing the chicane strength causes a second maximum to appear which corresponds to overbunching and the formation of a double-peak structure in the longitudinal density distribution (Fig. 5.13). The slight discrepancy between the

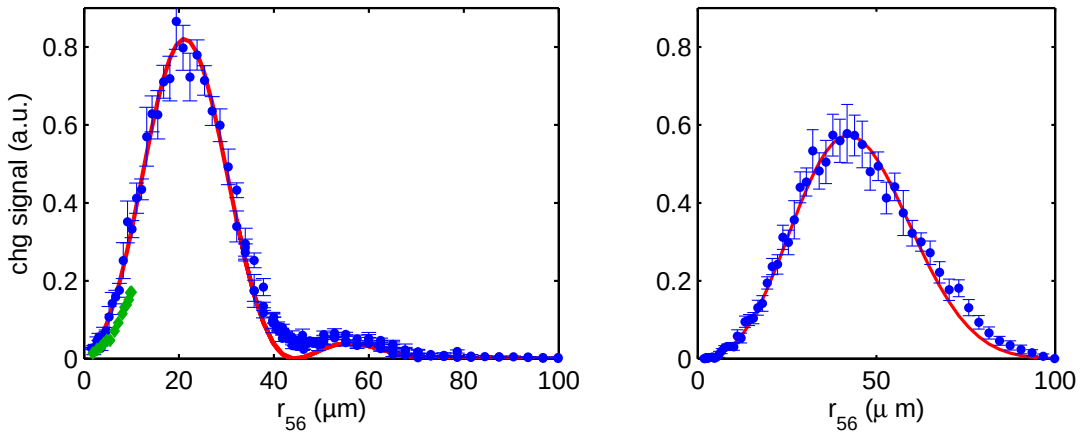

(a) (b)

Figure 5.12: CHG intensity vs. chicane strength for a laser pulse energy of $E_\mathrm{L} = 2.6$ mJ (a) and for $E_\mathrm{L} = 1.3$ mJ (b).

theoretical fit and the measurement in Fig. 5.12 can be due to neglecting the Gaussian distribution of the laser pulse and assuming a constant laser pulse energy.

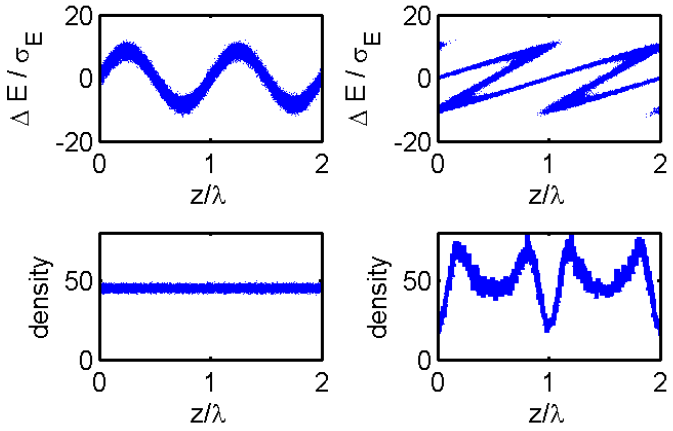

Figure 5.13: Energy modulation and density distribution of the electrons in the modulator (left) and after passing the chicane (right). Due to the high r_{56} value, there is an overbunching in the chicane. The relative energy modulation over the relative energy spread is denoted by $\Delta E/\sigma_\mathrm{E}$.

As shown in Fig. 5.14, the measured energy modulation is proportional to the square root of the laser pulse energy, confirming the theory (Eq. 2.97).

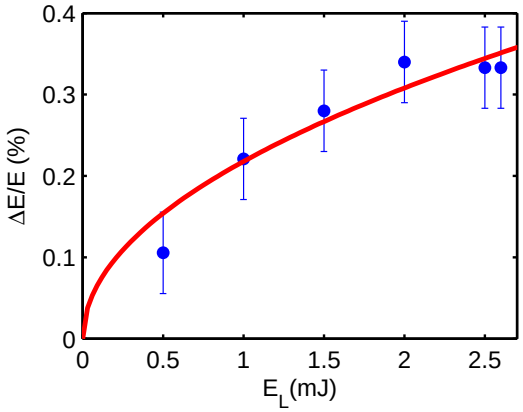

Figure 5.14: Energy modulation amplitude versus laser pulse energy. The solid line shows a function proportional to the square root of the laser pulse energy.

5.6 Coherence measurements

The coherence properties of the CHG radiation were investigated by conducting classic double-slit and Michelson experiments. The coherence functions and coherence lengths of 400-nm and 200-nm CHG and SE pulses were determined. Furthermore, the coherence time was also measured by combining the double slit with two pairs of transparent wedges and making a delay between the two partial pulses from slits.

ICCD camera

The interference patterns were recorded by means of a fast-gated intensified CCD camera (ICCD) with a shortest gating time of 3 ns (dicam pro from PCO) [109]. This camera contains an image intensifier unit which includes a photocathode, a multi-channel plate (MCP) and a phosphor screen (Fig.5.15). There is a collimator lens and an output lens between the image intensifier and the CCD, which scales the image by a ratio of 1/2.17. This ratio was confirmed by measurements using a test target. The resolution of this optics (given in the data sheet) is better than 60 LP/mm @ 5% modulation transfer function (MTF) with LP being the number of the line pairs. The number of pixels of the CCD is 1280(H) × 1024(V), and the size of each pixel is 6.7 µm × 6.7 µm, yielding a total size of 8.6 mm × 6.9 mm.

The resolution and the scaling rate of the camera was verified by using a resolution test target (USAF-1951) which is a set of clear lines on an opaque chrome background (a 1.5 mm thick optical glass substrate). Each group of lines contains 6 elements with increasing number of line pairs. The line width of and space between each element is equal to 1 mm /(2 LP), and the line length is equal to (5 mm)/(2 LP). An example image of this target taken by the ICCD camera is shown in the first plot in Fig. 5.16. The test target was placed directly in

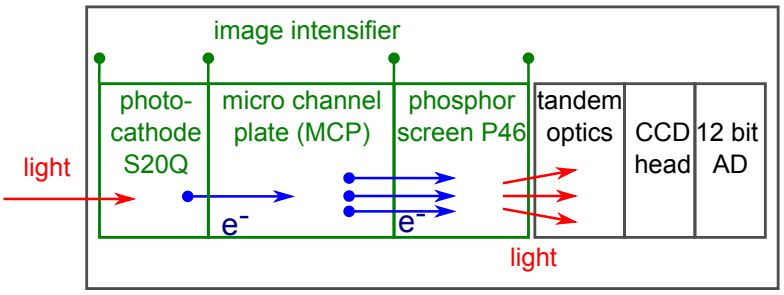

Figure 5.15: Block diagram of the ICCD camera including an image intensifier unit, tandem optics, CCD head and a 12-bit digitization unit.

front of the camera. A convex lens with $f = 100$ mm placed 72 cm before the test target was used to expand a white light on the target.

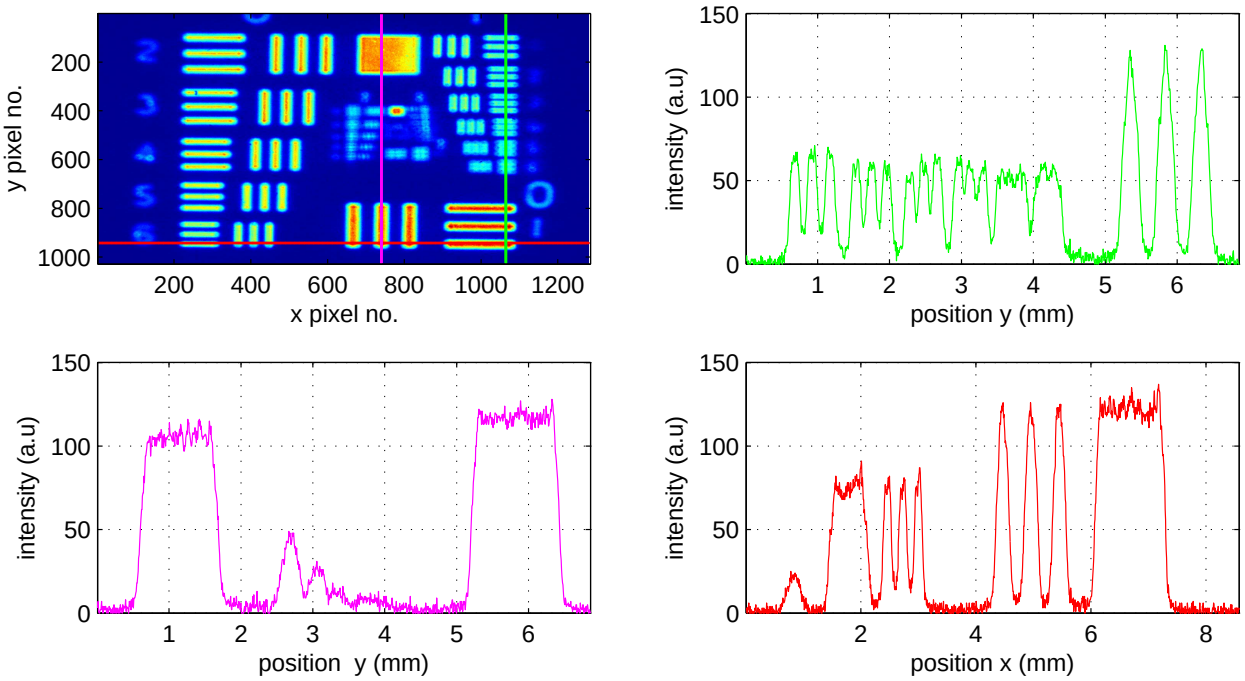

Figure 5.16: The image of the test target taken by means of the ICCD camera. The test target was placed right in front of the aperture of the camera (top left). The intensity of the image along the green, magenta and red lines as marked on the 2D image.

It can be seen from Fig. 5.16 (top right) that at the fourth element in group one (with LP = 2.83), the contrast of the lines falls to about 25%. The red and the magenta colored plots are used to calibrate the length, giving a scaling ratio of about 1/2; close to the value given in the data sheet.

CHG and SE beam profile

Example profiles of the 200-nm CHG and SE beams (second harmonic of 400-nm seed) measured using the ICCD camera, are shown in Fig. 5.17. The intensity profile is strongly modulated, mainly due to the rough and degenerated surface of the in-vacuum deflecting Cu/Al mirror in BL 4. A photo of this mirror (Fig. 5.18) illustrates that its surface is damaged by radiation.

A bandpass filter with a FWHM bandwidth of 10 nm used in front of the camera eliminates the red-shifted parts of the SE and reduces the spot size. The spot size of the SE is also limited by the 25-mm mirrors, while the CHG spot is smaller and almost centered to the optics. The profile of the CHG radiation has a Gaussian shape with a FWHM width of about 6.5 mm in both horizontal and vertical directions.

In Fig. 5.19, the image of the 400-nm CHG and SE spots after exchanging the first in-vacuum deflecting mirror in BL 4 is shown. The quality of the beam profile is evidently improved. The intensity is more uniform. The measured 400-nm-CHG beam size is about 12 mm; larger than the 200-nm-CHG beam size. A possible reason is a change in laser beam size due to different telescopes in the seed beamline for 800-nm and 400-nm seed pulses.

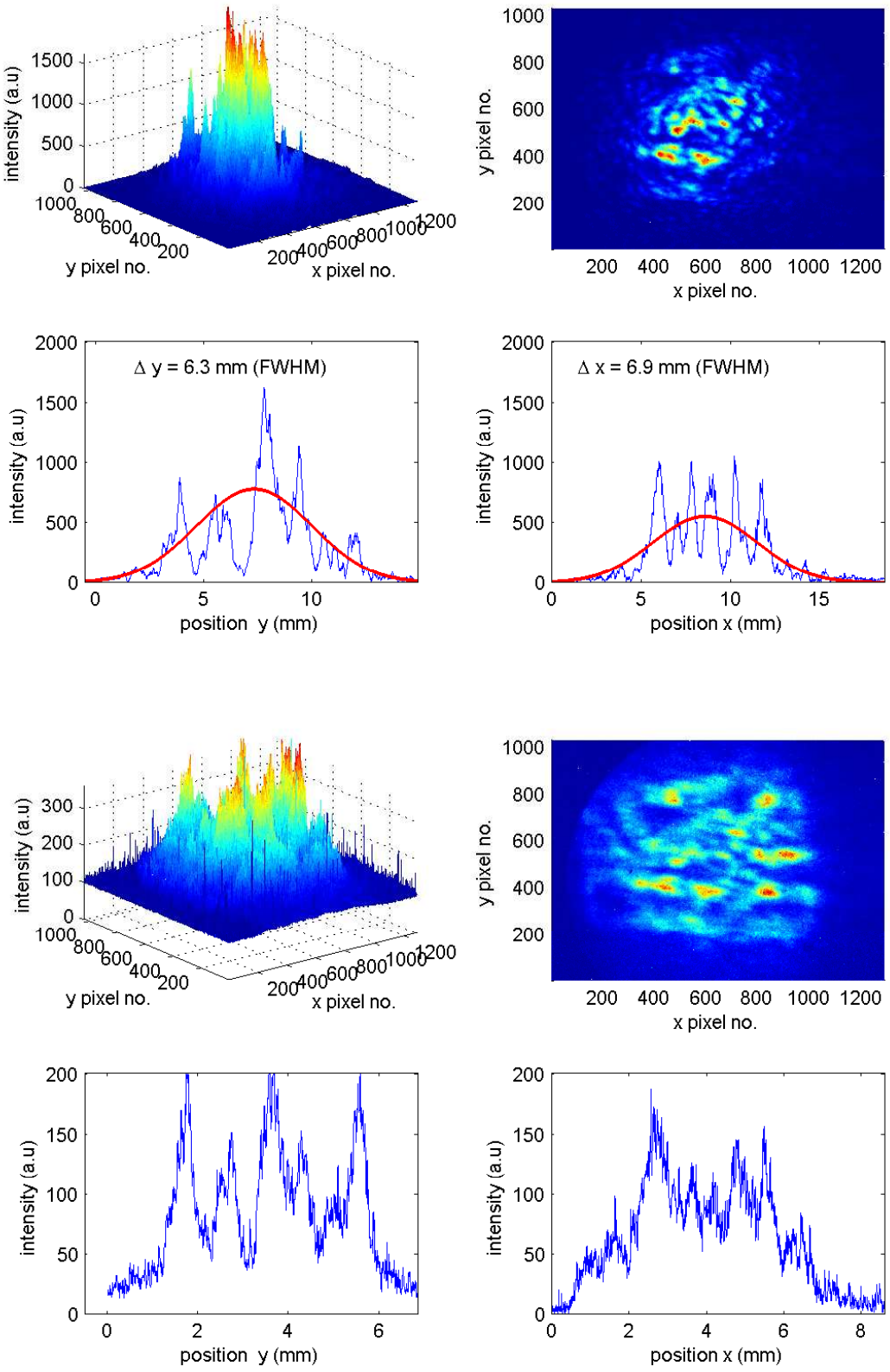

Figure 5.17: The profile of 200-nm CHG radiation (top) and SE (bottom) measured using the ICCD camera. The curves show the intensity along a line crossing the center of the beam in horizontal (y) and vertical (x) directions. The x- and y-axes are the pixel numbers multiplied with the pixel size. The blue curve is the measurement, and the red curve is a Gaussian fit, the FWHM width of which is denoted by Δy and Δx.

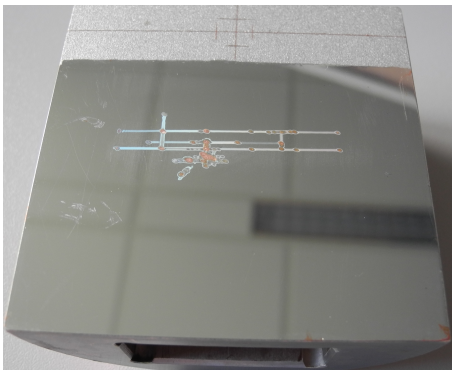

Figure 5.18: Image of the Cu/Al mirror deflecting the radiation into BL 4, showing surface damage due to the synchrotron radiation and laser beam.

Data analysis of interference experiments

in order to analyze interference fringe patterns (from a double-slit setup and Michelson interferometer) and to derive the coherence from them, three methods are applied in this thesis yielding consistent results.

- In the first method, the visibility of the fringes is estimated by finding the maxima and minima.

- In the second method, a theoretical expression of the interference pattern in near field (Eq. 2.88) is used to fit the experimental data leading to the coherence.

- In the third method, the fringe patterns are 2D-Fourier transformed, resulting in a pattern which can be used to calculate the coherence, as described in the following [111].

The intensity distribution of the interference pattern of two beams with intensities $I_1(\vec{u}) = I_2(\vec{u}) = I_0(\vec{u})$ can be expressed as [35]

$$I(\vec{u}) = 2I_0(\vec{u})(\{1 + \gamma_{12}(\tau)\ \cos[\phi(\vec{u}) + \alpha_{12}(\tau)]\}\,, \tag{5.3}$$

where $\vec{u}(x, y)$ is the position vector on the observation plane, τ is the time delay caused by the difference between the propagation path lengths of the two beams, and $\gamma_{12}(\tau)$ is the coherence. The slowly varying phase of γ_{12} is denoted by $\alpha_{12}(\tau)$, and $\phi(\vec{u})$ is the rapidly changing phase which gives rise to interference fringes. In case of double-slit experiment, $\phi(\vec{u})$ equals to $2\pi\vec{u} \cdot \vec{d}/(L\lambda)$ with L being the distance between the slits and detector, and $\vec{d} = (d_x, d_y)$ being the slit separation in the horizontal and vertical direction. The Fourier

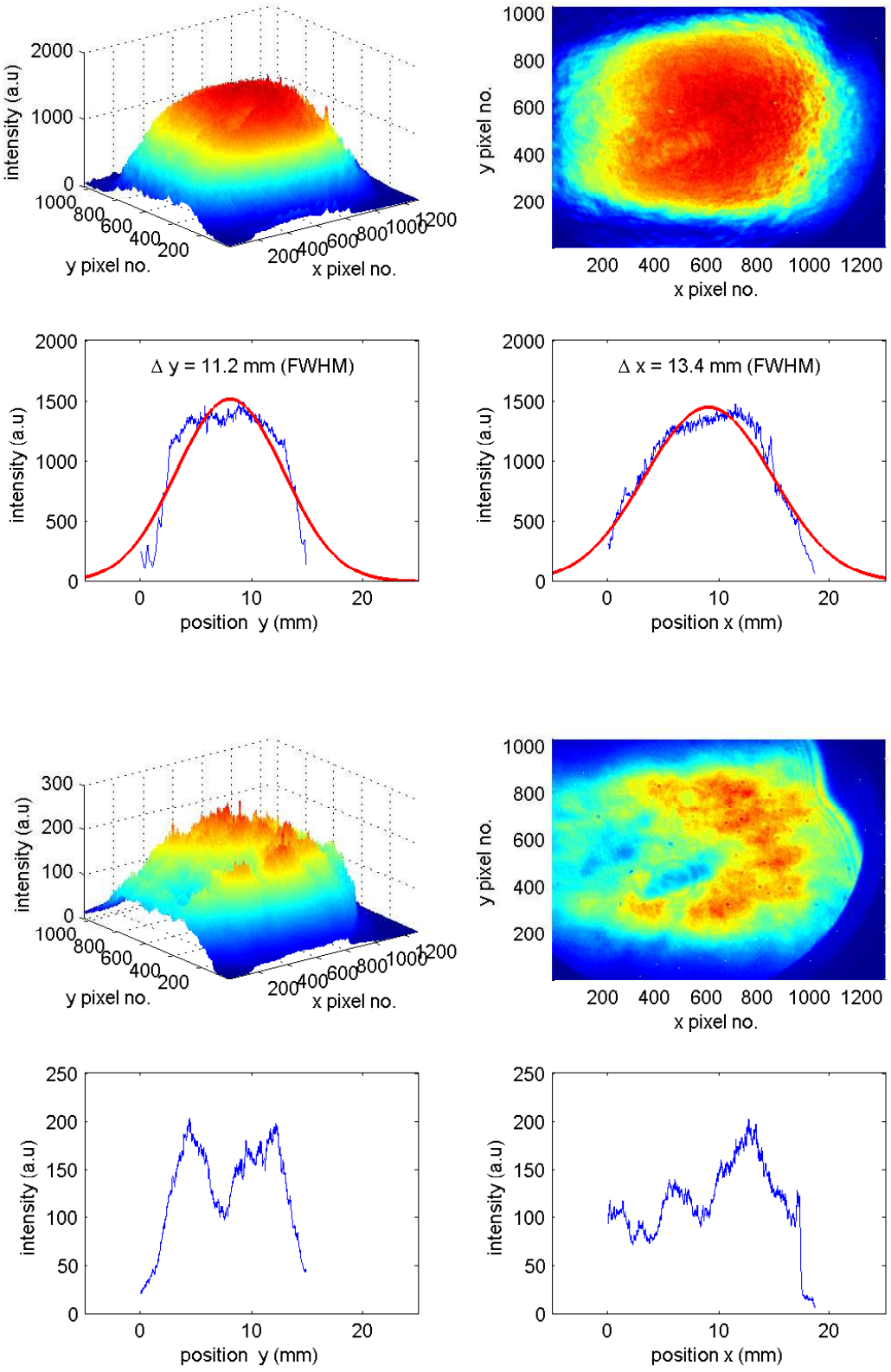

Figure 5.19: The profile of 400-nm CHG (top) and SE radiation (bottom) measured using the ICCD camera, after exchanging the first deflecting mirror in BL 4. The curves show the beam profile along a line crossing the center of the beam in horizontal (y) and vertical (x) directions. The blue curve is the measurement, and the red curve is a Gaussian fit, the FWHM of which is denoted by Δy and Δx.

transform of Eq. 5.3 in the frequency domain yields [111]

$$\tilde{I}(f) = 2\tilde{I}_0(f) \otimes \left\{ \underbrace{\delta(f)}_{\mathrm{AC}} + \frac{1}{2}\gamma_{12} \left[\underbrace{\delta(f+f_\mathrm{s})}_{\mathrm{XC}} e^{-i\alpha_{12}(\tau)} + \underbrace{\delta(f-f_\mathrm{s})}_{\mathrm{XC}} e^{i\alpha_{12}(\tau)} \right] \right\}, \tag{5.4}$$

where δ is the Dirac delta function, $\otimes$ is the convolution operator, f is the frequency coordinate, and f_s is the fringe frequency. In Fourier space, the central term is the sum of the autocorrelation (AC) functions of the two beams, and the sideband terms contain information on the degree of cross correlation (XC) between the interfering fields. The coherence can be determined as [111]

$$\gamma_{12} = \frac{\tilde{I}_\mathrm{XC}(f_\mathrm{s})}{\tilde{I}_\mathrm{AC}(0)}. \tag{5.5}$$

In all of these methods, a background image was subtracted from the interference pattern image before analyzing it. The background image of the CHG radiation is taken by the camera after shifting the trigger of the laser away from the electron bunch, using a vector modulator. This causes temporary mismatching of the longitudinal overlap, so that only the SE radiation and possibly stray light of the laser pulses is present in the background image.

When $I_1 \neq I_2$, the contrast observed in the experiments is reduced compared to the coherence of the incident radiation as given in Eq. 2.61.

A 25-mm-diameter bandpass filter was always mounted directly in front of the camera with a FWHM bandwidth of 10 nm for 200-nm radiation and 40 nm at 400 nm, unless stated otherwise. These filters are important for blocking the laser beam and its stray light. The bandwidth of the CHG radiation is not affected by these filters, while the bandwidth of SE is determined by them.

For double-slit experiments, no lens was used in the beam path. In case of the Michelson experiment, a lens with a focal length of 100 mm was used to focus the light on a point approximately 10 mm before the beam splitter. The divergent light after the beamsplitter makes it possible to resolve the circular fringes with the camera. Without a lens the fringes would be too close to each other to be resolved. No additional apertures were used in either experiment.

5.6.1 Transverse coherence

In order to study the transverse coherence properties of CHG radiation and SE, double-slit experiments were performed using several slits with different dimensions. The visibility of the resulting interference fringes depends on the slit width, the slit separation and the distance from the source. The distance of the measurement point from the radiation source, i.e. the radiator, was about 10 to 12 meters, and the distance of the slits from the camera L was about 1 to 2.5 meters in different experiments. In such a distance and with a slit separation of $d \approx 1$ mm, the near field condition for double slit $L\lambda \leq \pi d^2$ holds, approximately.

Several double-slits with different dimensions were employed for the measurements. The arrangement of the double-slit set and its photo is shown in Fig. 5.20. These slits were processed with laser cutting by the company MEKO [110] with a tolerance of ±5 µm in slit width and separation. The material is standard stainless steel (1.4301) with a thickness of 50 µm.

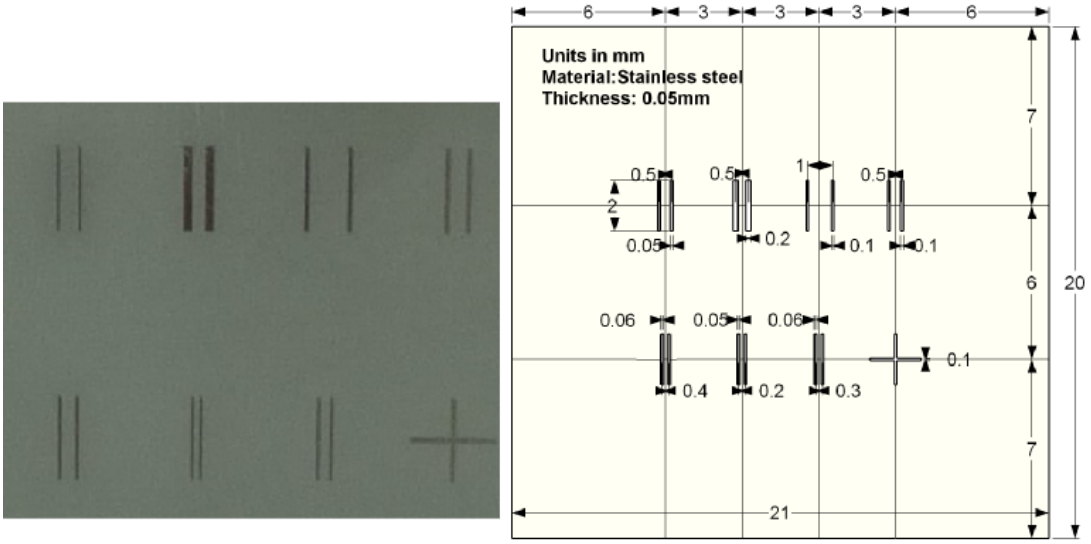

Figure 5.20: Dimensions and arrangement of double slits. Distances are given in mm.

One example of the interference pattern and the intensity profile of 400-nm CHG radiation is shown in Fig. 5.21, in which the slit width was 0.1 mm, the slit separation was 0.5 mm and the distance from the slits to the camera was about 1.18 m. Using the central maximum and minima yields a central fringe visibility of 0.76. This value might be slightly different from the coherence value due to non-uniform intensity distribution of the CHG spot and non-equal slit widths. Both lead to non-equal light intensities from the slits, hence reducing the fringe contrast.

The calibration of the x-axis of all fringe patterns in this Chapter is done by multiplying the pixel sizes with the number of pixels and the scaling factor 2.17 of the internal optics

(see Section 5.6). The angle θ is derived by dividing this value by the distance between the camera and the slits. The fringe separation is theoretically given by Eq. 2.84. By substituting the values of $\lambda = 400$ nm, $L = 1.18$, and $d = 1$ mm, a fringe distance of $\Delta x \approx L\lambda/d = 472$ µm is expected. The measured distance between the fringes is about 470 µm.

Once the x-axis is calibrated, the visibility of the fringes along the horizontal axis can be used to get a rough estimate of the longitudinal coherence length, as described in the following. The time delay associated with the path length difference between the waves from two slits to the camera ($\delta\tau_m$ with m being the fringe number) compared to the longitudinal coherence length (Eq. 2.67) determines the visibility at $x \neq 0$. If $\delta\tau_m < \tau_c$, the visibility remains as high as the central visibility, else it will decrease. In Fig. 5.21, the blue curve is a fit assuming a constant visibility along the x axis.
A slight discrepancy in visibility can be seen between the measured data and the fit, but this discrepancy is so small that it might be only due to non-perfect background subtraction or a non-symmetric beam profile. Even on the second order fringes, the fit is still good. It can be concluded that the interference pattern in the range of $x \simeq \pm 8$ mm is not influenced by the

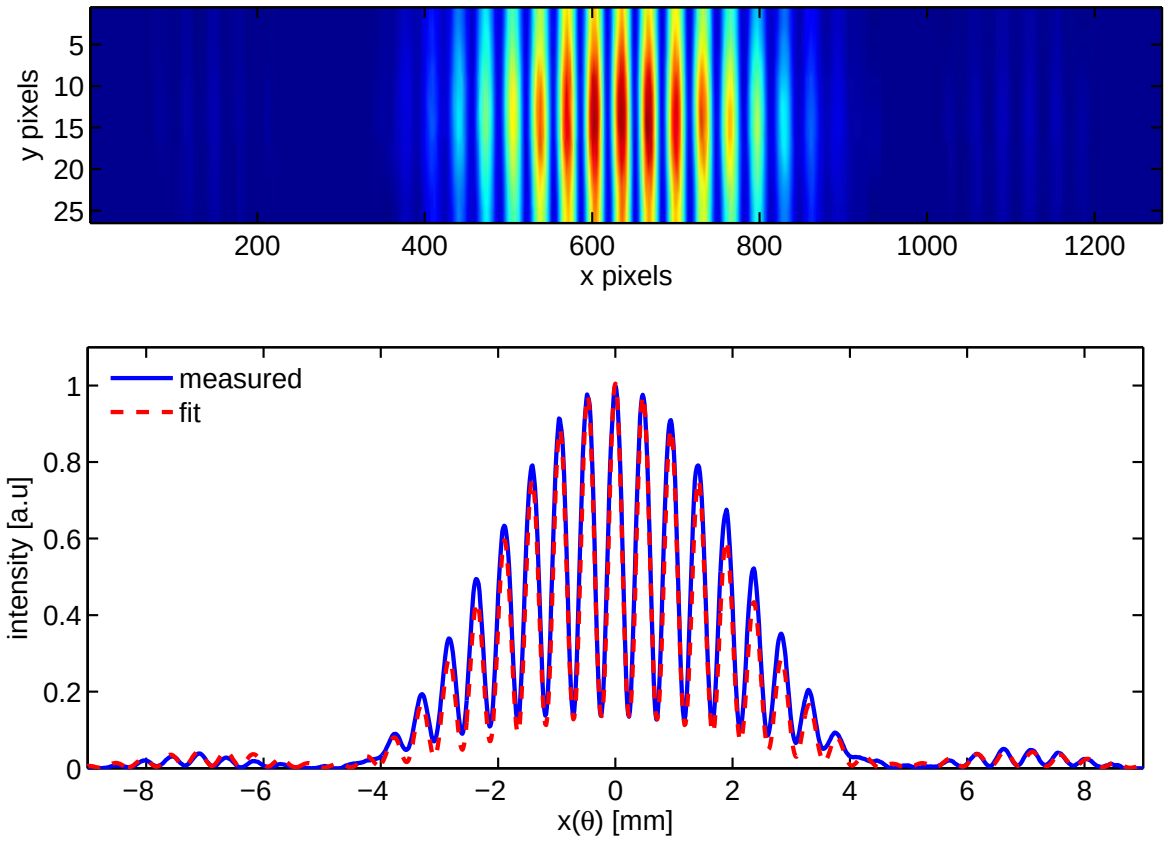

Figure 5.21: Measured interference pattern of CHG radiation at 400 nm obtained with a double-slit with a width of 100 µm and a slit separation of 1 mm (blue line). The red curve is a fit assuming a constant visibility of 0.76 along the x axis.

limited temporal coherence length, and the visibility stays almost constant.

At $x = 8$ mm with $L = 1.18$ m, and $d = 1$ mm, the path length difference between the waves from two slits is $\delta l = d\sin(\theta) = d\tan(\theta) = d \cdot x/L = 6.78 \times 10^{-6}$ m, corresponding to 22.6 fs. It can be concluded that the temporal coherence length of 400-nm CHG pulses is longer than 22.6 fs.
The bandwidth of the CHG spectrum at this measurement was 7.2 nm (FWHM). The longitudinal coherence length for a Gaussian spectrum with this bandwidth would be $l_c = c\tau_c = 0.66\lambda^2/(\Delta\lambda)_{\mathrm{FWHM}} = 14.7$ µm, corresponding to 49 fs.

The dependence of the visibility of fringes from 200-nm CHG pulses on the slit width was studied. The visibility was measured by varying the slit width at a fixed slit separation of $d = 0.5$ mm and $d = 1.0$ mm (Fig. 5.22(a)). As expected, the visibility decreases with increasing slit width.

The lower row of the slit set in Fig. 5.20, which has smaller slit separations and widths, yields a higher visibility (0.7, 0.9, 0.8, respectively from left to right). The highest visibility of 200-nm CHG radiation (second harmonic) was measured with a slit width of 50 µm and slit separation of 200 µm as shown in Fig. 5.22(b).

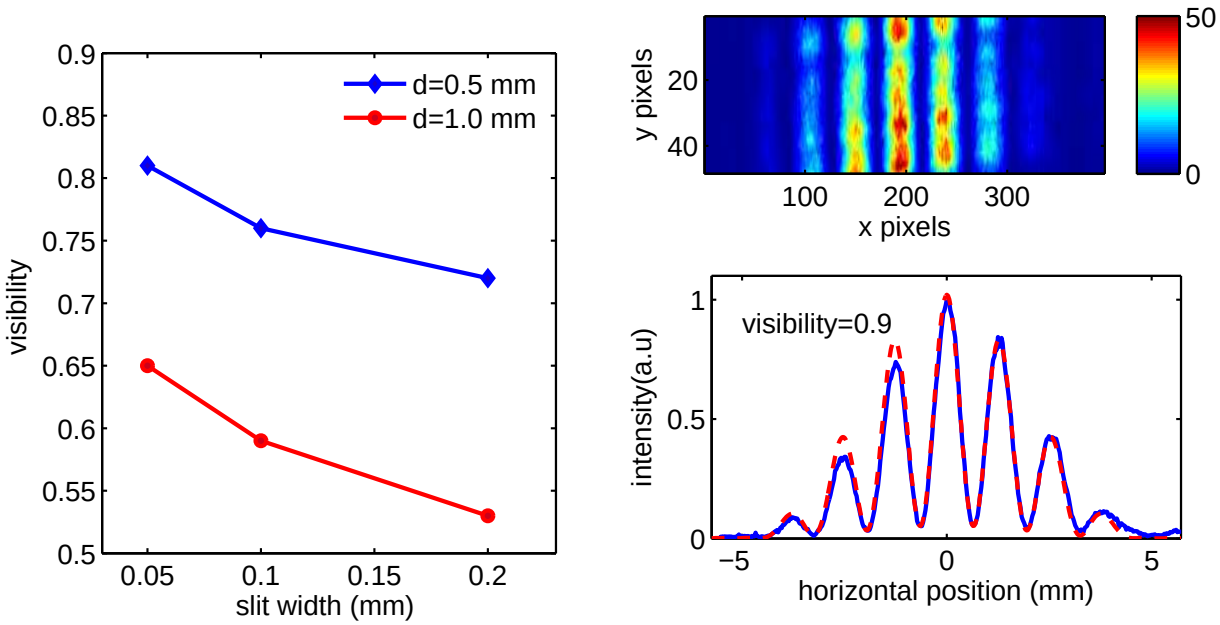

(a) (b)

Figure 5.22: Dependence of the visibility of fringes from 200-nm CHG radiation on the slit width, measured with fixed slit separation of $d = 0.5$ mm and $d = 1.0$ mm (a). Interference pattern and intensity profile of 200-nm CHG pulses, measured with a slit width of 50 µm and slit separation of 200 µm (b).

The errors in the visibility are mainly systematic, for example due to non-uniform beam profiles as mentioned before, leading to non-symmetric fringes. The regions of interest were always selected in the most uniform part of the image. By choosing a region of interest in another part of the image or by changing the size of the actual region of interest, errors were of the order of 1 to 5 percent.

Transverse coherence length of 400-nm CHG radiation

The double-slit experiment was conducted for different slit separations d, and the transverse coherence length was derived as the characteristic width of the normalized mutual coherence function $\mu(d)$

$$l_{\mathrm{c}} = \int_0^\infty |\mu(d)|^2 \mathrm{d}d\,; \qquad \mu(d) = V(d)/V(0). \tag{5.6}$$

A set of slits with a constant slit width but increasing slit separation was designed. For three slit widths (50 µm, 100 µm, 200 µm), the slit separation varies from 1 mm to 3.5 mm in 0.5 mm steps. The arrangement of the double-slit set and its photo is shown in Fig. 5.23.

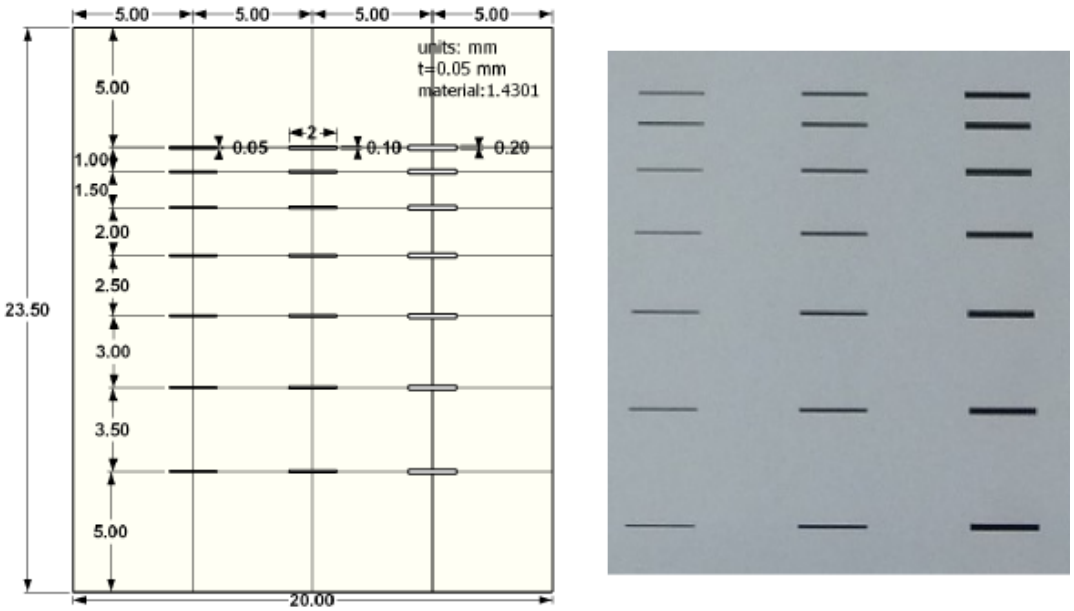

Figure 5.23: Dimensions and arrangements of the double slits used to measure the transverse coherence length.

Examples of the 400-nm CHG radiation fringes (averaged over 64 images) and their intensity profiles in a selected region (ROI) are shown in Fig. 5.24. The slit separations in these two examples are 1 mm and 2.5 mm, the slit width was fixed to 100 µm, and $L = 1.25$ m. The exposure time was about 100 ns, capturing only one SE and one CHG pulse in each

shot. The same measurements were also done with SE and a longer exposure time of about 1 µs, accumulating 64 single shots. The measurement was performed with slits orientations in both horizontal and vertical directions.

The measured visibility of the fringes is shown in Fig. 5.25. According to Eq. 5.6, the normalized visibility should be integrated over d from zero to infinity. A Gaussian function is fitted to the measured data to cover this range, and the coherence length is calculated using this fit function.
The coherence length of 400-nm CHG radiation in both horizontal and vertical direction has almost an equal magnitude of about $l_c = 1.9$ mm. The visibility of the SE fringes is slightly smaller than that of CHG, but the transverse coherence length is almost the same.

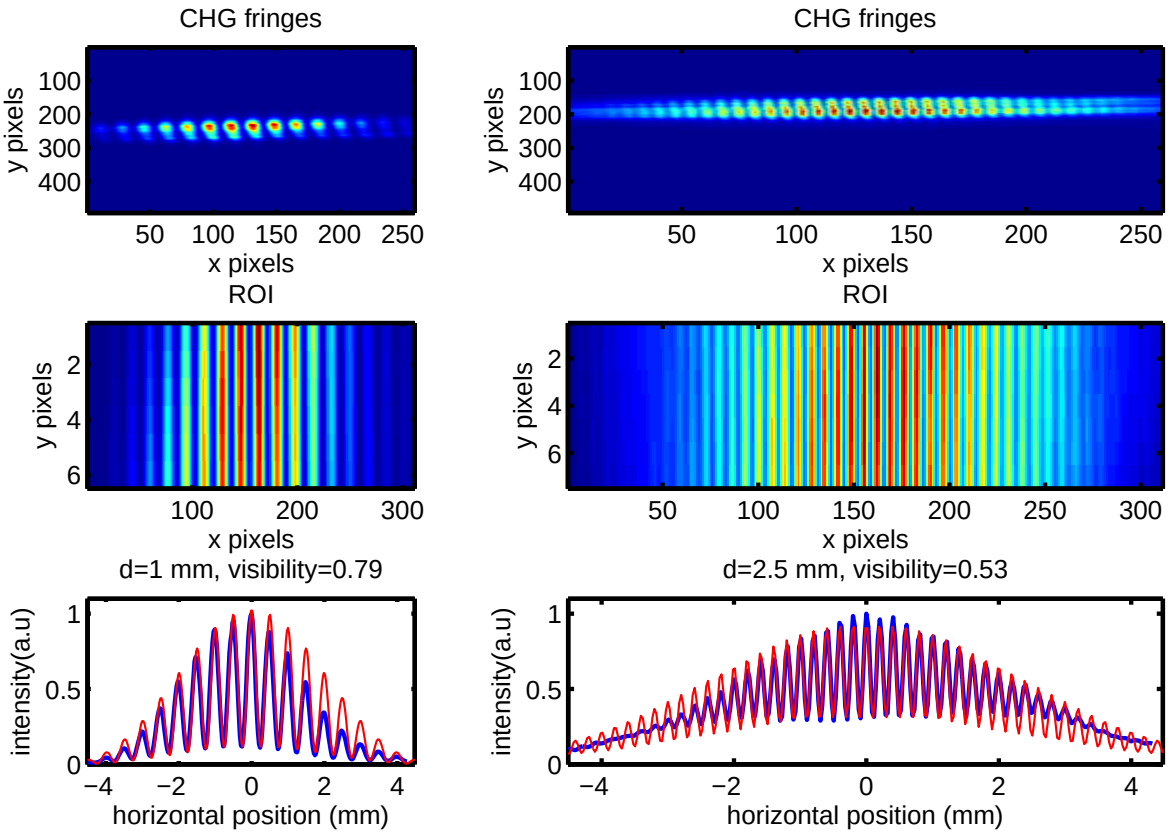

(a) (b)

Figure 5.24: Example fringes of the 400-nm CHG radiation interference pattern with a slit separation of $d = 1$ mm (a) and $d = 2.5$ mm (b). The slit width was 100 µm. The upper plots show the whole pattern, the central plots the region of interest (ROI) which is used to calculate the visibility, and the lower plots show the intensity profile of the fringes in the ROI.

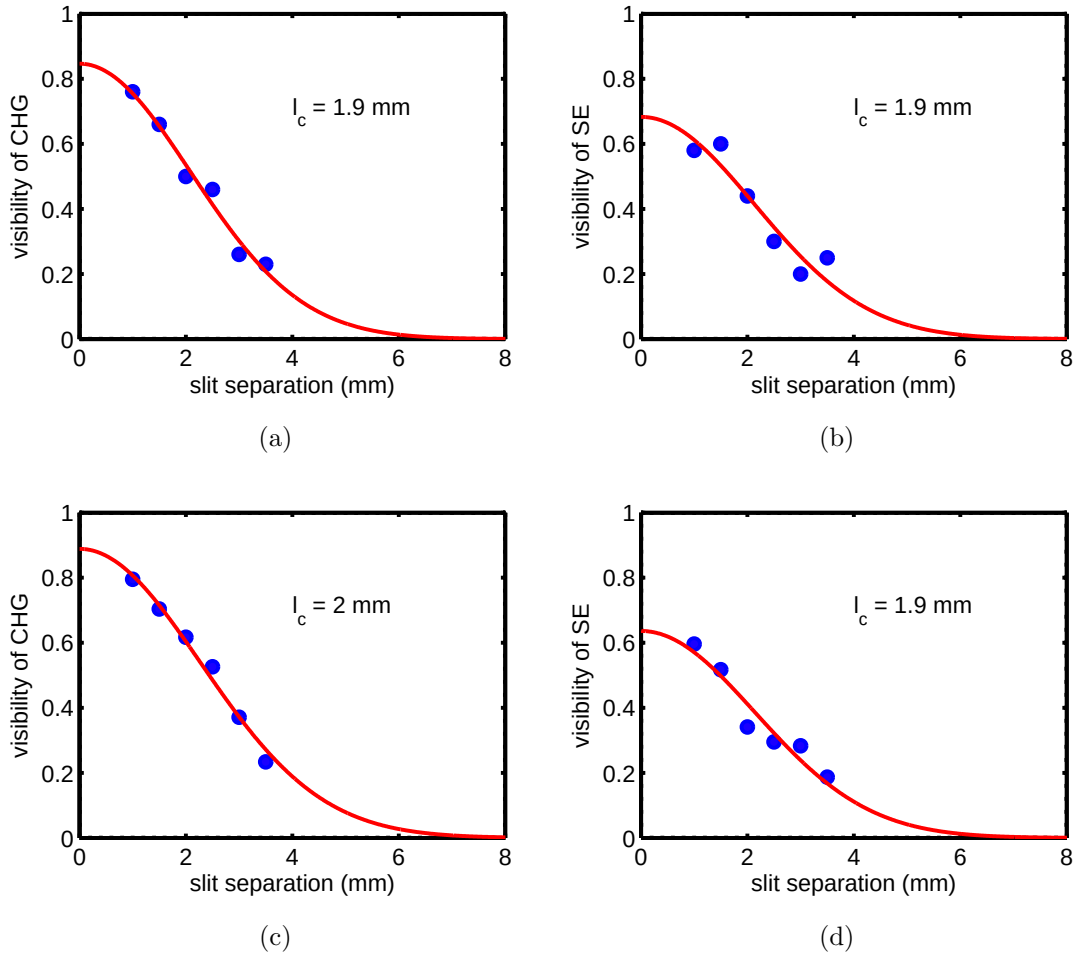

Figure 5.25: Transverse coherence function of 400-nm CHG (left) and SE (right) radiation in the vertical (a,b) and horizontal directions (c.d), measured using a slit with a width of 100 µm. The blue dots are the measured data and the red curve is a Gaussian function.

Transverse coherence length of 200-nm CHG radiation

The transverse coherence length of the 200-nm CHG radiation (second harmonic of 400 nm) was measured in horizontal direction. The results are shown in Fig. 5.26. This measurement was done with all three slit widths. As can be seen, the slit width has no significant influence on the coherence length. The coherence length averaged over the three measurements is about $l_c = 1$ mm.

The transverse coherence length was also measured for the fourth harmonic of the 800-nm seed laser. An example of a 200-nm CHG radiation interference pattern and the visibility versus slit separation is shown in Fig. 5.27.
The intensity variation along the slit in interference pattern is due to the finite size of the slit. A coherence length of about $l_c = 1.1$ mm was derived.

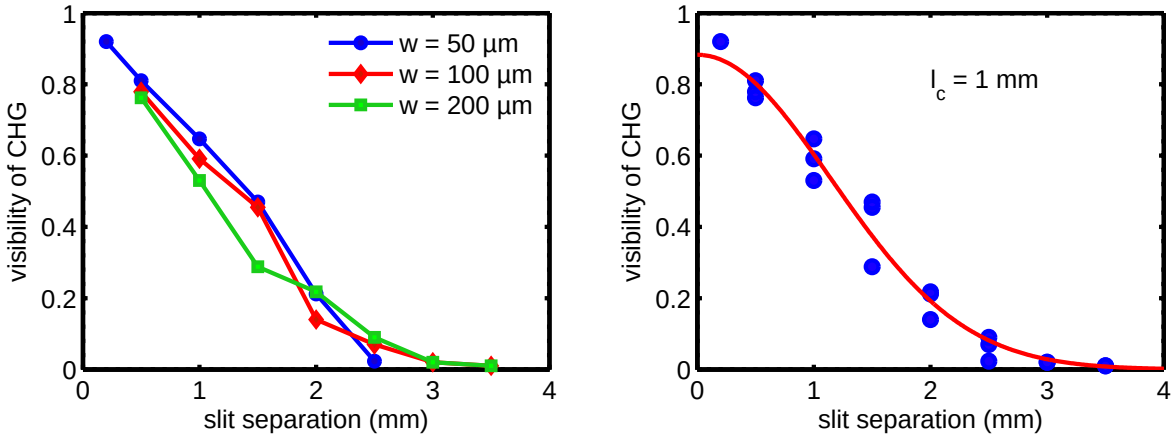

(a) (b)

Figure 5.26: The transverse coherence function of 200-nm CHG radiation (second harmonic), measured in the horizontal direction with three slit widths (a) and a Gaussian function fitted to the measured data (b).

Transverse coherence of the spontaneous emission (SE)

The transverse coherence of the 200-nm SE was investigated in dedicated measurements while no bandpass filters or coated mirrors were used. A longer exposure time of the order of 1 µs was needed to collect enough intensity, and 100 images were averaged. A background in the corner of each image was chosen and its averaged intensity was subtracted form the whole image. The visibility is found by using the maxima and minima at the center.

By turning the different parts (modulator, radiator, chicane) of the U250 on or off and tuning them, the transverse coherence was investigated under variation of path lengths in the undulator as well as K values (Figures 5.28 and 5.29). The spectral width of the undulator radiation is given by $\Delta\lambda = \lambda_0/N_\mathrm{u}$, where N_u is the number of the undulator periods. A larger N_u yields a more narrow spectrum, hence a larger temporal coherence length. Here, the modulator and the radiator each with 7 periods count as longer sections compared to the chicane which has only 3 periods.

The fit (red dashed curve) in all plots in Fig. 5.29 is the sum of a number of interference patterns calculated using wavelengths with rectangular distribution in the range of $(200\pm(\lambda_0/N_\mathrm{u}))$ nm. For fitting the undulator configuration, $N_\mathrm{u} = 6$ was used, and for fitting the OK configuration $N_\mathrm{u} = 12$ with $L = 2.5$ m, $w = 0.06$ mm and $d = 0.4$ mm.

Figures 5.28(a) and 5.29(a) show the fringe patterns and the intensity profile while the undulator was tuned to the optimum parameters of the optical klystron (OK) used for the coherent harmonic generation. The modulator was tuned to 400 nm, the chicane current was

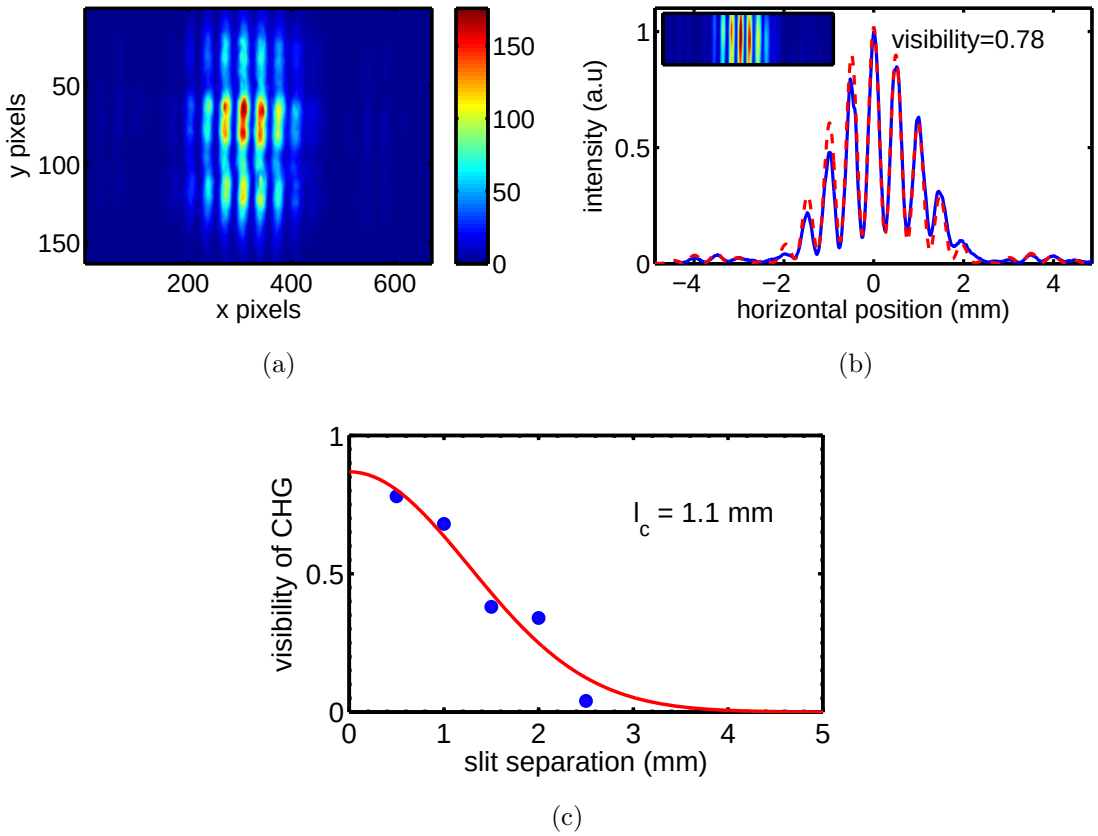

Figure 5.27: Interference pattern of 200-nm CHG radiation (the fourth harmonic of the 800-nm seed laser) using a slit width of 100 µm and a separation of $d = 0.5$ mm (a,b); the inset in figure (b) shows the ROI used for analyzing. The transverse coherence function measured in the horizontal direction is shown in (c). The blue dots are the measured data and the red curve is a Gaussian function.

about 280 A ($r_{56} \approx 25$ µm) and the radiator was at 200 nm. In this configuration, the SE has not only a high transverse coherence of 0.8, but also a higher temporal coherence length compared to the other configurations.
This large coherence time might be attributed to an interference between the three parts of the undulator U250 yielding a narrowband spectrum.
At a horizontal distance of about $x = 2.1$ mm from the central axis on the screen, the visibility of the fringes decreases to 0.4 (half of the central visibility). With $L = 2.5$ m and $d = 0.4$ mm, this distance corresponds to a wave arrival time difference of $\tau = x \cdot d/(L \cdot c) = 1.1$ fs at this point.

The fringes in Figs. 5.28(b) and 5.29(b) were measured while the whole U250 was tuned to the same resonance wavelength of 200 nm. The central visibility of 0.77 is relatively high, but decreases quickly off-axis, which is an indication of a low temporal coherence length.
The visibility of the fringes degrades to 0.3 at a horizontal distance of about $x = 1.6$ mm corresponding to a wave arrival time difference of $\tau = 0.85$ fs.

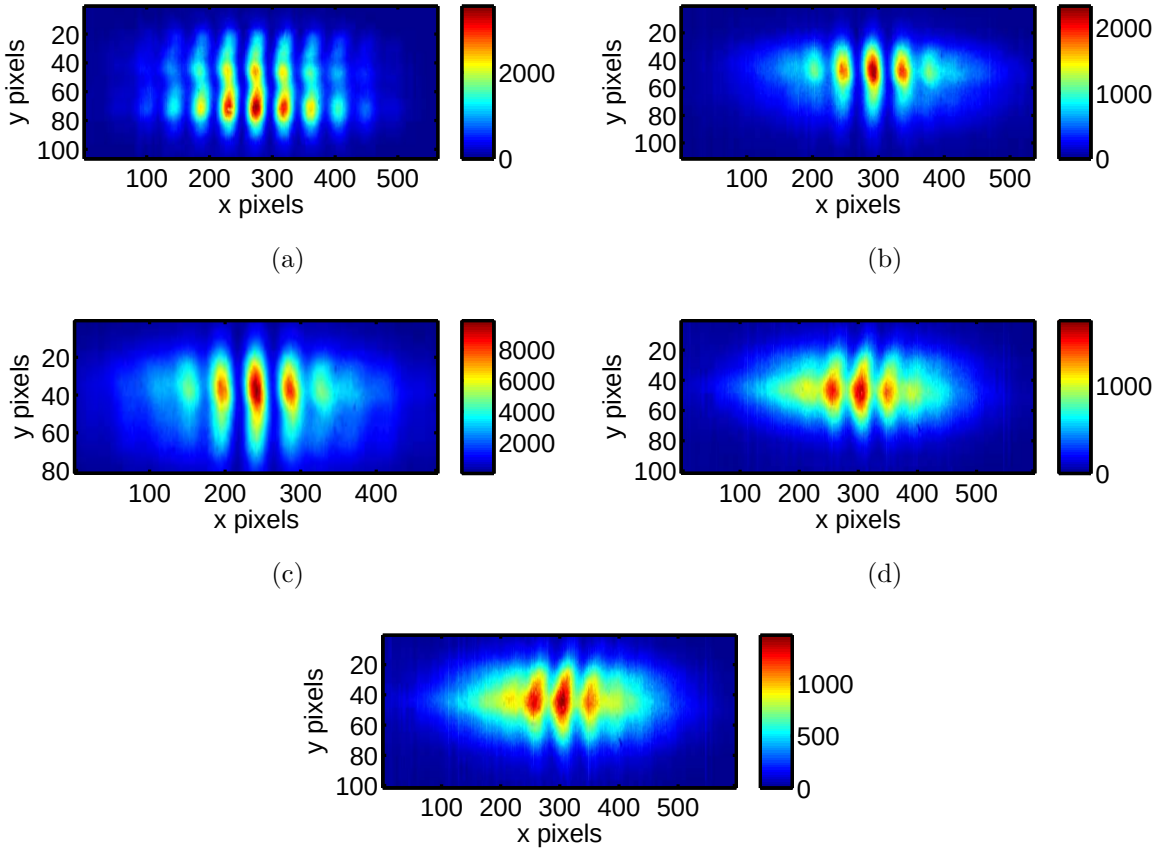

Figure 5.28: Fringe patterns of spontaneous emission in different configurations; a) CHG configuration (modulator at 400 nm, radiator at 200 nm, $r_{56} \approx 25$ µm), b) whole undulator at 200 nm, c) radiator and modulator at 200 nm, d) modulator and chicane at 200 nm, e) chicane at 15 µm. The ICCD camera was used with a pixel binning of 2×2. Further description in the text.

The fringe pattern and also the visibility does not change by turning the chicane in the above configuration off (Figures 5.28(c) and 5.29(c)). The presence of the chicane has an effect on the temporal coherence only when it is tuned to its optimum value, satisfying the effective bunching condition.
By turning both of the long sections (radiator and modulator) off, the visibility reduces to 0.3 (figures 5.29(e) and 5.28(e)), and it does not get much higher by turning one of the long sections (modulator) on (Figures 5.29(d) and 5.29(d)).

According to this measurement, it can be concluded that a high coherence can be obtained by increasing the length of the undualtor (by turning both long sections i.e., modulator and radiator on). While using the CHG configuration, both the temporal and transverse coherence are highest, using the radiator (or even the radiator with chicane), visibility is the lowest.

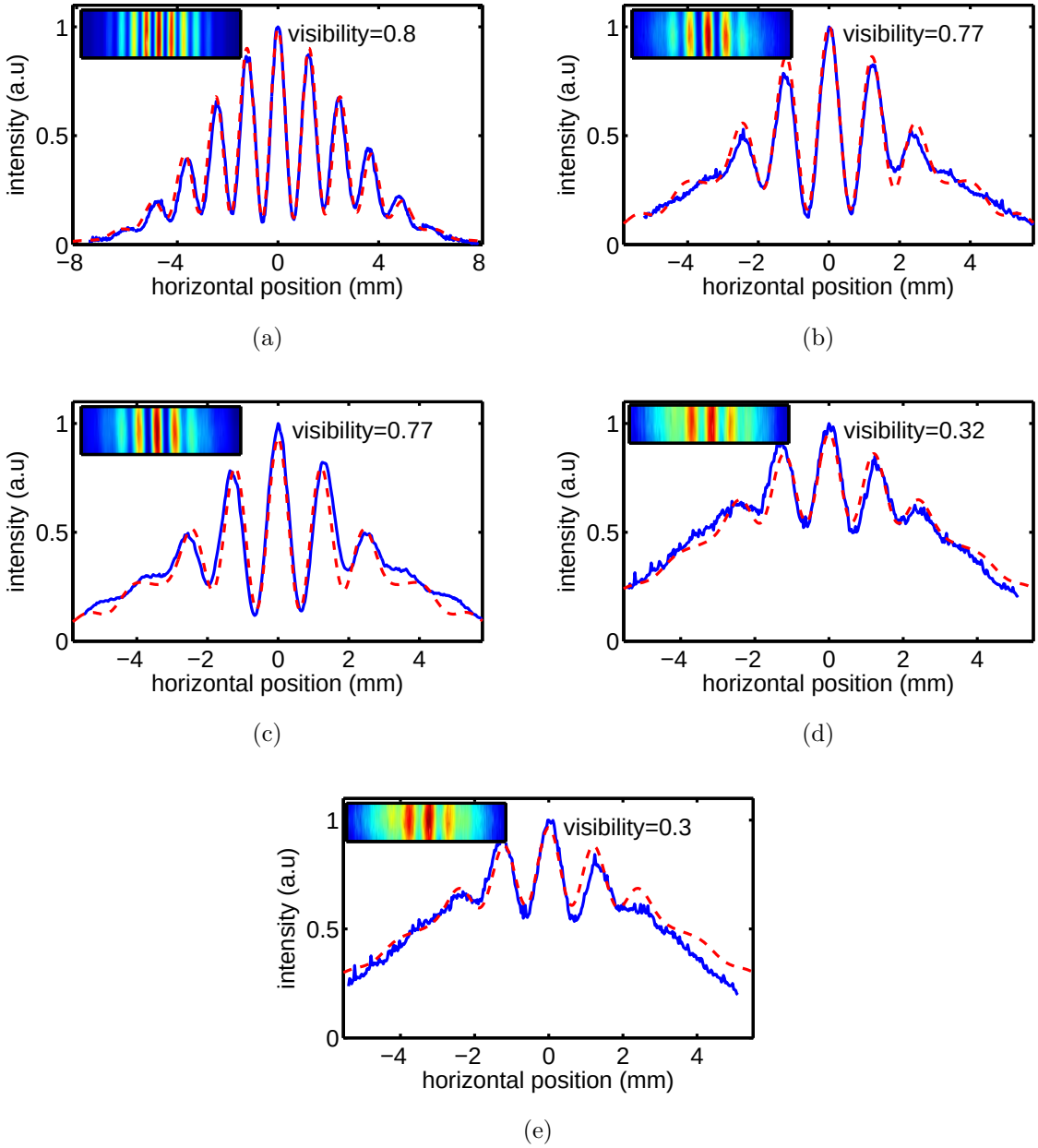

Figure 5.29: Intensity profile of the ROI in the interference pattern of the spontaneous emission in different configurations; a) CHG configuration (modulator at 400 nm, radiator at 200 nm, $r_{56} \approx 25$ µm), b) whole undulator at 200 nm, c) radiator and modulator at 200 nm, d) modulator and chicane at 200 nm, e) chicane at 15 µm; all measured without bandpass filter. The inset shows the ROI in the fringe patterns used for analyzing. The blue curves are the measured data and the red dashed curves are fits.

The transverse coherence was measured for the entire U250 tuned to several K values. The visibility was $V = 0.77$ for $K = 4.86$, and $V = 0.33$ for K values of 2.7, 3.7 and 5.7. For $K = 7.1$ the visibility was 0.35. Varying the K value did not affect the transverse coherence significantly.

Furthermore, the transverse coherence of 200-nm SE was measured by using a bandpass (BP) filter (FWHM of 10 nm), while the undulator was in optical-klystron configuration (Fig. 5.30(a)), and while the whole undulator was tuned to a K value of 4.86 (resonance wavelength of 200 nm) (Fig. 5.30(b)) with $L = 0.97$ m, $w = 0.06$ mm and $d = 0.4$ mm. Because of the absorption in the BP filter, an exposure time of 10-10^2 µs was needed, which is much larger than before.
It can be seen that with using a filter and reducing the spectral bandwidth, the visibility decay along the horizontal axis is not so fast as before due to the increased temporal coherence. The fits in both of these figures were performed assuming a constant visibility. The effect of the spectral width can be easily seen by comparing figures 5.30(b) and 5.30(a) with 5.29(b) and 5.29(a).

By increasing the exposure time, the second and even the third maxima of the sinc-function

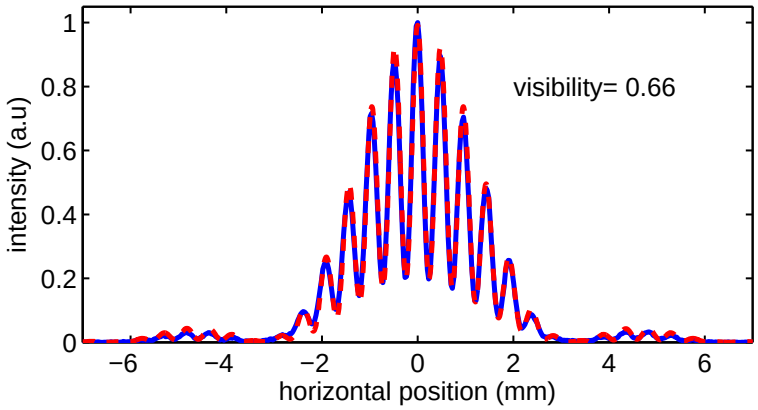

(a)

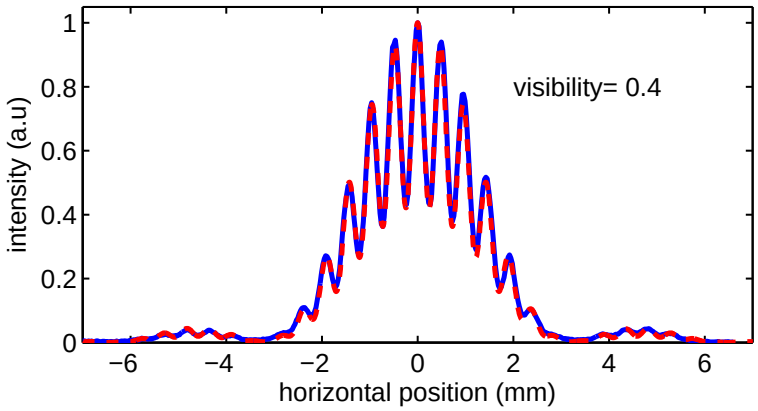

(b)

Figure 5.30: Intensity profile of the spontaneous emission using a bandpass filter (FWHM of 10 nm), while the undulator was in optical-klystron configuration (a), and while the whole undulator was tuned to a K value of 4.86, corresponding to a wavelength of 200 nm (b).

can be resolved (Fig. 5.30). At the center of the second maximum (at about $x = 5$ mm), typical values of $V = 0.4$ were measured for the CHG configuration and $V = 0.26$ when the whole undulator was at 200 nm.
At $x = 5$ mm, where the visibility is approximately half of the central visibility, the delay between the waves from two slits is $\delta l = d \cdot x/L = 2.1 \times 10^{-6}$ m, corresponding to 7 fs. This value is close to the coherence time of a Gaussian-shaped radiation with 10 nm (FWHM) bandwidth, which is equal to 8.8 fs.

In addition, the transverse coherence of the Ti:sapphire laser was measured (Fig. 5.31). With $w = 0.05$ mm, $d = 0.5$ mm and $L = 1.26$ m, and a distance of about 30 meters away from the laser system, the fringe visibility was about 0.91. The fringe patterns of the Ti:sapphire laser is shown in Fig. 5.31.

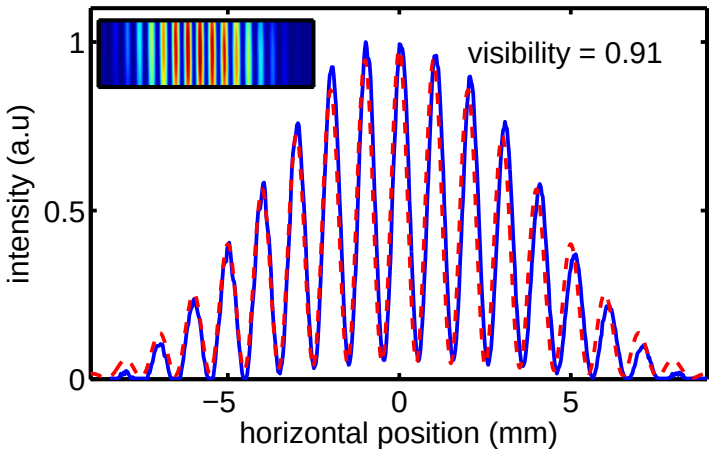

(a)

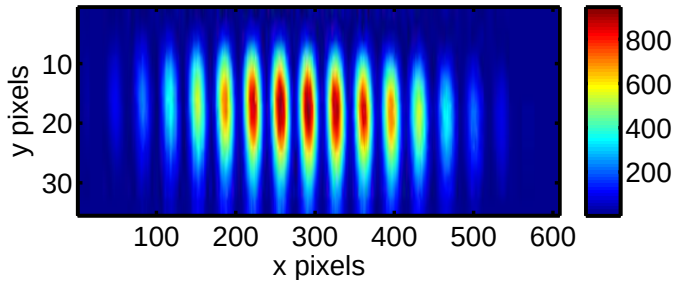

(b)

Figure 5.31: Fringe pattern of the Ti:sapphire laser pulses measured at a distance of about 30 meters away from the laser system.

5.6.2 Longitudinal coherence

The temporal coherence length (coherence time) of 200-nm CHG pulses was studied both with a Michelson interferometer and by introducing two movable non-coated fused silica wedges in front of each slit of the double-slit setup (Fig. 5.32). A bandpass filter (10 nm FWHM) was placed right before the camera to eliminate the seed laser light, reducing the bandwidth of the SE but not affecting the CHG bandwidth, which is about 1.5%. The coherence time is determined by the shape and the bandwidth of the spectrum, while the transverse coherence length is determined mainly by the source size and divergence. However, these two also depend on each other [112, 113].

Measurements using double-slits followed by wedges

A photo and sketch of two non-coated fused silica wedges in front of each slit of the double-slit is shown in Fig. 5.32. The vertical position of one of the wedges was varied (Δy) using a micrometer stage. Thus, the optical path length of one beam with respect to the other was varied by $\Delta z = (n_\mathrm{f} - 1)\Delta y \tan\theta$ (wedge angle $\theta = 4°$, refractive index $n_\mathrm{f} = 1.55$ at 200 nm), giving a time delay of $\tau = \Delta z/c$ between the two beams.

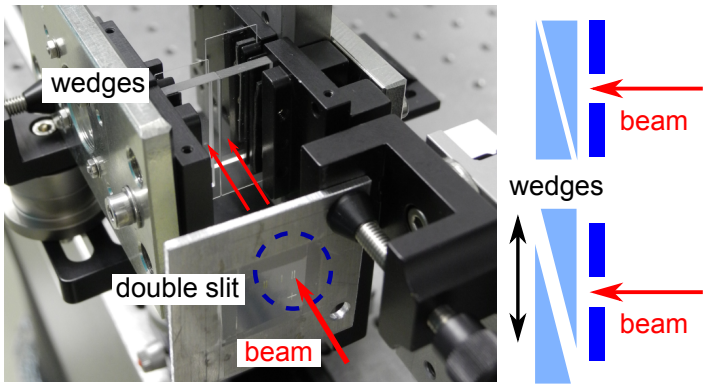

Figure 5.32: Photo and sketch of the double-slit setup followed by fused-silica wedges.

In Fig. 5.33, example interference patterns are shown for zero, medium and maximum time delay using slits of width $w = 100$ µm, separation $d = 0.5$ mm, length of $l = 2$ mm, and a distance of about $L = 1.3$ m between slits and camera. On the right side of the figure, the 2D fast Fourier transformation (FFT) of the interference patterns is shown. In Fourier space, the amplitude of the side peak corresponds to the cross-correlation of the two beams (XC) [111], and the amplitude at the center corresponds to the autocorrelation of the beams (AC). The coherence function $\gamma(\tau)$ and coherence time τ_c can be derived by [111]

$$\gamma(\tau) = \frac{\tilde{I}_\mathrm{XC}}{\tilde{I}_\mathrm{AC}}\,, \quad g(\tau) = \frac{\gamma(\tau)}{\gamma(0)}\,, \quad \tau_\mathrm{c} = \int_{-\infty}^{\infty} |g(\tau)|^2\,\mathrm{d}\tau, \tag{5.7}$$

where $\tilde{I}_{\mathrm{XC}}$ and $\tilde{I}_{\mathrm{AC}}$ are the mean values of the intensity in small ROIs around the side and central peaks in the frequency domain. At a large delay, at which the interference pattern smears totally out, $\tilde{I}_{\mathrm{XC}}$ has still a small non-zero value. Therefore, the linear interpolation of the two outermost τ values of $\tilde{I}_{\mathrm{XC}}$ was subtracted from $\tilde{I}_{\mathrm{XC}}$ at each delay, and an averaged background from the corners of each image was subtracted from each $\tilde{I}_{\mathrm{AC}}$ value. Examples of measured temporal coherence functions of 200-nm CHG and SE pulses are shown in Fig. 5.34, giving a coherence time of about 34 fs for CHG and 9.5 fs for SE.

The CHG spectrum at this measurement is shown in Fig. 5.41(b) with $\lambda_0 = 198.9$ nm and a FWHM width of $\Delta\lambda = 1.6$ nm. If the spectrum was perfectly Gaussian, the theoretical coherence time would be $\tau_{\mathrm{c}} = 0.66\lambda_0^2/(c\Delta\lambda) = 54$ fs, which is longer than the measured value. The reason of this discrepancy is the slight deviation of the CHG spectrum from a perfect Gaussian shape (as can be seen in in Fig. 5.41(b)), which can change the theoretical value of the coherence time significantly. A Lorentzian function fits better to the slope of the spectrum at higher wavelengths rather than a Gaussian one. Assuming a perfectly Lorentzian shaped spectrum, the coherence time would amount to about $\tau_{\mathrm{c}} = \lambda_0^2/(\pi c\Delta\lambda) = 26$ fs. In fact, the CHG spectrum is between the Gaussian and Lorentzian, and the measured coherence time of

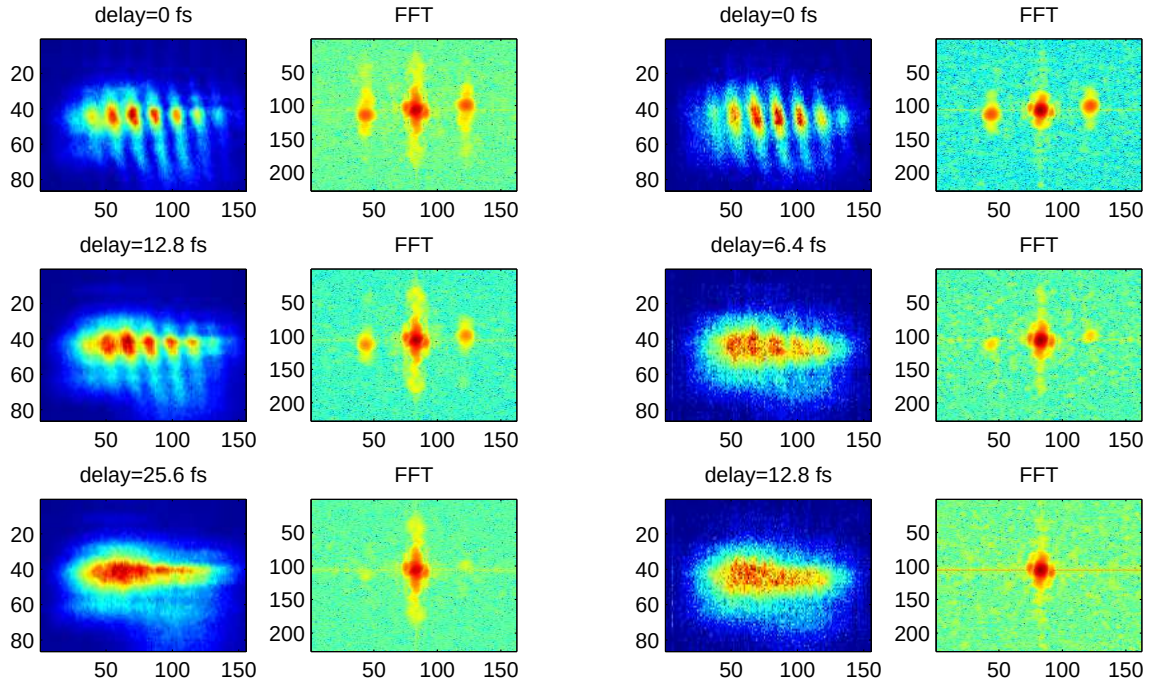

(a) (b)

Figure 5.33: Interference patterns obtained using a double-slit followed by wedges at different delays. a) Interference pattern of the CHG radiation (left) and its FFT (right). b) Interference pattern of the SE (left) and its FFT (right).

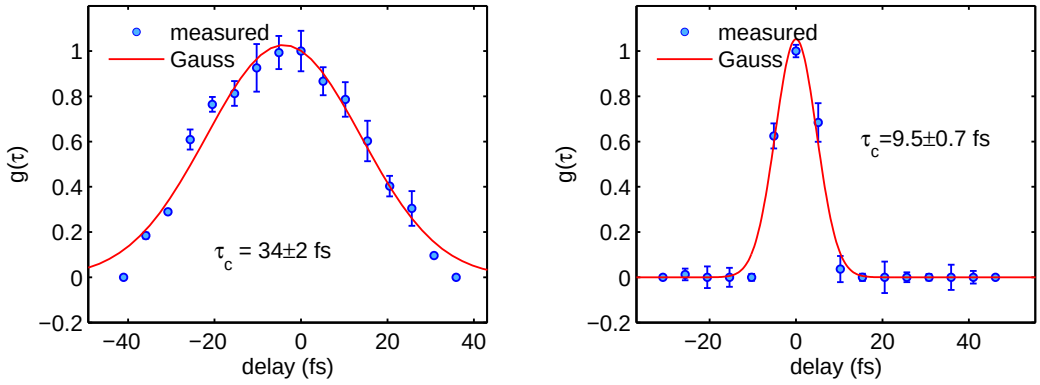

(a) (b)

Figure 5.34: Coherence time of the CHG (a) and SE pulses (b) measured with double-slits followed by wedges. The blue dots are the measured data, the red curves are Gaussian fits.

34 fs is also between the theoretical coherence time of a Gaussian and Lorentzian shaped spectrum.

The coherence time measurement was repeated for different slit dimensions to investigate the effect of the transverse beam extension on the temporal coherence length. The results are summarized in Table 9. No clear correlation was found between the slit dimension and the measured coherence time.

The measured coherence time of SE was about (9±1) fs, using different slit configurations. With a Gaussian shape at a central wavelength of $\lambda_0 = 200$ nm and a FWHM width of $\Delta\lambda = 10$ nm (given by bandpass filter), the theoretical coherence time of SE is $\tau_c = 0.66\lambda_0^2/\Delta\lambda = 8.8$ fs, matching the measured value.

Table 9: Measured and calculated coherence time of CHG using different slit dimension.

w (µm)	d (mm)	l (mm)	$\tau_{c,meas.}$(fs)	$\Delta\lambda/\lambda_0$	$\tau_{c,cal.}$ (fs)
200	1.0	2	34±2	1.61/198.90	54
200	1.0	1	32±1	1.61/198.90	54
200	1.5	1	31±2	1.61/198.90	54

In a separate measurement, the coherence time was studied by varying the r_{56} value of the chicane, while its optimum was 39 µm. A slit width of $w = 100$ µm and separation of $d = 0.5$ mm was used. The results are summarized in Table 10. In this measurement range, there is no significant correlation between the chicane r_{56} value and the measured coherence time.

Table 10: Measured and calculated coherence time of CHG under variation of the r_{56} value of the chicane.

r_{56} (µm)	$\tau_{c,meas.}$(fs)	$\Delta\lambda/\lambda_0$	$\tau_{c,cal.}$ (fs)
22	26±1	-	-
39	23±4	2.63/202.93	34
66	24±1	-	-

Measurements using the Michelson interferometer

The setup of the Michelson interferometer is shown in Fig. 5.35. A 2-mm thick fused-silica beamsplitter with a special coating for 200 nm was used to divide the radiation intensity into two equal parts. A nanometer positioning stage was used to delay the beams with respect to each other (PX 400 SG with controller NV 40/1 CLE [114]). The total travel range of the stage is 400 µm in open-loop and 320 µm in closed-loop operation with a resolution of 8 nm in both operating modes. Additionally, the stage was mounted on a manual micrometer stage for longer distances. Operation in closed loop was not used, because the fringes smeared and disappeared due to oscillations of the stage feedback system. Therefore, the measurements were performed in open-loop mode, in which the position of the stage is proportional to a monitored voltage ranging from -3 V to 10 V. The linearity and the travel range of the stage was verified roughly by using a dial gauge.

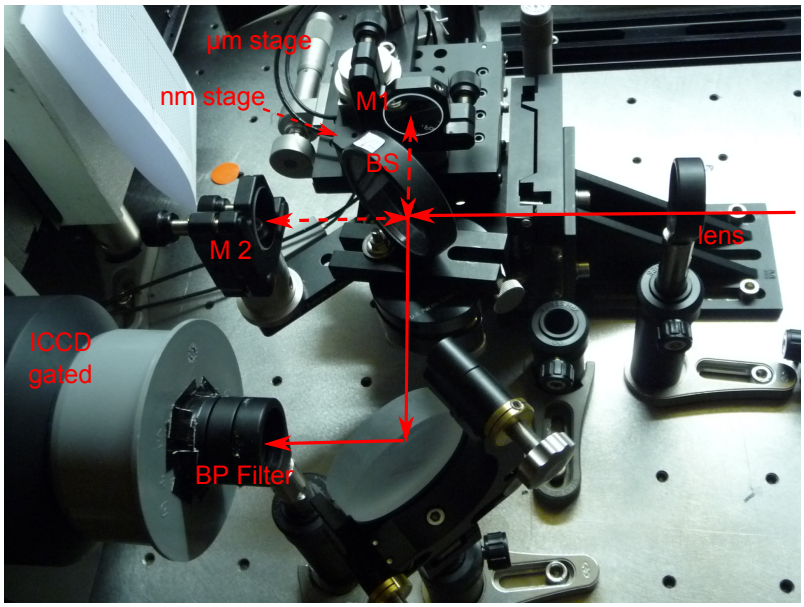

Figure 5.35: Setup of the Michelson interferometer to measure the temporal coherence length, including a lens, a beamsplitter, two adjusting mirrors, a nm stage, a µm stage and an ICCD camera.

An example interference pattern of 200-nm CHG pulses, the fourth harmonic of the 800-nm

seed laser, is shown in Fig. 5.36. The exposure time of the camera was set to 200 ns, ensuring that only one CHG pulse and one SE background pulse were recorded, albeit with on-chip integration of 20 or 100 images to get enough counts. The results were the same for both cases, except that with a lower number of accumulated images the error bars were larger. All measurements were done in single-bunch mode. The maximum CHG-to-SE ratio was about 50.

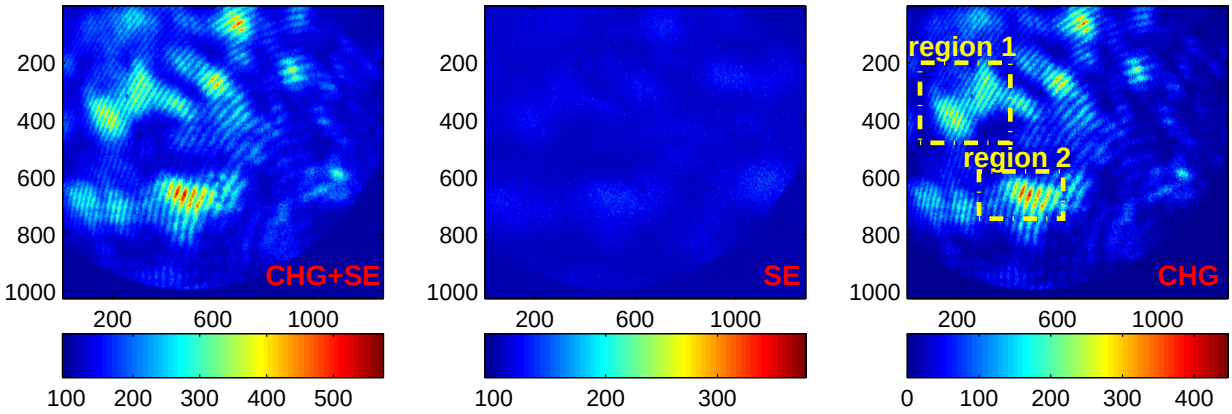

Figure 5.36: Interference fringe patterns of the Michelson interfermometer. The total radiation including both CHG and SE radiation (left), SE radiation (center) and the net CHG radiation by subtracting the previous plots from each other (right). Both axes of these plots are pixel numbers of the camera. Two regions in the pattern, marked as regions 1 and 2, were chosen for the analysis of the visibility of the fringes.

Due to the damaged in-vacuum mirror in BL 4 (see Section 5.6), the spatial profile of the CHG radiation and hence the interference pattern was not uniform. Two regions in the pattern were used to analyze the visibility of the fringes, marked as regions 1 and 2. The fringe patterns for the two regions and their Fourier transform are shown in Fig. 5.37 for zero, medium and maximum delay. In zero delay, the visibility is largest, whereas in maximum delay no more fringes are visible.

The cross-correlation and autocorrelation terms in Fourier space are marked as XC and AC, respectively. The coherence function is derived by dividing the mean value of the intensity in the XC region by the mean value in the AC region. For each delay, 50 images were recorded, and the value of the coherence function was averaged and normalized by its maximum. The measured normalized coherence functions for both regions 1 and 2 are shown in Fig. 5.38. Error bars denote the standard deviation of the visibility from 50 images at each delay point. Region 1 yields a coherence time of about 155 fs, region 2 about 118 fs, much larger than expected.

The spectrum of the CHG radiation in this measurement was measured using the Czery-

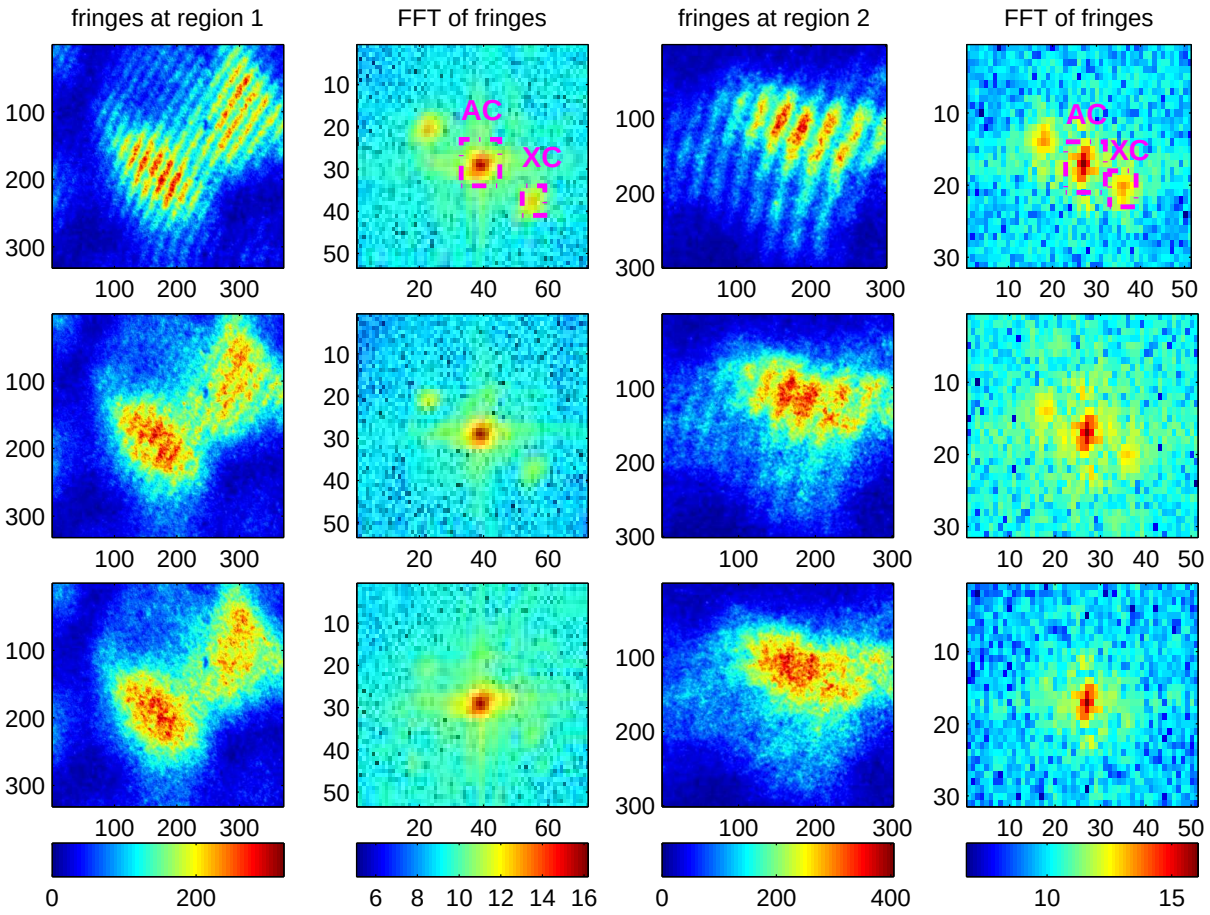

Figure 5.37: Fringe patterns of 200-nm CHG pulses (the 4$^{\text{th}}$ harmonic of the 800-nm seed laser) at two different regions in the beam spot and their Fourier transforms for zero, mean and maximum delay (top to bottom). Maximum visibility occurs at zero delay, and zero visibility at maximum delay. The cross-correlation and autocorrelation terms are marked as XC and AC, respectively in the FFT pattern. The coherence function is derived as the ratio of the mean intensity values of the XC region and the AC region.

Turner monochromator and APD, and analyzed with two different functions (Fig. 5.39). The shape of the spectrum is neither perfectly Gaussian nor Lorentzian. Assuming a Gaussian shape, a FWHM temporal coherence length of $\tau_c = 0.66\lambda^2/(c\Delta\lambda) \sim 46$ fs is derived and assuming a Lorentzian shape, $\tau_c = \lambda^2/(\pi c\Delta\lambda)$ is 24 fs.

The reason for the discrepancy between the calculated values and the measurement could be tracked down to the chirp which occurs in the beamsplitter of the Michelson interferometer while no compensation plate was used. As one beam passes through the beamsplitter once, the other passes three times, yielding a 4-mm path length difference through the material, and therefore a non-equal chirp in the two arms of the Michelson interferometer.

The coherence length of the 200-nm CHG pulses was also measured while seeding with

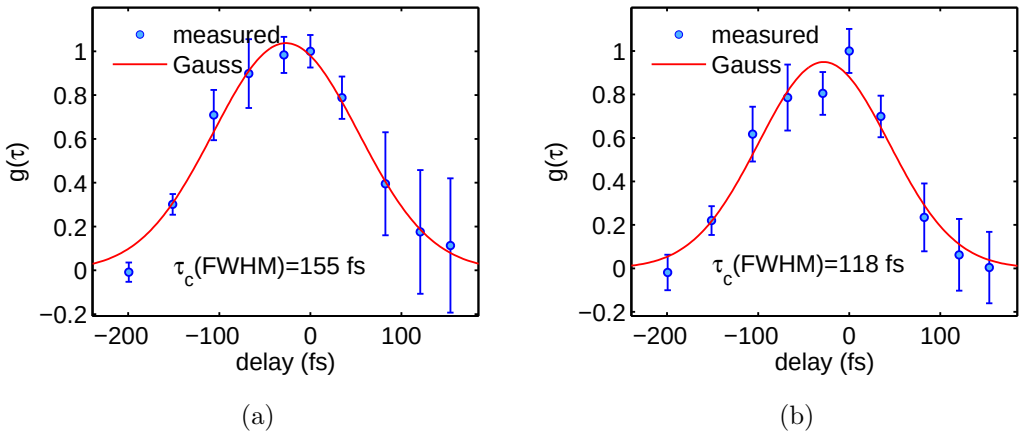

(a) (b)

Figure 5.38: Normalized coherence function of 200-nm CHG radiation (4^{th} harmonic of 800-nm seed laser), measured using a Michelson interferometer for region 1 (a) and region 2 (b) with a temporal coherence length of about 150 fs and 120 fs, respectively.

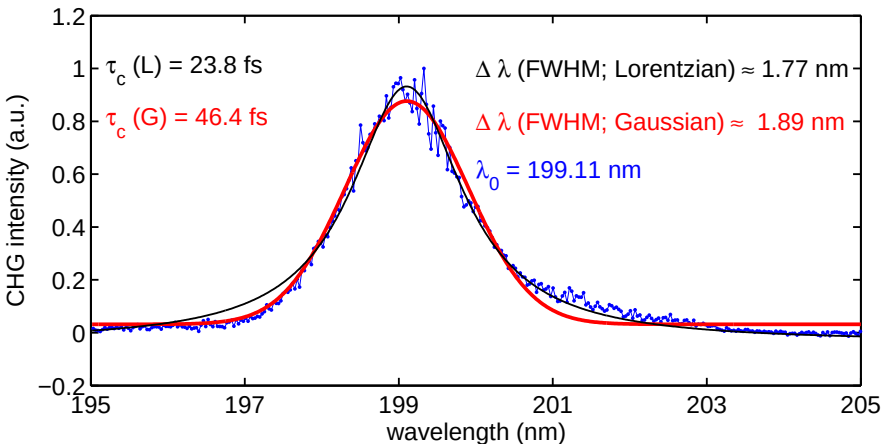

Figure 5.39: Spectrum of 200-nm CHG pulses, the 4^{th} harmonic of the 800-nm seed laser. The blue curve is the measured data, the red curve is a Gaussian fit, and the black curve is a Lorentzian fit.

400 nm. The fringe patterns are shown for two different measurements in Fig. 5.40, in which the distance between the fringes were noticeably varied by moving the lens and the mirrors and moving from the center of the circular fringes towards the edges. The measured coherence function and spectrum is shown in Fig. 5.41. This measurement was done without compensation plate, and yielded unrealistically high values ($\tau_c = 135$ fs).

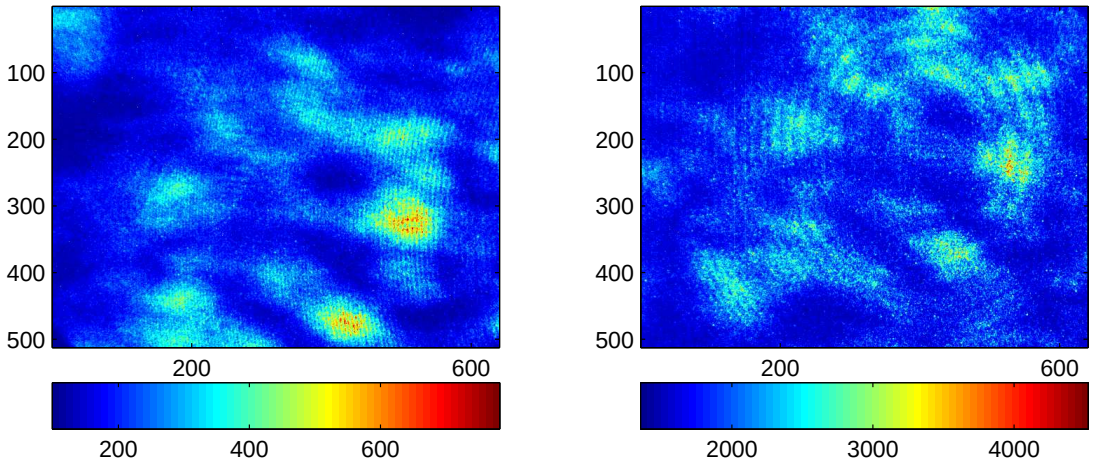

Figure 5.40: Michelson interference fringe patterns of 200-nm CHG radiation (second harmonic of 400-nm seed laser). Both axes of these plots are pixel numbers of the camera with a pixel size of 6.7×6.7 µm^2.

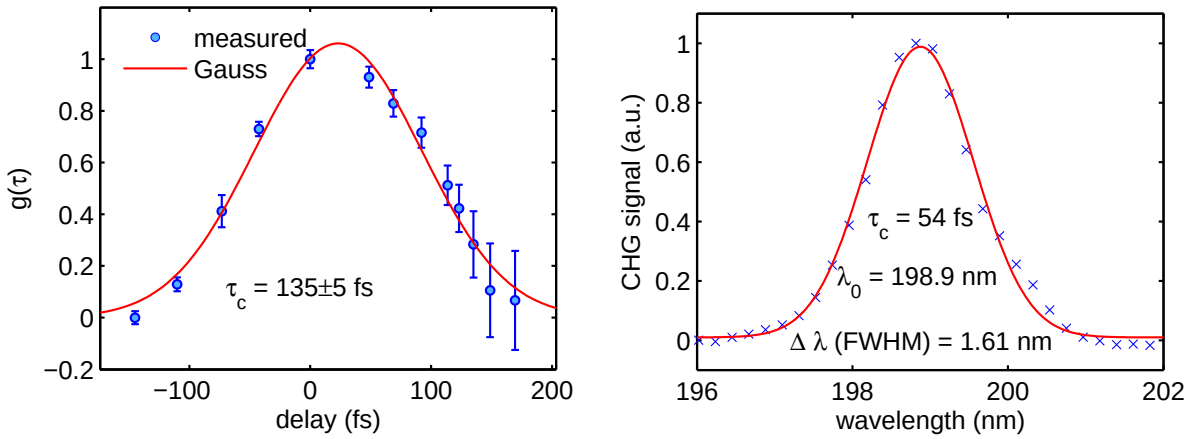

(a) (b)

Figure 5.41: Normalized coherence function $g(\tau)$ of 200-nm CHG radiation (second harmonic of 400-nm seed laser) measured by Michelson interferometer with Gaussian fit (a) and spectrum of CHG radiation with Gaussian fit (b). Both are measured at $r_{56} = 37$ µm. The error bars are the standard deviation of the fringe visibility for 50 measurements at each delay point.

The coherence time of 200-nm CHG pulses (2$^{\text{nd}}$ harmonic) was measured again after placing a 2-mm thick fused-silica window next to the coated side of the beamsplitter which is as thick as the beamsplitter and parallel to it, in order to compensate the material difference between the two arms. Furthermore, the damaged in-vacuum 45° mirror in BL 4 was exchanged by a new mirror. As shown in Fig. 5.42, the quality of the fringes was improved, and a shorter coherence time of about 33 fs was obtained, close to the expected value. This measurement

was performed while the chicane was tuned to a larger r_{56} value compared to the optimum value for CHG. The CHG spectrum is not Gaussian, therefore the coherence time cannot be calculated using the simple analytic formula for a Gaussian beam.

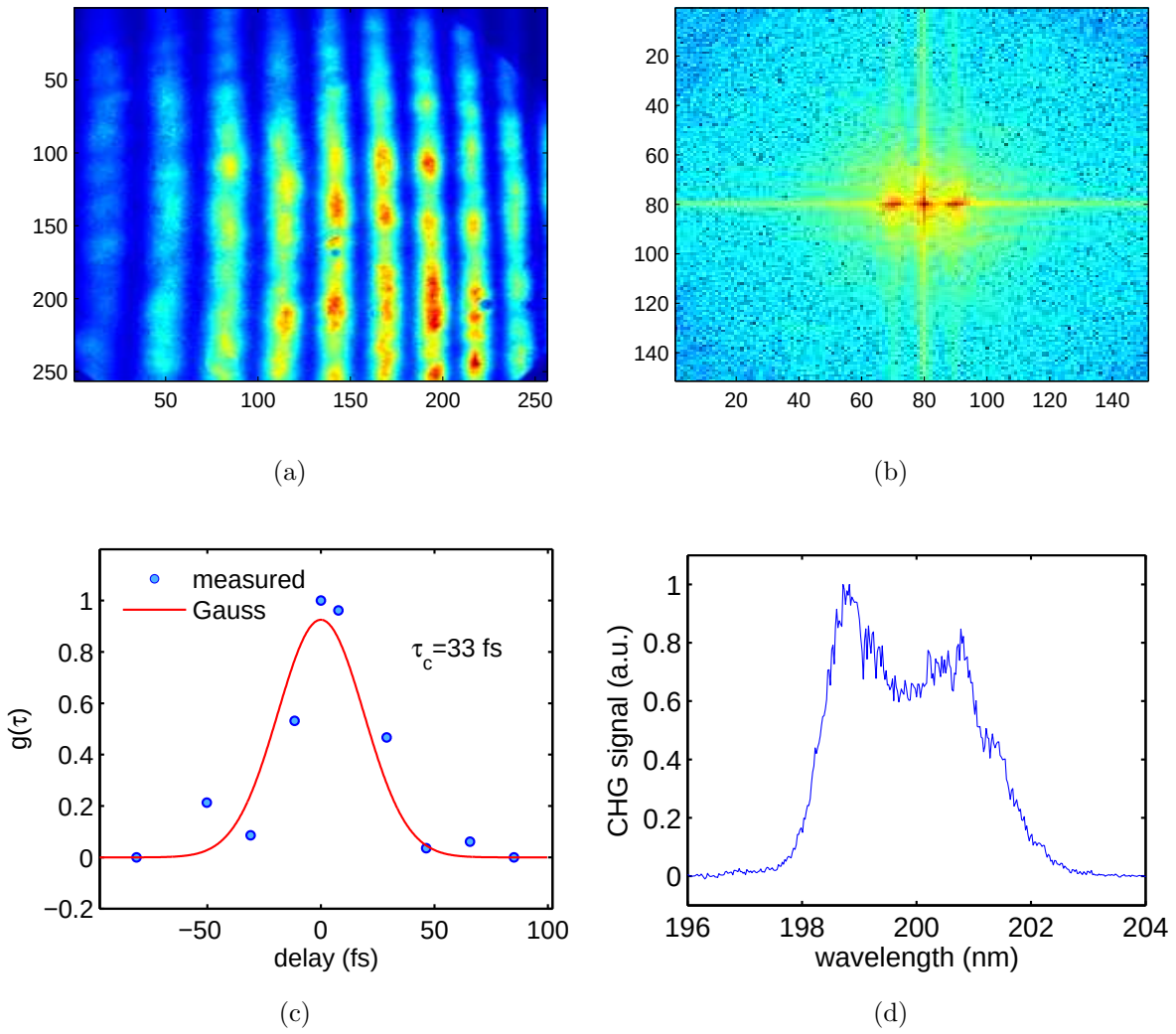

Figure 5.42: Interference pattern at zero delay (a) and its Fourier transform (b). Temporal coherence function (c) and spectrum of 200-nm CHG radiation (d). The measurements were done while using a compensation plate in the Michelson interferometer.

5.6.3 CHG coherence versus chicane strength

The temporal coherence of CHG radiation is associated with the microbunching in the chicane. The microbunching of electrons in the chicane increases the temporal coherence.

Transverse coherence

The transverse coherence of 200-nm CHG radiation was measured while varying the chicane strength. This measurement was performed using a double-slit with a slit separation

of 500 µm and a slit width of 100 µm. The fringe patterns were analyzed using the Fourier transformation as well as finding the central visibilities. An example of an interference pattern and the transverse coherence versus r_{56} is shown in Fig. 5.43.

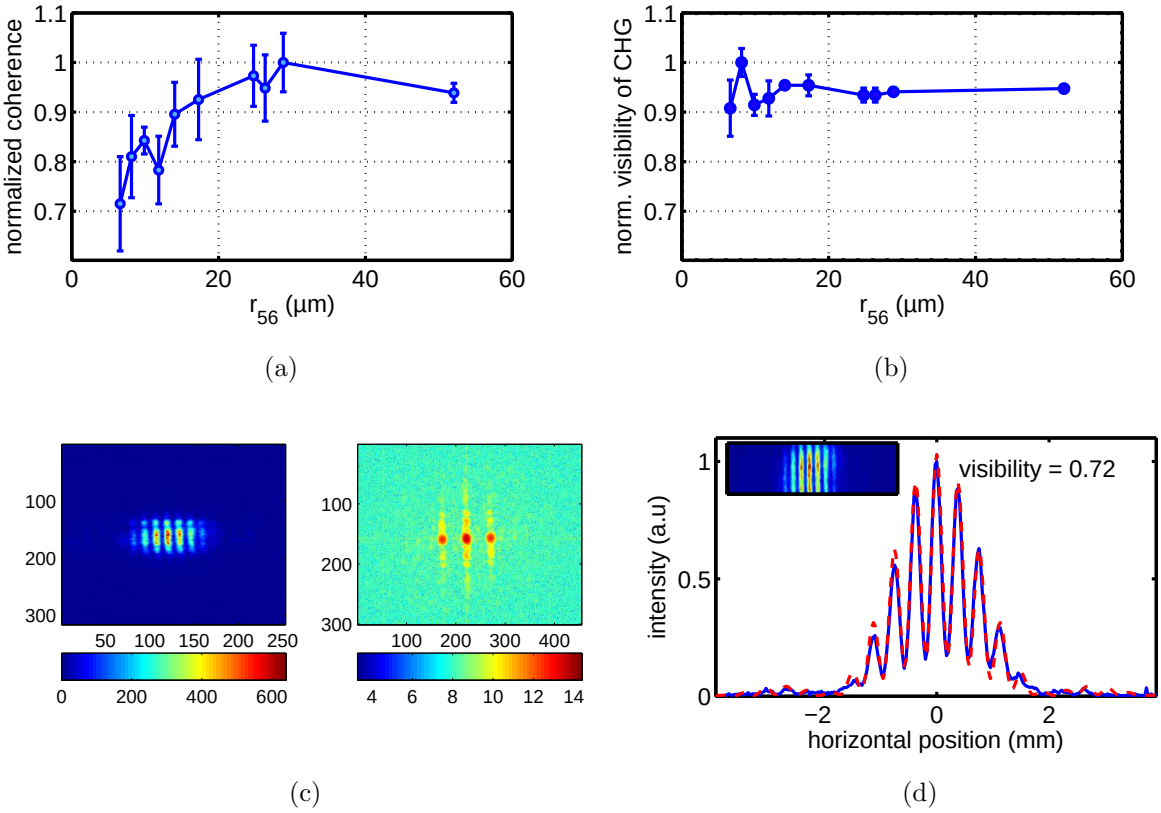

Figure 5.43: Normalized coherence of the CHG radiation versus r_{56} value of the chicane analyzed by using Fourier transformation (a), and by finding the central visibilities (b). Example interference fringe pattern at $r_{56} = 29$ µm (c, left), its Fourier transform (c, right), and its intensity profile across the region shown in the inset (d).

The central visibility does not change by varying the chicane strength (Fig. 5.43(b)). However, when using the FFT method, the coherence shows a trend similar to CHG intensity; the optimum chicane value here was about 29 µm, at which the CHG-to-SE intensity ratio was highest.

By decreasing the r_{56} value to about 30 % of its optimum, coherence decreases to 70 % of its maximum value. Increasing the r_{56} value by about 70 % of its optimum degrades the coherence by about 10 % (Fig. 5.43(a)).

This effect can be explained by the fact that the Fourier transformation is applied to the whole image including the off-axis fringes, hence including the effect of the temporal coherence (see beginning of Section 5.6.1).

Temporal coherence

The dependence of the temporal coherence of the 200-nm CHG radiation on the chicane strength was studied by using the Michelson interferometer at zero delay. An example interference pattern and the scan of the temporal coherence versus r_{56} are shown in Fig. 5.44.

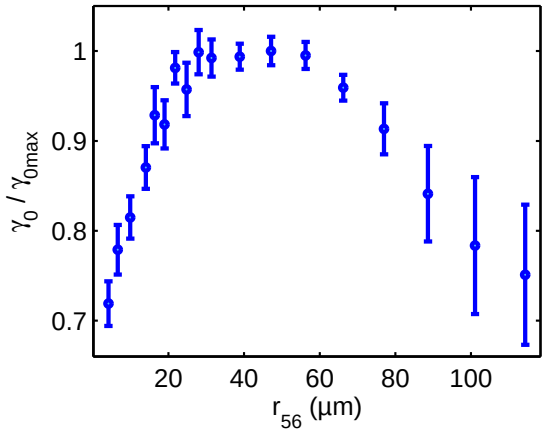

(a)

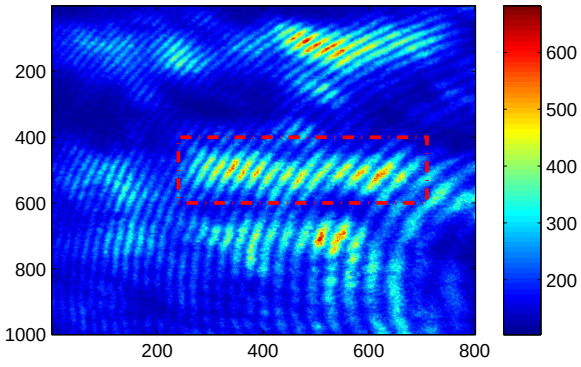

(b)

Figure 5.44: An example interference pattern of the 200-nm CHG pulses (a), and the temporal coherence at zero delay γ_0 versus r_{56}, normalize to the maximum value $\gamma_{0,\max}$ (b).

It can be seen that at an optimum chicane value, at which the bunching factor is highest, the maximum visibility is detected.

6 Summary and Outlook

Pump-probe experiments to study ultrafast dynamic phenomena require two short pulses and a good control of the time delay between them. A short-pulse facility based on coherent harmonic generation (CHG) has been commissioned at the DELTA storage ring since 2011. In 2013, the CHG performance was dramatically improved by modifying the central poles of the undulator U250 which act as a chicane (between modulator and radiator) for microbunching. At DELTA, CHG is mostly conducted with a single bunch in the storage ring, but was also demonstrated in user operation with a hybrid fill pattern, comprising a 3/4-circumference multi-bunch fill and a single bunch of higher charge.
In the frame of this dissertation, the CHG pulses were characterized and the preparations for pump-probe experiments were accomplished, including the construction and commissioning of a pump-pulse beamline to guide the laser pulses.

6.1 Preparation of pump-probe experiments

An evacuated beamline has been designed, constructed and commissioned successfully to guide about 10% of the laser power (0.8 W) over a distance of about 53 m to the experimental station of a VUV beamline (BL 5). Pump pulses have been focused on the sample and temporally overlapped with the seed-laser pulses.
The size of the beam on the sample can be finely tuned moving a curved mirror on a micrometer stage in the new optics hutch near the experimental station.
The position of the beam has been stabilized using a commercial optical feedback system. While the position of the beam on both detectors of the feedback system shows a remaining rms fluctuation of 26 µm, the stability on the sample will be slightly worse due to four further mirrors and one lens in the remaining six meters of the beamline between detectors and sample.
The GDD in the whole beamline has been estimated to be about 1550 fs^2, which for a Gaussian pulse with an initial duration of 40 fs yields a pulse duration of about 115 fs at the sample. This pulse duration is small enough to study the demagnetization of ferromagnetic materials as planned, as the process of demagnetization and remagnetization takes place in the few-ps range depending on the pump fluences [96]. However, the temporal resolution is limited by the duration of the probe pulses, which is currently lengthened by the monochromator in the VUV beamline to about 5 ps but can be reduced to a few hundred fs.
The energy fluence required to demagnetize a ferromagnetic material was estimated to be about 1 to 10 mJ/cm^2 [93–96]. This energy can be achieved by focusing the pump pulses to a $1/e^2$ diameter of about 5 mm.

Furthermore, the CHG pulses were detected using a delay-line detector in the VUV beamline measuring the photoelectron count from Au and Cu samples. A LiF filter was used that blocks the large background of the high-harmonic spontaneous emission (SE) radiation (below 105 nm) from the undulator. Down to 133 nm, the CHG-to-SE ratio was high enough (of the order of 10 to 100) to be used for pump-probe experiments with reasonable measurement durations. While creating photoelectrons with pulses of shorter wavelengths, this filter has to be removed yielding a CHG-to-SE ratio of a few percent at 100 nm and 80 nm.

The preparations for pump-probe photoemission experiments are nearly completed. The first experiment will be presumably performed on a magnetic system Co/Cu. The goal is to use the magnetic linear dichroism (MLD) effect in order to study the demagnetization dynamics in this thin-film system [97].

6.2 Characterization of CHG pulses

The angular distribution of the SE and CHG pulse was investigated. The measured width of the 200-nm CHG radiation profile was about 0.65 mrad (FWHM) in the horizontal direction and 0.85 mrad (FWHM) in the vertical direction measured at a distance of about 10 meters away from the radiator, consistent with the measurements using a fast-gated intensified CCD (ICCD) camera. The width of the 400-nm CHG radiation profile was about 1 mrad (FWHM) measured using an ICCD camera at a distance of about 12 meters from the radiator.

The CHG spectrum was measured using different instruments and methods, a CCD spectrometer, a Czerny-Turner spectrometer followed by a PMT or APD, and measuring the photoelectron yield under variation of the PGM wavelength in the VUV beamline. The results are consistent and exhibit a nearly Fourier-transform limited bandwidth. The bandwidth of the CHG radiation was about 1.5% at 200 nm and 1.2% at 133 nm.
When the r_{56} value of the magnetic chicane was tuned to a value higher than its optimum value, an interference pattern was observed in the CHG spectrum. The reason is interference between the radiation from the multi-peaks created in the electron density distribution due to overbunching.
The dependence of the CHG wavelength and bandwidth on undulator K value and laser wavelength was investigated. The central wavelength of the CHG radiation is determined by the laser wavelength rather than the undulator wavelength due to its small bandwidth compared to the $\sim 14\%$ bandwidth of the undulator. The microbunches act like a narrow-band amplifier on the broad undulator spectrum.

The observed CHG-to-SE ratios vary from 0 to a few 100, yielding maximum ratios of the peak power close to 10^6. The CHG pulse energy was estimated using the measured SE power and its relation to CHG power, to about 5 nJ and 0.2 nJ at 1.5% bandwidth for the 400 and 200 nm CHG radiation, respectively.

The energy modulation was estimated by measuring the CHG intensity while increasing the r_{56} value of the chicane from 0 to 100 µm and fitting the measured data with the theoretical formula. This measurement was repeated while seeding with various laser pulse energies yielding an energy modulation which is proportional to the square root of the laser pulse energy, consistent with the theory. The maximum measured value was $\Delta E/E = 0.4\%$ obtained when seeding with a laser pulse energy of 2.6 mJ (measured before the evacuated part of the seed beamline) at 400 nm.

6.3 Coherence measurements

A good transverse and longitudinal coherence is an essential property needed for a wide range of experiments in holography, microscopy with phase contrast and diffraction imaging.
The coherence of CHG pulses at the short-pulse facility at DELTA has been investigated with a double-slit setup and a Michelson interferometer. The interference patterns were observed using the ICCD camera.
Three methods were used to extract the transverse and longitudinal coherence of CHG pulses from interference patterns: the central visibility of the pattern was determined, a Fourier transformation was applied to the fringe pattern, and a function for the near-field diffraction was fitted to the measured intensity distribution. The results were in good agreement with each other.

Diffraction patterns were recorded with different slit widths and separations. A transverse coherence of up to 0.9 was obtained using the double-slit setup at a distance of about 10 m from the radiator.
By conducting the double-slit experiment for different slit separations, the transverse coherence length has been measured. The characteristic width of the coherence function was about $l_c = 1.9$ mm for 400-nm CHG radiation and $l_c = 1$ mm for 200-nm CHG radiation at a distance of about 10 m from the radiator.
The transverse coherence of the SE is slightly smaller than that of the CHG radiation, but the transverse coherence length is almost the same.

The temporal coherence length of 200-nm-CHG pulses was measured using two methods, a Michelson interferometer and a double slit followed by movable fused silica wedges which cause variable delay between the waves from the two slits. The results from these two methods

are in good agreement yielding a temporal coherence length of 34 fs for the 200-nm CHG pulses.

Measuring the visibility of the interference pattern while varying the r_{56} value of the chicane showed that the temporal coherence of CHG radiation is associated with the microbunching in the chicane. By using the optimum r_{56} value, the visibility of the fringes from Michelson interferometer is at its maximum.
Furthermore, the transverse coherence of 200-nm CHG radiation was measured while varying the chicane strength. The central visibility of the fringes did not change by varying the chicane strength. However, when using the FFT method, the coherence shows a trend similar to CHG intensity, which implies the effect of the temporal coherence on the the off-axis double-slit fringes.

In addition, a rough estimate of the coherence time of the 400-nm CHG radiation was made by recording the interference pattern from a double slit with a high resolution and evaluating the lateral decay of the fringe visibility. The results show a coherence length larger than about 23 fs.
Furthermore, the fast decay of the visibility of SE double-slit fringes measured without using bandpass filters yields a small temporal coherence length of about 1 fs for 200-nm SE.

The coherence was also studied by recording the speckles pattern caused by a bio-polymer sample [115] on a shot to shot basis, confirming a high degree of transverse and temporal coherence of CHG pulses compared to the SE pulse.

6.4 Outlook

While the intermediate goals are CHG user experiments with 23 eV, it is reasonable to perform the first experiments at BL 5 with a photon energy of 9.3 eV to take advantage of the higher flux at the third harmonic of 400-nm seed pulses. For a good temporal resolution, the probe-pulse duration should be reduced from a few ps down to a few 100 fs by lowering the line density of the grating or decreasing the size of the probe beam on the monochromator. The seed beamline should be equipped with an optical feedback system similar to that in the pump-pulse beamline to achieve a better transverse laser-spot position and overlap stability.

The pulse duration of 200-nm CHG radiation could be measured by autocorrelation using two-photon absorption (TPA) [116, 117]. As shown in [116], a pulse energy above 60 nJ is needed for TPA. The 200-nm CHG pulse energy is currently significantly lower than this value, but the seed-laser pulses could be used in a cross-correlator to pump a nonlinear crystal such as CaF_2 or BBO, using the CHG pulses as probe. The duration of the 400-nm laser

pulses can be measured utilizing TPA in a visible-blind SiC photodiode. In addition to a better understanding of the laser-electron interaction and the resulting energy modulation, a good estimate of the pulse duration would be of benefit for user experiments, too.

Simulations focusing on the transverse and temporal coherence of CHG should be done in order to interpret and verify the experimental results and also to understand the coherence properties of CHG adequately.

In the near future, the evacuated section of BL 4 will be extended into the diagnostics hutch, enabling measurements of coherence and spectra at higher photon energies, especially at 9.3 eV (133 nm). Also planned is the construction of a fast VUV spectrometer in the diagnostics hutch, using a recently acquired fast-gated intensified CCD camera. Its ability to capture the radiation of single electron bunches can be used to verify the wavelength stability of the CHG.

Seeding with 265 nm is the next step to generate CHG pulses of lower wavelengths for pump-probe experiments at BL 5. For even higher photon energies, the EEHG [54] scheme is planned to be implemented at DELTA.

References

[1] M. Salaban, *History of animation*, `http://en.wikipedia.org/wiki/History_of_animation#mediaviewer/File:Vase_animation.svg`, (2009).
Licensed under Public domain via Wikimedia Common. The source of the image is the National Museum of Iran.

[2] D. Strickland and G. Mourou, *Compression of amplified chirped optical pulses*, Opt. Commun. 56, 219 (1985).

[3] F. R. Elder et al., *Radiation from Electrons in a Synchrotron*, Phys. Rev. 71, 829 (1947).

[4] T. Shintake, *Review of the worldwide SASE FEL development*, Proc. of Particle Accelerator Conference 2007, Albuquerque, New Mexico, USA, 89.

[5] W. Ackermann et al., *Operation of a free-electron laser from the extreme ultraviolet to the water window*, Nature Photonics 1, 336 (2007).

[6] L.-H. Yu et al., *High-Gain Harmonic-Generation Free-Electron Laser*, Science 289, 932 (2000).

[7] E. Allaria et al., *Highly coherent and stable pulses from the FERMI seeded free-electron laser in the extreme ultraviolet*, Nature Photonics 6, 699 (2012).

[8] A list of synchrotron light sources can be found in `http://www.lightsources.org/regions`.

[9] M. Abo-Bakr et al., *Brilliant, Coherent Far-Infrared (THz) Synchrotron Radiation*, Phys. Rev. Lett. 90, 094801 (2003).

[10] R. Coïsson and F. D. Martini, *Free-Electron Relativistic Scatterer for UV-Generation*, Physics of Quantum Electronics: Free-Electron Generators of Coherent Radiation 9, 939, Addison-Wesley (1982).

[11] B. Girard et al., *Optical Frequency Multiplication by an Optical Klystron*, Phys. Rev. Lett. 53, 2405 (1984).

[12] R. Prazeres et al., *Coherent harmonic generation in the vacuum ultraviolet spectral range on the storage ring ACO*, Nucl. Instr. Meth. A, 272, 68 (1988).

[13] R. Prazeres et al., *Coherent harmonic generation in VUV with the optical klystron on the storage ring Super-ACO*, Nucl. Instr. Meth. A 304, 72 (1991).

[14] M. Labat et al., *Coherent harmonic generation experiments on UVSOR-II storage ring*, Nucl. Instr. Meth. A 593, 1 (2008).

[15] M. Labat et al., *Coherent harmonic generation on UVSOR-II storage ring*, Eur. Phys. J. D 44, 187 (2007).

[16] G. De Ninno et al., *Generation of Ultrashort Coherent Vacuum Ultraviolet Pulses Using Electron Storage Rings: A New Bright Light Source for Experiments*, Phys. Rev. Lett. 101, 053902 (2008).

[17] E. Allaria et al., *Experimental Characterization of Nonlinear Harmonic Generation in Planar and Helical Undulators*, Phys. Rev. Lett. 100, 174801 (2008).

[18] C. Spezzani et al., *Sub-picosecond coherent VUV source on the Elettra storage ring*, Nucl. Instr. Meth. A 596, 451 (2008).

[19] M. Höner et al.,*A dedicated THZ beamline at DELTA*, Proc. International Particle Accelerator Conference 2011, San Sebastian, Spain, 2939.

[20] S. Khan et al., *Coherent Harmonic Generation at DELTA: A new facility for ultrashort pulses in the VUV and THz regime*, Sync. Rad. News 24, 18 (2011).

[21] S. Khan et al., *Generation of Ultrashort and Coherent Synchrotron Radiation Pulses at DELTA*, Sync. Rad. News 26, 25 (2013).

[22] H. Huck et al., *Coherent Harmonic Generation at the DELTA storage ring* , Proc. Free Electron Laser 2011, Shanghai, China, 5.

[23] M. Zeinalzadeh et al., *Temporal and spatial allignment of the electron bunches and ultrashort laser pulses for the CHG experiment at DELTA*, Proc. International Particle Accelerator Conference 2011, San Sebastian, Spain, 2945.

[24] A. Schick et al., *Recent Results from the short-pulse facility at the DELTA storage ring*, Proc. International Particle Accelerator Conference 2012, New Orleans, USA, 1617.

[25] H. Huck et al., *Status of the DELTA short-pulse facility*, Proc. Free Electron Laser 2012, Nara, Japan, 401.

[26] M. Huck et al., *Experimental characterization of the Coherent Harmonic Generation source at the DELTA storage ring*, Proc. International Particle Accelerator Conference 2013, Shanghai, China, 2132.

[27] P. Ungelenk et al., *Temporal and spectral observation of laser-induced THz radiation at DELTA*, Proc. International Particle Accelerator Conference 2013, Shanghai, China, 94.

[28] R. Molo et al., *Investigation of the magnetic chicane of the short-pulse facility at the DELTA storage ring*, Proc. International Particle Accelerator Conference 2013, Shanghai, China 1889.

[29] H. Wiedemann, *Particle Accelerator Physics*, 3rd edition, Springer (2007).

[30] K. Wille, *The Physics of Particle Accelerators an introduction*, Oxford University Press (2005).

[31] P. Schmüser, M. Dohlus and J. Rossbach, *Ultraviolet and Soft X-Ray Free-Electron Lasers*, Springer Tracts in Modern Physics 229 (2008).

[32] A. E. Siegman, *Lasers*, University Science Books (1986).

[33] J. C. Diels and W. Rudolph, *Ultrashort Laser Pulse Phenomena (Optics and Photonics Series)*, Academic Press (1999).

[34] B. E. A. Saleh, M. Carl Teich, *Fundamentals of Photonics*, John Wiley & Sons (1991).

[35] J. W. Goodman, *Statistical Optics*, John Wiley & Sons (2000).

[36] J. D. Jackson, *Classical Electrodynamics*, 3rd edition, John Wiley & Sons, Inc. (1998).

[37] T. Tanaka, *A synchrotron radiation calculation code* J. Synchrotron Rad. 8, 1221 (2001). `http://radiant.harima.riken.go.jp/spectra`.

[38] D. A. G. Deacon, *Storage ring free electron lasers: Experimental progress and future prospects*, Nucl. Instr. Meth. 208, 171 (1983).

[39] H. Huck, *Optimierung und Charakterisierung des Free Electron Lasers am Speicherring DELTA*, Dissertation, TU Dortmund University (2009).

[40] P. Elleaume, *Optical Klystron*, J. Phys. (Paris), Colloques 44 (C1), 353 (1983).

[41] M. Born and E. Wolf, *Principles of Optics*, Cambridge University Press (1999).

[42] E. Hecht, *Optics*, 4th edition, Addison Wesley (2002).

[43] D. J. Kane, R. Trebino, *Characterization of arbitrary femtosecond pulses using frequency-resolved optical gating*, IEEE Journal of Quantum Electronics 29, 571 (1993).

[44] Aleph, *Gaussian beam with German description*, `http://commons.wikimedia.org/wiki/File:Gaussian_beam_with_german_description.svg#mediaviewer/File:Gaussian_beam_with_german_description.svg`
Licensed under Creative Commons Attribution-Share Alike 2.5 via Wikimedia Commons (2008).

[45] C. Iaconis, I. A. Walmsley, *Spectral phase interferometry for direct electric-field reconstruction of ultrashort optical pulses*, Optics Letters 23, 792 (1998).

[46] A. E. Siegman, *New developments in laser resonators*, Proc. SPIE 1224, 2 (1990).

[47] Applied Optics Research, *GLAD Theory Manual*, 4.7 edition (2001).

[48] R. Ischebeck, *Transverse Coherence of a VUV Free Electron Laser*, Dissertation, University of Hamburg (2003).

[49] `http://desy.cfel.de/cid/`

[50] A. Zholent and M. Zolotorev, *Femtosecond X-Ray pulses of synchrotron radiation*, Phys. Rev. Lett. 76, 912 (1996).

[51] R.W. Schoenlein et al., *Generation of Femtosecond Pulses of Synchrotron Radiation*, Science 287, 2237 (2000).

[52] S. Khan et al., *Femtosecond Undulator Radiation from Sliced Electron Bunches*, Phys. Rev. Lett. 97, 074801 (2006).

[53] P. Beaud et al., *Spatiotemporal Stability of a Femtosecond Hard–X-Ray Undulator Source Studied by Control of Coherent Optical Phonons*, Phys. Rev. Lett. 99, 174801 (2007).

[54] G. Stupakov, *Using the Beam-Echo Effect for Generation of Short-Wavelength Radiation*, Phys. Rev. Lett. 102, 074801 (2009).

[55] D. Xiang et al., *Demonstration of the Echo-Enabled Harmonic Generation Technique for Short-Wavelength Seeded Free Electron Lasers*, Phys. Rev. Lett. 105, 114801 (2010).

[56] D. Xiang et al., *Demonstration of EEHG at the* 14^{th} *harmonic*, THOANO02, Proc. Free Electron Laser 2013, Manhattan, USA.

[57] E. Hemsing et al., *Highly coherent vacuum ultraviolet radiation at the* 15^{th} *harmonic with echo-enabled harmonic generation technique*, Phys. Rev. ST Accel. Beams 17, 070702 (2014).

[58] D. Xiang et al., *Evidence of High Harmonics from Echo-Enabled Harmonic Generation for Seeding X-Ray Free Electron Lasers*, Phys. Rev. Lett. 108, 024802 (2012).

[59] Z.T. Zhao et al., *First lasing of an echo-enabled harmonic generation free-electron laser*, Nature Photonics 6, 360 (2012).

[60] E. L. Saldin et al., *The Physics of Free Electron Lasers*, Springer (2000).

[61] R. Bonifacio et al., *Large harmonic bunching in a high-gain free-electron laser*, Nucl. Instr. Meth. A 293, 627 (1990).

[62] W.B. Colson and A.M. Sessler, *Free Electron Lasers*, Ann. Rev. Nucl. Part. Sci. 35, 25 (1985).

[63] L. H. Yu and I. Ben-Zvi, *High-gain harmonic generation of soft X-rays with the "fresh bunch" technique*, Nucl. Instr. Meth. A 393, 96 (1997).

[64] M. Höner, *Optical Design and Construction of a Dedicated THz Beamline at DELTA and Study of Laser-Electron Interact*, Diploma thesis, TU Dortmund University (2011).

[65] F. van der Veen, *Shining light on matter*, CERN Accelerator School, Synchrotrons and FELS, Brunnen, Switzerland (2003).

[66] A. Einstein, *Über einen die Erzeugung und Verwandlung des Lichtes betreffenden heuristischen Gesichtspunkt*, Annalen der Physik. Leipzig 17, 132 (1905).

[67] S. Hüfner, *Photoelectron Spectroscopy Principles and Applications*, 3rd edition, Springer (2003).

[68] A. Eschenlohr et al., *Ultrafast spin transport as key to femtosecond demagnetization*, Nature Materials 12, 332-336 (2013).

[69] J. Friedl, DELTA group, *Recent Results of the Commissioning of the DELTA Facility*, Proc. Particle Accelerator Conference 1997, Vancouver, Canada, 724.

[70] D. Schirmer, *Synchrotron radiation sources at DELTA*, DELTA internal report 001-05, TU Dortmund University (2009).

[71] M. Höner et al., *Investigation of beam instabilities at DELTA using bunch-by-bunch feedback systems*, Proc. International Particle Accelerator Conference 2014, Dresden, Germany, 3486.

[72] 9$^{\text{th}}$ DELTA User Meeting & Annual Report (2013). `http://www.delta.tu-dortmund.de/cms/Medienpool/User_Reports/DELTA_User_Report_2013.pdf`

[73] M. Tolan et al., *DELTA: Synchrotron Light in Nordrhein-Westfalen*, Synchrotron Radiation News 16(2), 9 (2003).

[74] L. Plucinski et al., *A hemispherical photoelectron spectrometer with 2-dimensional delay-line detector and integrated spin-polarization analysis*, J. Electron Spectros. Rel. Phenom. 181, 215 (2010).

[75] C. Zilkens, *Gestufte Oberflächen und Quasieindimensionale Strukturen Photoemission an 3d Metallen auf W(110)*, Dissertation, Köln University (2002).

[76] `www.surface-concept.com`

[77] `http://www.vgscienta.com/`

[78] J. Kirschner, R. Feder, *Spin Polarization in Double Diffraction of Low-Energy Electrons from W(001): Experiment and Theory*, Phys. Rev. Lett. 42, 1008 (1979).
`http://www.focus-gmbh.com`

[79] A. Schick, *Construction of a Seed Beamline for the CHG Facility at DELTA and Optimization of the Laser-Electron Interaction*, Dissertation, TU Dortmund University (in preparation).

[80] P. Ungelenk, *A New THz Beamline at DELTA - Tracking Simulations, Mechanical Design, Assembly, and First Measurements*, Diploma thesis, TU Dortmund University (2011).

[81] M. Höner, *Optical Design and Construction of a Dedicated THz Beamline at DELTA and Study of Laser-Electron Interaction*, Diploma thesis, TU Dortmund University (2011).

[82] The APD (Hamamatsu S9073) was set up by K. Holldack, HZB, Berlin.

[83] `https://www.coherent.com/Products/?1443/Synchrolock-AP`

[84] P. Probst et al., *$YBa_2Cu_3O_{7-\delta}$ quasioptical detectors for fast time-domain analysis of terahertz synchrotron radiation*, Appl. Phys. Lett. 98, 043504 (2011).

[85] P. Thoma et al., *High-Speed Y–Ba–Cu–O Direct Detection System for Monitoring Picosecond THz Pulses*, IEEE Trans. on THz Sci. Tech. 3, 81 (2013).

[86] M. A. C. de Araújo et.al., *Measurement of Gaussian laser beam radius using the knife-edge technique: improvement on data analysis*, Applied Optics 48, 2, 393 (2009).

[87] Private communication with Bernard Riemann and Holger Huck, DELTA, TU Dortmund University.

[88] The merging part of pump-pulse beamline was designed and provided by Stefan Cramm, FZJ, PGI6, Jülich.

[89] The photodiode unit was constructed and mounted by Stefan Cramm, FZJ, PGI6, Jülich, as well as the Labview program.

[90] The concrete pillars were designed by Markus Höner and Peter Ungelenk, DELTA, TU Dortmund University.

[91] T. Noll, *Elastische parallelkinematische Führungsgetriebe für ultrapraezise Bewegungen im Vakuum*, Dissertation, TU Berlin (2003).

[92] `http://www.tem-messtechnik.de/aligna.htm`

[93] C. La-O-Vorakiat, et al., *Ultrafast Demagnetization Dynamics at the M Edges of Magnetic Elements Observed Using a Tabletop High-Harmonic Soft X-Ray Source*, Phys. Rev. Lett. 103, 257402 (2009).

[94] B. Koopmans et al., *Experimental access to femtosecond spin dynamics*, J. Phys.: Condens. Matter 15, S723 (2003).

[95] T. Roth et al., *Dynamics of the coercivity in ultrafast pump–probe experiments*, J. Phys. D: Appl. Phys. 41, 164001 (2008).

[96] H.A. Dürr, *Femtosecond electron and spin dynamics in ferromagnetic Ni probed by UV and soft X-ray pulses*, Nucl. Instr. Meth. A 601, 132 (2009).

[97] D. Venus et al., *Magnetic dichroism in UV photoemission at off-normal emission: Study of the valence bands*, Phys. Rev. B. 55, 2594 (1997).

[98] `www.lasercomponents.com`

[99] Layertec catalog 2013, Femtosecond Laser, `http://www.layertec.de`.

[100] `http://www.swampoptics.com`

[101] `www.dataray.com`

[102] H. Garcia et al., *New approach to the measurement of the nonlinear refractive index of short (<25 m) lengths of silica and erbium-doped fibers*, Opt. Lett. 28, 1796 (2003).

[103] E.T.J. Nibbering et al., *Determination of the inertial contribution to the nonlinear refractive index of air, N2, and O2 by use of unfocused high-intensity femtosecond laser pulses*, J. Opt. Soc. Am. B 14, 650 (1997).

[104] The software *Vchirp* is provided by the company *Venteon*, `www.venteon.com`

[105] `http://www.sglux.de/`

[106] A transmission spectrum of Lithium Fluoride can be found at: `http://www.korth.de/index.php/162/items/18.html`

[107] The software and the hardware of the delay line detector was modified by Dr. Andreas Oeslner, Surface Concept GmbH, Mainz.

[108] S. Döring et al., *A short-pulse facility for time and angle resolved photoemission experiments at BL5*, 9th DELTA User Meeting & Annual Report (2013). http://www.delta.tu-dortmund.de/cms/Medienpool/User_Reports/DELTA_User_Report_2013.pdf

[109] The camera was provided by B. Schmidt and S. Wunderlich, DESY, Hamburg.

[110] http://www.meko.de/

[111] A. Singer et al., *Spatial and temporal coherence properties of single free-electron laser pulses*, Optics Express 20, 17480 (2012).

[112] Y. Cai et al., *Interdependence between the temporal and spatial longitudinal and transverse degrees of partial coherence and a generalization of the van Cittert–Zernike theorem*, J. Opt. Soc. Am. A, 29, 2542 (2012).

[113] V. P. Ryabukho et al., *Influence of the frequency spectrum width on the transverse coherence of optical field*, Optics and Spectroscopy, 108, 979 (2010).

[114] http://www.piezosystem.de

[115] C. Gutt et al., *Femtosecond speckle and coherence experiments at the CHG short-pulse facility DELTA*, SNI 2014, Bonn, Germany.

[116] P. C. Heisel et al., *197 nm femtosecond laser-pulse duration: comparison of autocorrelation measurements*, Appl. Phys. B: Lasers and Optics 112, 49 (2013).

[117] C. Homann et al., *Convenient pulse length measurement of sub-20-fs pulses down to the deep UV via two-photon absorption in bulk material*, Appl. Phys. B 104 (2011).

Acknowledgments

This thesis would not have been possible without the help, support and patience of my supervisor, Prof. Dr. Shaukat Khan, for which I am extremely grateful.
I appreciate Prof. Dr. Christian Gutt, the second supervisor of my thesis, for his very useful advices and helpful comments.

I would like to thank my husband Holger for both his personal and academic support and great patience at all times.

My parents, brothers and sisters have given me their selfless support and encouragement, for which my mere expression of thanks does not suffice.

The good advice, support and friendship of my colleagues, especially Peter Ungelenk, Andreas Schick, Robert Molo, Markus Höner, Andre Nowaczyk, Helge Rast, Gerrit Schünemann, Patryk Towalski, Fin Hendrik Bahnsen, Svenja Hilbrich, Arne Meyer auf der Heide, Carsten Mai and Bernard Riemann has been invaluable on both an academic and a personal level.

I would like to express my appreciation for the efforts of the technical and scientific staff of DELTA and the physics faculty, especially Wolfgang Brembt, Günther Dahlmann, Thomas Dybiona, Jochem Friedl, Bernhard Hippert, Vadim Kniss, Peter Kortmann, Hans-Peter Ruhl, Detlev Schirmer, Gerald Schmidt, Tanja Schulte-Eickhoff, Ulf Berges and Thomas Weis.

I appreciate the help, advice and support of the DELTA user community, especially Stefan Cramm, Lukasz Plucinski, Sven Döring and Alexej Herdt.

I am pleased to thank our colleagues at other institutes particularly, FZJ in Jülich, HZB in Berlin, DESY in Hamburg and KIT in Karlsruhe, for their continuous support and advices.

I would like to acknowledge the financial, academic and technical support of the TU Dortmund University, Center for Synchrotron Radiation DELTA, DFG, BMBF and NRW Forschungsschule.